Macropinocytosis-Inducing Peptides: Identification, Utility, and Mechanism-of-Action

新規マクロピノサイトーシス誘導ペプチドの同定、
細胞内送達への有用性と作用様式

２０２０

アラフィレス　ジャン ヴィンセント ヴァレンズエラ

Arafiles, Jan Vincent Valenzuela

Acknowledgments

The work herein was done under the supervision of Prof. Shiroh Futaki (Institute for Chemical Research, Kyoto University). My utmost gratitude is given to Prof. Futaki for not only fostering my professional growth in the scientific research field but also for providing a suitable environment for my personal growth in a foreign land. Working on a post-graduate degree, away from home, family, and friends, is physically and mentally demanding, but Prof. Futaki never fails to offer some grain of experiential wisdom and encouragement, to make this chapter of my life's journey a bit more bearable. May it be attending conferences, introducing us to notable experts in the field of peptide chemistry, or just simply having casual conversations in the tearoom, he always supports his students to succeed. He is a great mentor. For this, I am indebted.

I would also like to thank Assoc. Prof. Miki Imanishi, Assoc. Prof. Hisaaki Hirose and Asst. Prof. Kenichi Kawano (Institute for Chemical Research, Kyoto University) for their technical and scientific guidance for the success of this work. Every one of them provided their flavor of expertise and valuable knowledge. Without their help, this thesis would not be possible. Likewise, my gratitude is given to Prof. Kazuhisa Nakayama and Prof. Yoshinobu Takakura (Graduate School for Pharmaceutical Sciences, Kyoto University) for giving their valuable time to review this thesis.

For their technical assistance, I extend my gratitude to Prof. Hirokazu Tamamura (Tokyo Medical and Dental University), Prof. Wataru Nomura (Hiroshima University), and Dr. Maxwell M. Sakiayamah (Tokyo Medical and Dental University) for performing the NanoBRET-based competition assay. I also thank Prof. Yoshio Hayashi (Tokyo University for Pharmacy and Life Sciences) for providing the NPyS-OMe reagent for the synthesis of the oxidized peptides and Prof. Akira Otaka (Tokushima University) for providing his valuable advice for the synthesis of the P4A dimers. My appreciation is also given to Dr. Kazuhiro Sonomura (Shimadzu Corp.) for performing the Ultra HPLC analysis.

Being the only foreigner in the Futaki Lab for some time, I thought that it would be hard for me to "fit in" – I was mistaken. My "senpais" made my time in the lab very insightful. They gave me technical, scientific, and career advice, and made sure to make me feel at home. I thank Dr. Yoshimasa Kawaguchi (Shionogi & Co., Ltd.), Dr. Akihiko Oku (AstraZeneca PLC), Dr. Tomo Murayama (National Police Agency, Japan), Dr. Tsuji Shogo (National Center for Geriatrics and Gerontology, Japan), Dr. Koki Shinoda (Nippon Shinyaku Co., Ltd.), and Dr. Toshihiro Masuda (Maruho Co., Ltd.) for making me part of the lab in its entirety. Also, I thank

all the past and current members of Futaki Lab for being a constant source of energy. Especially, I give my heartfelt appreciation to Dr. Misao Akishiba (Helmholtz Zentrum München) for teaching me from day one, and for a life-long friendship that transcends cultural and lingual divides.

For being the bridge for me to pursue my graduate degrees in Japan, I thank the Asian Chemical Biology Initiative, spearheaded by Prof. Motonari Uesugi (iCeMs, Kyoto University) and Ms. Mitsue Nakashima, for allowing my sensei and me to meet. Most importantly, I thank the Japanese Government (Monbukagakusho: MEXT) Scholarship for funding my studies.

Likewise, I thank my friends, Watson, Bev, Yejin, Hue, Yui, Ate Mel, Dalton, Macky, Francine, Mica, Kim Castro, Kim Garcia, and Julius. They are constant sources of happiness outside of the lab.

Doctoral studies seem unsurmountable alone, but walking with someone together, lightens the load just enough to finish the race. For this, I thank Dr. Huyen Dinh (Institute for Advanced Energy, Kyoto University) for her unending love and support throughout this arduous journey. Her presence in my life is instrumental in keeping me rooted and steadfast in achieving this degree. Along the way, she made me rethink a lot about how I live my life – unceasingly reminding me to keep a leveled head, stay humble, show appreciation, and always understand. I grew much more as a professional, and as a person because of her. Dù anh không biết số phận rồi sẽ đưa chúng mình về đâu, anh vẫn rất hạnh phúc vì đã được gặp, quen, và thương nhau. Anh em yêu.

Hindi magbubunga ang kahit anong itinanim kung hindi ito pagsisikapan. Ngunit hindi magiging possible ang lahat ng karangalang ito kung hindi dahil sa walang humpay na suporta mula sa aking pamilya at mga kaibigan. Dahil rito, taos puso and aking pasasalamat para sa aking ina na si Josie, sa aking kapatid na si Hazel, Lola Rosario, Ayi Tessie, Ayi Teng, Yaya Amy, Ate Sally, Winifred, Gleng, Maden, Devs, Vannie at Ann. Sila ang bukal ng walang humpay na tiwala at suporta na aking pinagkukunan ng lakas ng loob at inspirasyon. Hindi lamang para sa sarili itong tagumpay na natatamasan ko, dadapwat ito ay para rin lang sa ating lahat. Salamat.

To the reader of this thesis, know that at the time of writing this work, the world is being ravaged by the COVID-19 pandemic – a time when we are witnessing the fragility of institutions that are not rooted on science and facts. On the other hand, this is also the time of unprecedented international cooperation among scientists across the globe in search for a remedy for this catastrophe. Let this remind us on the immense potentials and possibilities stemming from interdisciplinary collaboration among scientists working towards a singular goal.

Table of Contents

List of Abbreviations

CPP	Cell-penetrating peptide
SDF−1α	Stromal cell-derived factor 1α
IgG	Immunoglobulin G
TALE	Transcription activator-like effector
CXCR4	CXC-chemokine receptor type 4
R12	Dodeca-arginine
Dex70-FL	Fluorescein-labeled 70kDa dextran
EIPA	5-(*N*-ethyl-isopropyl)amiloride
PI3K	Phosphoinositide 3-kinase
F-actin	Filamentous actin
R8	Octa-arginine
TPA	12-*O*-tetradecanoylphorbol-13-acetate
PDGF-BB	Platelet-derived growth factor B
SN21-FITC	Fluorescein isothiocynate-labeled SN21
Dex70-TMR	Tetramethylrhodamine-labeled 70kDa dextran
BMP	Bis(monoacylglycerol)phosphate
EGFP	Enhanced green fluorescent protein
LLOMe	L-leucyl-L-leucyl methyl ester
pDNA	Plasmid DNA
siRNA	Small-interfering RNA
EMSA	Electrophoretic mobility shift assay
HeLa-GL3	HeLa cells stably expressing GL3 firefly luciferase
LF2000	Lipofectamine 2000
IgG-AF488	Alexa Fluor 488-labeled IgG
Anti-NPC-AF594	Alexa Fluor 594-labeled anti-nuclear pore complex IgG
Control IgG-AF594	Alexa Fluor 594-labeled Mouse isotype control IgG
HeLa-TBS-Luci	HeLa cells stably transfected with luciferase gene downstream of a TALE-binding sequence

NanoBRET	NanoLuc-based bioluminescence resonance energy transfer assay
PtdIns(4,5)P2	Phosphatidylinositol 4,5-bisphosphate
PtdIns(3,4,5)P3	Phosphatidylinositol 3,4,5-triphosphate
HPLC	High performance liquid chromatography
MALDI-TOF MS	Matrix-assisted laser desorption/ionization-time of flight mass spectrometry
α–MEM	Minimum Essential Media α
SE	Standard error

Introduction

Intracellular delivery of exogenous cargoes provide useful information for molecular cell biology, and chemical biology, having potential for drug discovery, and therapeutics.[1] Protein- and peptide-based therapeutic agents often require a way to enter cells to maximize their potencies, and this is a reason for the increasing demands for better strategies for delivery.[2,3]

Delivery of cargoes into the cell can be performed either through direct transduction or via endocytic pathways (Figure 0). Direct transduction enables exogenous cargoes to have direct access to the cytosol, where the cargo can exhibit its biological activity. Different groups have provided strategies to achieve direct transduction of cargoes, namely, mechanical perturbation of cell membranes,[4] chemical modification of cargoes by esterification,[5] and conjugation with cell-penetrating peptides (CPPs; short peptides capable of intracellular delivery).[6–8] These strategies were found promising but are limited by the sizes, the properties, and the required amount of cargoes.[9]

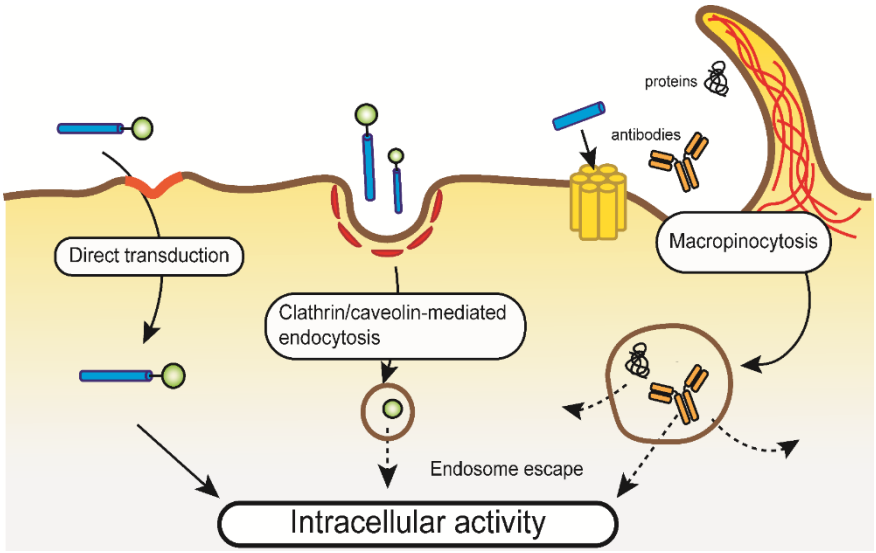

Figure 0. Different pathways for intracellular delivery. Direct penetration allows uptake of cargo molecules directly into the cytosol. Clathrin/caveolin-mediated endocytosis is small-scale uptake compared to macropinocytosis, both of which require the cargos to escape from endosomes into the cytosol where the cargoes can exhibit their biological activities.

Delivery of large bioactive cargoes can be achieved through the cellular endocytic pathways.[10,11] A good example is the delivery of bioactive cargoes conjugated with CPPs,[9,12,13] which could be related to the capacity of endocytic pathways to accommodate larger cargoes into vesicular structures.[14] Commonly discussed endocytic uptake mechanisms for intracellular deliveries are clathrin- or caveolin-mediated endocytosis and macropinocytosis.[15] Delivery systems using endocytosis mostly utilize specific receptors for the uptake of materials of interests. However, there are a limited number of receptors available for the needed delivery. Moreover, the sizes of endosomes formed through these pathways are only up to ~120 nm for clathrin-mediated endocytosis and ~80 nm for caveolin-mediated endocytosis, possibly restricting the number of cargoes that can be accommodated in endosomes.[16–18]

Different from clathrin/caveolin-mediated endocytosis, macropinocytosis is an actin-mediated form of endocytosis, which facilitates bulk uptake of extracellular fluid and materials into large endosomes, called macropinosomes.[19,20] The diameters of macropinosomes are reported to be up to 5 μm, and this is considerably larger than those of endosomes formed by clathrin- and caveolin-mediated endocytosis. Previous studies suggested the involvement of macropinocytosis in the cellular entry of specific viruses.[21] On the other hand, previous studies demonstrated the significance of this pathway in the cellular uptake of CPPs,[22,23] stapled peptides,[24] liposomes,[25] and exosomes.[26] Thus, macropinocytosis can be regarded as a general and ubiquitous cellular uptake pathway. Lipid-based and nanoparticle-based intracellular delivery systems induce macropinocytosis to achieve cellular delivery.[27] Establishing strategies that specifically activate macropinocytosis, therefore, can be advantageous for large scale uptake of bioactive macromolecules.

Considering the potentials of macropinocytosis, this dissertation focused on exploiting macropinocytosis for intracellular delivery of macromolecules and understanding the mechanisms underlying macropinocytosis induction. Specifically, a short peptide derived from SDF-1α (SN21) was identified as a macropinocytosis inducer. Nucleic acids and bioactive proteins underwent successful intracellular delivery in the presence of SN21. Additionally, the work also tried to explain the mechanism underlying the induction of macropinocytosis by the identified peptide. The findings should aid in developing new intracellular delivery strategies based on macropinocytosis induction.

Chapter One:

Nucleic Acid and Protein Delivery Using a Macropinocytosis-Inducing Peptide Combined with a Membrane-Lytic Peptide

第1章

マクロピノサイトーシス誘導ペプチドと膜溶解ペプチドとを併用した核酸およびタンパク質送達

Intracellular delivery via endocytic pathways requires (1) the accumulation of cargo molecules into endosomes, and (2) an effective disruption of endosomal membranes to release the cargoes into the cytosol (i.e., endosome escape). Despite numerous works on endosome escape strategies,[28–30] there are still large rooms for improving the efficacy in these aspects. Macropinocytosis induction can offer a solution partly because of its ability to uptake exogenous materials on a large scale. Combining a robust physiological induction of macropinocytosis with endosome escape should improve the efficiency of intracellular delivery (Fig. 1–1). This chapter discusses the use of an identified macropinocytosis-inducing peptide derived from stromal cell-derived factor 1α (SDF-1α), fused with a physicochemical disruptor of endosomal membranes, to deliver functional nucleic acids and proteins into cells.

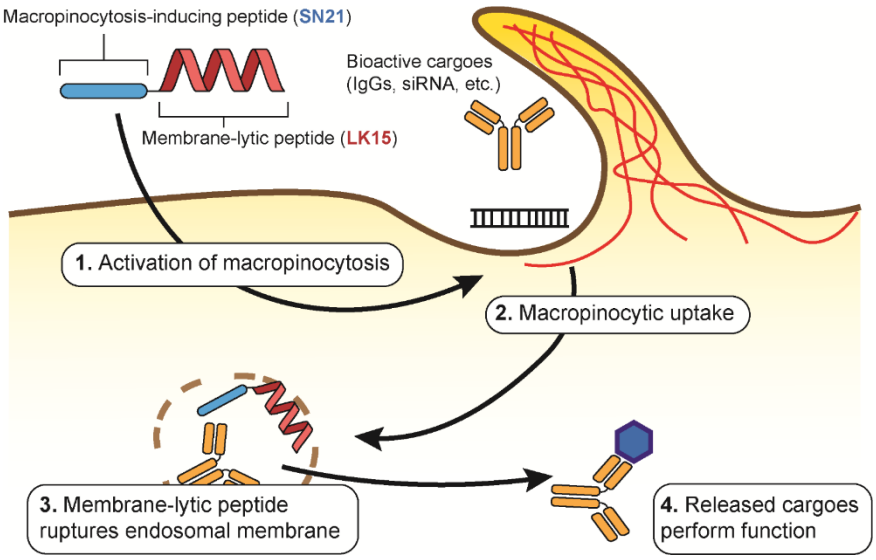

Figure 1–1. Proposed macropinocytosis-based intracellular delivery strategy. An identified macropinocytosis-inducing peptide (SN21) is combined with a membrane-lytic peptide (LK15). The conjugate should facilitate (1) the induction of macropinocytosis to accumulate bioactive cargoes by (2) macropinocytic uptake, followed by (3) disruption of endosomal membranes, and (4) release of the cargoes into the cytosol to exhibit their activities.

I. Identification of macropinocytosis-inducing peptides

Previous work in the Futaki laboratory showed that the CPP dodeca-arginine (R12) stimulates CXCR4 to induce its macropinocytic uptake.[31] The same study showed the CXCR4 ligand, SDF-1α, activates macropinocytosis. Given the potential usefulness of this uptake system, SDF-1α was used as a template to derive novel macropinocytosis-inducing peptides in this study.

Structural studies by Crump et al. and Kofuku et al. suggested that the N-terminal 17-amino acid residues of SDF-1α are crucial for its activity.[32,33] Residues 12–17 (RFFESH) makes the initial contact with the N-terminal extracellular region of CXCR4, and residues 1–8 (KPVSLSYR) is then allowed to access the binding site of CXCR4, resulting in conformational changes in CXCR4 that lead to signaling.[34] Peptides having these features were studied to be agonists of CXCR4 to induce chemotaxis.[35,36] Considering that SDF-1α induces macropinocytosis, these short peptides may have the same ability. To test this hypothesis, peptides comprised of n residues of SDF-1α N-terminus (SNn peptides; n = 8, 17, 21, 23, and 25) were synthesized by Fmoc-based solid-phase peptide synthesis (Fig. 1–2A). SN8 contained the receptor-activating motif, while SN17 to SN25 contained both receptor-activating and receptor-binding regions with C-terminal extensions that are sequentially longer. These peptides were tested for their induction of Dex70-FL (=fluorescein-labeled 70kDa dextran) uptake, which is a fluid-phase endocytosis marker that serves as the primary criterion to evaluate macropinocytosis induction.[37] All synthesized peptides, except for SN8, induced a significant increase in the uptake of Dex70-FL (Fig. 1–2B, C). The observed activity of SN17 to SN25 is likely to depend on the presence of both receptor-binding and

receptor-activating regions, both of which are required for the activity of SDF-1α. Among the derived peptides that increased dextran uptake, SN21 is the shortest candidate that significantly induced Dex70-FL uptake (~75% higher than no peptide treatment control; Fig. 1–2C), while showing comparable induction of Dex70-FL uptake to that obtained from 100 nM SDF-1α treatment (Fig. 1–2D). In the interest of practicality, this study focused on SN21.

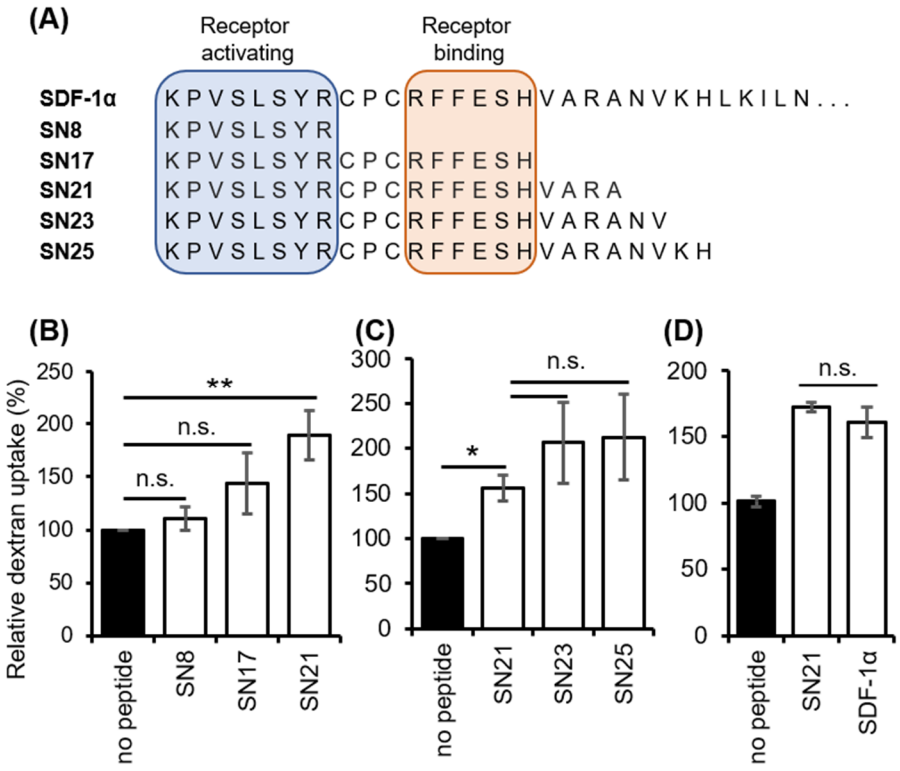

Figure 1–2. Design and screening of SDF-1α-derived peptides. (A) Sequences of SDF-1α, SN8, SN17, SN21, SN23, and SN25 indicating the receptor-activating and receptor-binding motifs. The C-termini of the synthesized peptides are amidated. (B, C) Dex70-FL uptake induced by SDF-1α-derived peptides in HeLa cells treated with 5 μM peptide with 1 mg/mL Dex70-FL in α-MEM (−). (D) Comparable Dex70-FL uptake induced by 100 nM SDF-1α and 5 μM SN21. Data are presented as mean ± standard error (SE) of three independent experiments. [(A) one-way Analysis of Variance (ANOVA) followed by Dunnett's *post-hoc* test, (B) Student's *t*-test, and (C) one-way ANOVA followed by Tukey's *post-hoc* test; **, $P < 0.01$; *, $P < 0.05$; n.s., not significant)].

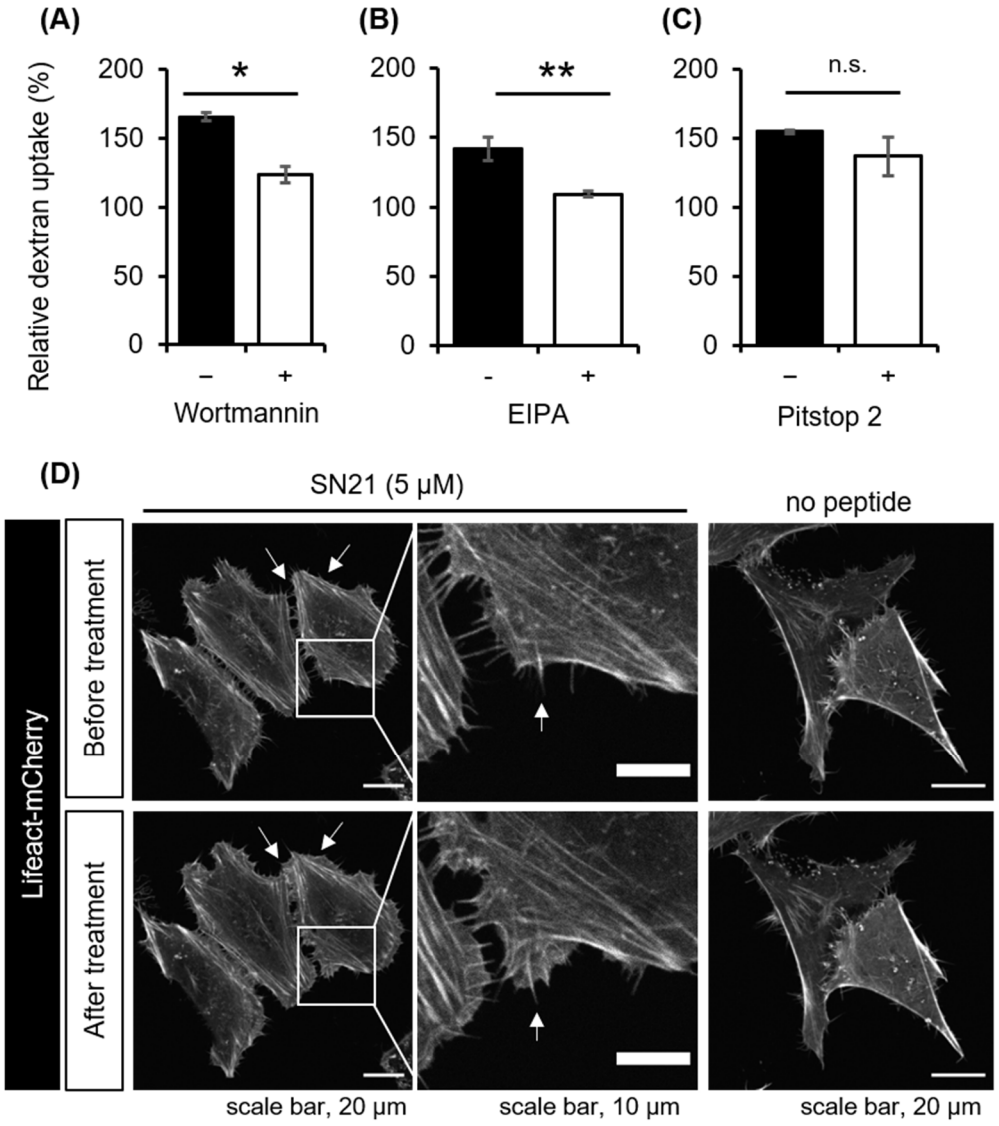

Figure 1–3. Confirming macropinocytosis induction by SN21. Effects of pretreating cells with (A) 500 nM wortmannin, (B) 100 μM EIPA, or (C) 25 μM Pitstop 2 on Dex70-FL uptake induced by 5 μM SN21. Data are presented as mean ± SE of three independent experiments (Student's *t*-test; **, $P < 0.01$; *, $P < 0.05$; n.s., not significant). (D) Dynamic actin cytoskeletal reorganization observed in Lifeact-mCherry-expressing HeLa cells before and after treatment with 5 μM SN21 for 10 min using FV3000 confocal laser scanning microscopy. White arrows indicate the locations of dynamic cyotskeletal reorganization.

The Dex70-FL uptake assay in the presence of specific inhibitors and observation of dynamic reorganization of the actin cytoskeleton confirm the activation of macropinocytosis by SN21. 5-(*N*-ethyl-isopropyl)amiloride (EIPA) and wortmannin are commonly used inhibitors of macropinocytosis.[38] EIPA inhibits Na^+/H^+ exchange, which lowers the submembranous pH preventing Rac1 signaling – stopping the cytoskeletal reorganization vital for initiating macropinocytosis.[39] Wortmannin inhibits phosphoinositide 3-kinase (PI3K) – preventing closure of macropinosomes.[40] Data from experiments using these inhibitors should provide a view on the macropinocytosis-inducing activity of SN21. Co-treatment with EIPA (100 μM) or wortmannin (500 nM) decreased SN21-stimulated Dex70-FL uptake (Fig. 1–3A, B). However, Figure 1–3C shows that inhibition of clathrin coat assembly using 25 μM pitstop 2[41] did not affect SN21-induced Dex70-FL uptake, suggesting that SN21-induced dextran uptake is less likely to be due to clathrin-mediated endocytosis. Time-lapse imaging of HeLa cells expressing Lifeact-mCherry (a marker for filamentous actin) treated with SN21 revealed lamellipodia formation (i.e., actin-rich veil-like cellular protrusions), suggesting the formation of membrane ruffling accompanied by macropinocytosis (white arrows, Fig. 1–3D).

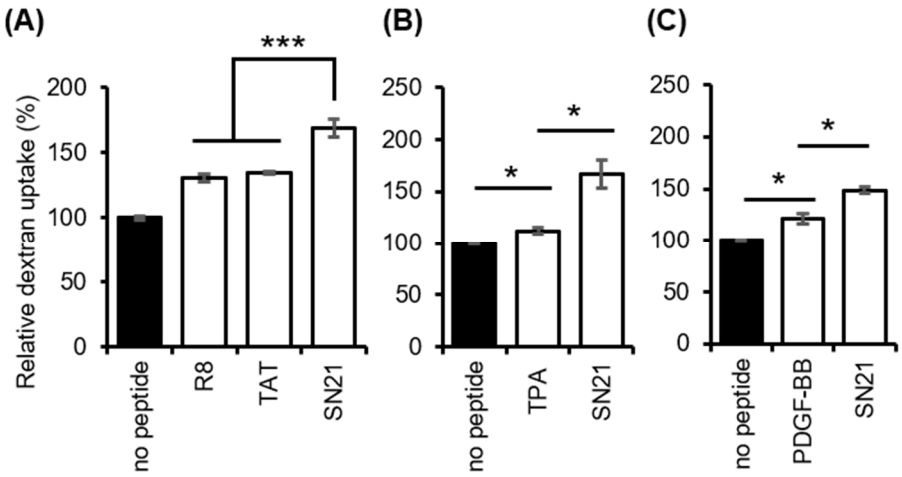

Figure 1–4. Comparison of Dex70-FL uptake induced by SN21 with other macropinocytosis inducers. Dex70-FL uptake induced by 5 μM SN21 compared to (A) 5 μM R8 or TAT, (B) 10 μM TPA, or (C) 500 ng/mL PDGF-BB. Data are presented as mean ± SE of three independent experiments [(A) one-way ANOVA followed by Tukey's *post-hoc* test; (B, C) *Student's t*-test; ***, $P < 0.001$; *, $P < 0.05$].

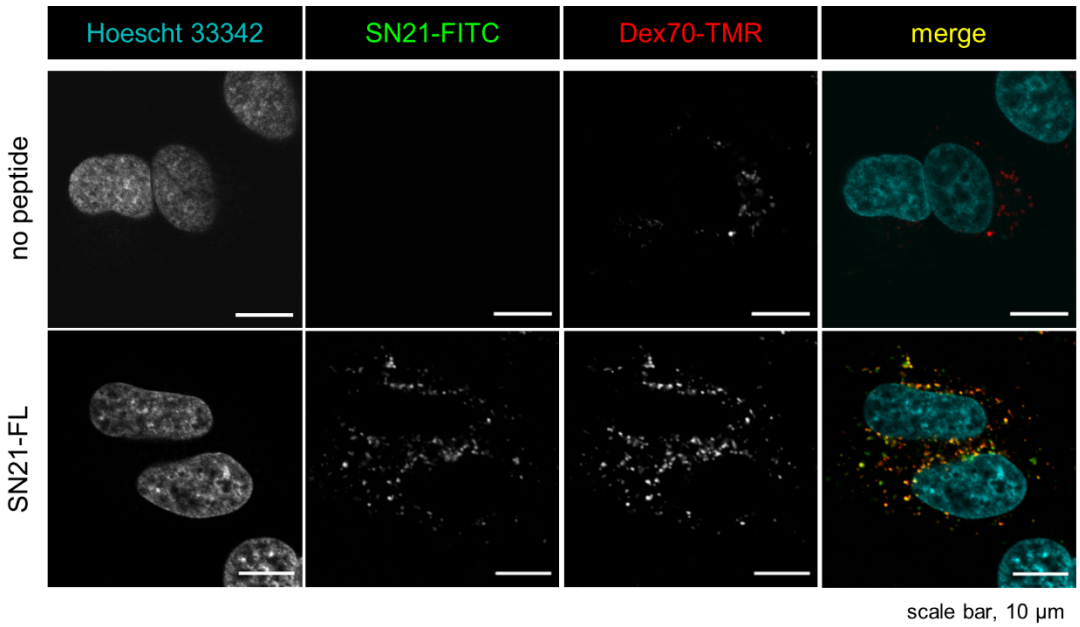

Figure 1–5. Colocalization of SN21-FITC and Dex70-TMR in HeLa cells treated with 5 μM SN21-FITC and 1 mg/mL Dex70-TMR in α-MEM (−) for 1 h. Observation performed using the FV1000 CLSM system (Olympus).

If SN21 is to be utilized as a tool for intracellular delivery, it is essential to compare the efficacy of this peptide for inducing macropinocytosis with other known inducers. Numerous accounts suggest macropinocytosis as among entry mechanisms for a human immunodeficiency virus type 1 (HIV-1) derived peptide TAT and R8, which are representative cationic CPPs.[6,42,43] Figure 1–4A shows ~33% and ~38% increase in dextran uptake in cells treated with 5 μM TAT and R8, respectively. However, SN21 yielded ~60% higher dextran uptake at the same concentration compared to no peptide control. In addition, SN21 showed better efficacy than 10 μM 12-*O*-tetradecanoylphorbol-13-acetate (TPA)[44] and 500 ng/mL platelet-derived growth factor (PDGF)-BB,[45] which increased dextran uptake by ~10% and ~30%, respectively, compared to no peptide treatment (Fig. 1–4B, C). These data collectively suggest the potential of SN21 as a macropinocytosis inducer and as a tool for intracellular delivery.

HeLa cells co-treated with fluorescein isothiocyanate-labeled SN21 (SN21-FITC) and tetramethylrhodamine-labeled 70 kDa (Dex70-TMR) showed their colocalization, suggesting co-internalization of SN21 with Dex70 (Fig. 1–5). This data also indicates that cargoes (represented by Dex70-TMR) are taken up into cells and are located within endosomes. Since SN21 cannot disrupt endosomal membranes, the cargoes could remain trapped and eventually be degraded in lysosomes without exerting their biological activities. To release the endocytosed cargoes to the cytosol, where their biological activities can be exhibited, a strategy facilitating endosome escape must be adopted.

II. Conjugation with membrane-lytic peptides enabled endosomal disruption

SN21 induces macropinocytosis to allow entry of biomacromolecules into endosomes. However, successful delivery requires the release of cargo molecules from endosomes to the cytosol. Cationic amphiphilic peptides offer a solution to achieve endosome escape.[22,46,47] These peptides form α-helical structures with both cationic hydrophilic and hydrophobic faces. The hydrophobic face interacts strongly with and disrupts lipid membranes, while the cationic hydrophilic face could provide selectiveness for endosomal membranes. It has been reported that endosomal membranes are rich in negatively-charged acidic lipids [e.g., bis(monoacylglycerol)phosphate (BMP)] over the plasma membrane, which is mainly composed of neutral and zwitterionic lipids.[48–51] The difference in lipid composition could be the reason for the strong interaction of cationic peptides, resulting in endosomal membrane perturbation. In previous works, CPPs conjugated with cationic amphiphilic peptides showed enhanced delivery of siRNA and proteins.[22,52–54] The fusion of such a membrane-lytic peptide with macropinocytosis-inducing peptides is expected to facilitate endosome escape. Namely, following the accumulation of this fusion peptide and cargo biomacromolecules within macropinosomes, the membrane-lytic component of the peptide should disrupt endosomal membranes to release the trapped cargoes.

SN21-LK15: KPVSLSYRCPCRFFESHVARA–GG–KLLKLLLKLLLKLLK-amide
macropinocytosis inducer (**SN21**) membrane-lytic peptide(**LK15**)

Figure 1–6. The primary structure of SN21–LK15 comprised of a macropinocytosis-inducing peptide and a membrane-lytic motif.

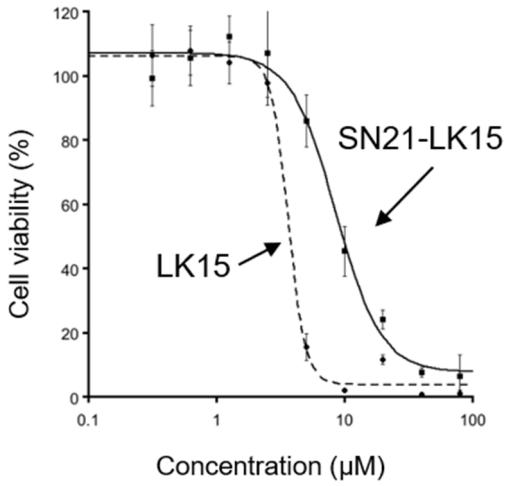

Figure 1–7. IC_{50} determination for LK15 (broken line) and SN21–LK15 (solid line). The viability of HeLa cells treated with 80, 40, 20, 10, 5, 2.5, 1.25, 0.625, 0.312, and 0 μM of peptides was determined by the WST–8 assay. Data are presented as mean ± SE of three independent experiments. IC_{50} was calculated using KaleidaGraph (ver. 4.01).

To test the above hypothesis, the membrane-lytic peptide LK15 (KLLKLLLKLLLKLLK)[55] was conjugated to SN21 via a glycylglycine spacer (SN21–LK15; Fig. 1–6). Cytotoxicity of the fusion peptide was analyzed using the mitochondrial dehydrogenase activity-based WST-8 assay.[56] LK15 is hemolytic and cytotoxic due to its strong interaction with lipid membranes regardless of its charge or composition.[57–59] Figure 1–7 shows the cytotoxicity curves of LK15 and SN21–LK15. The IC_{50} (concentration at which 50% of total cells are dead) of LK15 was 3.7 ± 0.2 μM, while SN21–LK15 was 8.5 ± 1.8 μM (Fig. 1–7), suggesting that the fusion of SN21 and LK15 substantially decreased the cytotoxicity. Increased cellular uptake of SN21–LK15 might reduce the cell-surface accumulation of SN21–LK15, resulting in the observed increase in IC_{50}.

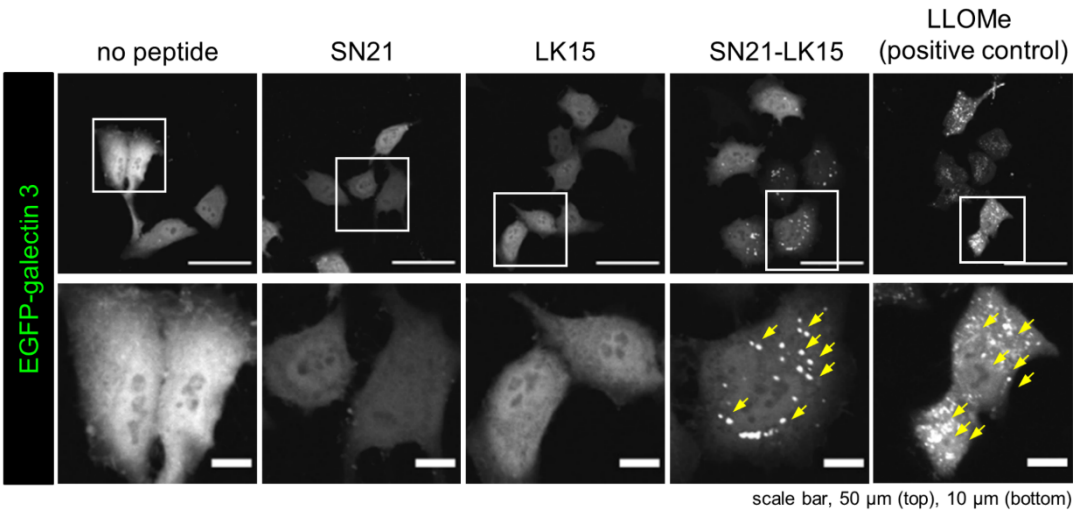

Figure 1–8. Detection of endosome rupturing by EGFP-galectin 3 accumulation assay. HeLa cells expressing EGFP-galectin 3 show fluorescent puncta (yellow arrows) after 30 min treatment with 2 μM SN21–LK15 and 1 mM LLOMe. Images were captured using the FV1000 CLSM system.

Once SN21–LK15 enters endosomes, it can disrupt endosomal membranes. This was evaluated by treating cells expressing galectin-3 fused with an enhanced green fluorescent protein (EGFP)[60] with SN21, LK15, and SN21–LK15. Galectin-3 is a β-galactoside-binding protein that accumulates on exposed sugar moieties within ruptured membranes.[61] When fused with a fluorescent protein, galectin-3 could serve as a probe to detect ruptured endosomal membranes, observed as fluorescent puncta across the cytosol. As a control, treating cells with the endosome destabilizing L-leucyl-L-leucyl methyl ester (LLOMe),[62] induced the expected fluorescent puncta (Fig. 1–8). Treatment with non-membrane disrupting SN21 showed no distinct fluorescent puncta (Fig. 1–8). The lack of puncta formation following LK15 treatment is an indication that LK15 is unlikely to enter endosomes. In striking contrast, SN21–LK15 induced fluorescent puncta, indicating its entry into endosomes and rupturing endosomal membranes.

III. Delivery of plasmid DNA and small interfering RNA

Endosome rupturing by SN21–LK15 suggests its capability to release cargoes into the cytosol. This peptide was first applied for nucleic acid delivery.

Complexation and condensation of nucleic acids is the first step towards cellular delivery of nucleic acids.[63,64] The amphipathic LK15 can condense nucleic acids but has low transfection efficiency.[55,65] Saleh et al. and Arthanari et al. offered a solution by conjugating LK15 with TAT to deliver plasmid DNA (pDNA)[53] and small-interfering RNA (siRNA),[54] respectively. It is, therefore, possible that SN21–LK15 also mediates nucleic acid delivery. The formation of a complex between SN21-LK15 and pDNA was first confirmed using a plasmid encoding EGFP (pEGFP-N1) as a model. Electrophoretic mobility shift assay (EMSA) was performed on EGFP-N1 combined with SN21–LK15 or LK15 at different charge ratios (total positive charges from peptides/negative charges from nucleic acid). The mobility of complexed nucleic acids (having larger molecular weights) in non-denaturing gels is retarded/shifted as compared to uncomplexed nucleic acids. When cationic peptides are used, the negative charge from the nucleic acids is also neutralized, preventing the migration of the nucleic acid. Like the free LK15, SN21–LK15 complexed with pEGFP-N1 from charge ratio 1 (Fig. 1–9A). Figure 1–9B shows confocal images of cells expressing EGFP following pEGFP-N1 delivery. SN21 did not deliver pDNA despite inducing macropinocytosis. Condensation helps nucleic acid to quickly be taken up into the cell through endocytic pathways, such as macropinocytosis. SN21–LK15 delivered pEGFP-N1 into cells resulting in ~54% of cells expressing EGFP, while LK15, which only complexes with pDNA, resulted in only ~14%.

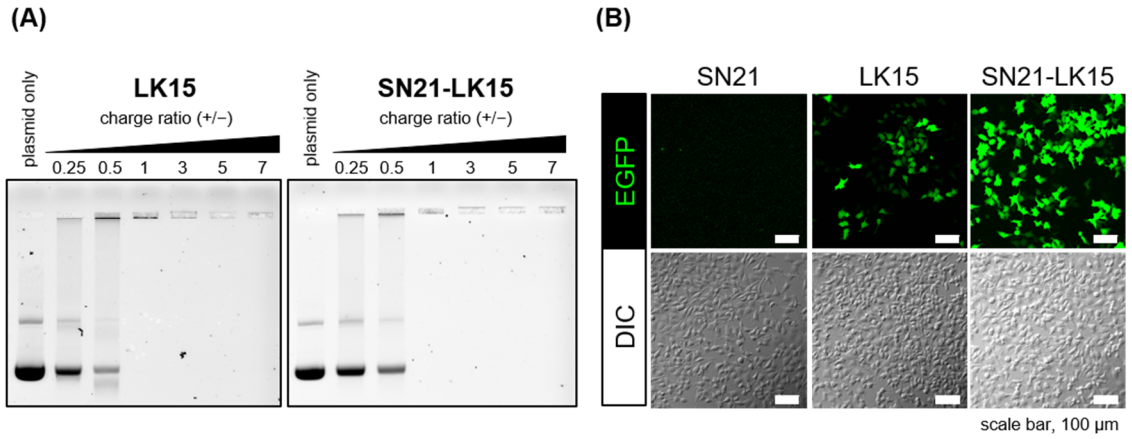

Figure 1–9. Delivery of plasmid DNA using SN21–LK15. (A) Electrophoretic mobility shift assay showing complexation of the pEGFP-N1 plasmid with LK15 or SN21–LK15. (B) HeLa cells transfected with 1 μg pEGFP-N1 using 10 μM SN21, LK15, or SN21–LK15, at charge ratio 5. Images were captured using the FV1000 CLSM system.

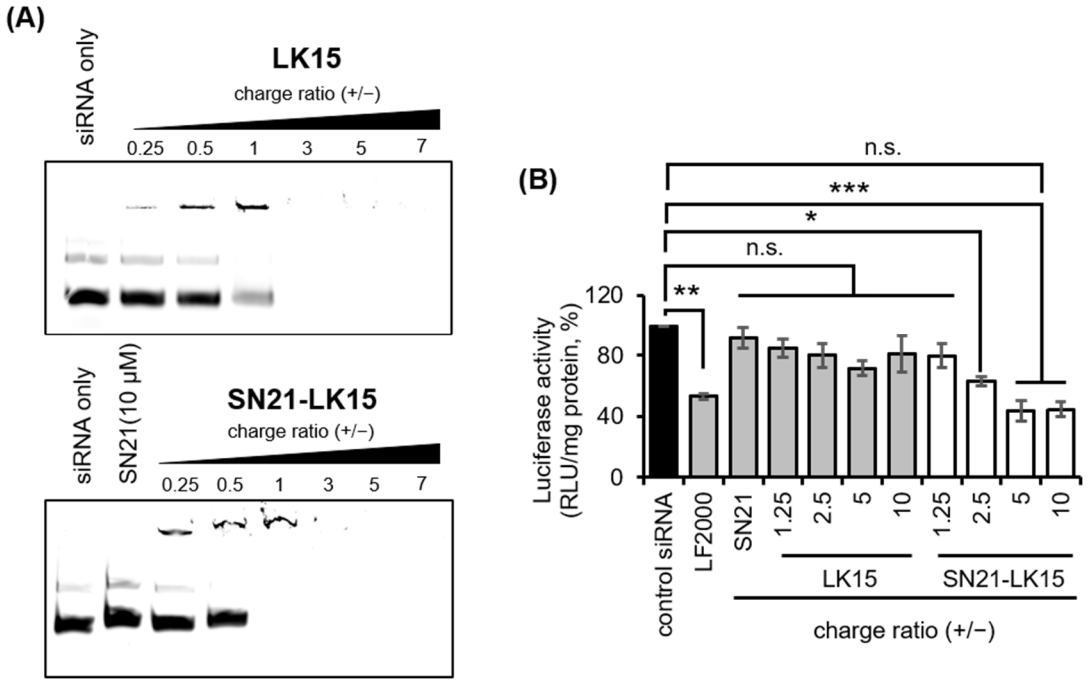

Figure 1–10. Delivery of siRNA using SN21–LK15. (A) Electrophoretic mobility shift assay showing complexation between BLOCK-iT Alexa Fluor Red Fluorescent Control siRNA and LK15 (upper panel) or SN21–LK15 (lower panel) at charge ratios 0.25, 0.5, 1, 3, 5, and 7. (B) Luciferase activity [relative light unit (RLU) per mg total protein] after transfecting HeLa-GL3 cells with 50 nM siLuc using LF2000, SN21, LK15, or SN21–LK15 at specified charge ratios. Data are presented as mean ± SE of three independent experiments (one-way ANOVA followed by Tukey's *post-hoc* test; ***, $P < 0.001$; **, $P < 0.01$; *, $P < 0.05$; n.s., not significant).

Next, the ability of SN21–LK15 to deliver siRNA was examined. Similar to pDNA, LK15, and SN21–LK15 was able to form complexes with siRNA (Fig. 1 – 10A). Transfection efficiencies using these peptides were confirmed by transfecting siRNA for luciferase gene (siLuc) into HeLa-GL3, with LF2000 as a positive control.[66] SN21–LK15 (charge ratio ≥ 2.5) delivered siLuc into HeLa-GL3 cells and significantly decreased luciferase activity expressed as relative light unit per mg of total protein (Fig. 1–10B). Increasing the charge ratio to 5 and 10 further decreased luciferase activity, comparable to an established transfection reagent, Lipofectamine 2000 (LF2000). Without SN21 fusion, siLuc transfection using LK15 resulted in an insignificant knockdown of the luciferase activity.

Similarly, the delivery of KRAS siRNA was also performed. KRAS is highly associated with cell proliferation and is a molecular target for RNA interference-based therapies.[67] Efficient delivery of KRAS siRNA should show the potential of SN21–LK15 as a transfection reagent for therapeutic nucleic acids. Western blot analysis shows decreased KRAS protein expression in cells transfected with KRAS siRNA using LF2000 and SN21–LK15 (Fig. 1–11A). Decreased KRAS expression decreased the cell proliferation of transfected HeLa cells determined by the WST-8 assay (Fig. 1–11B, C).

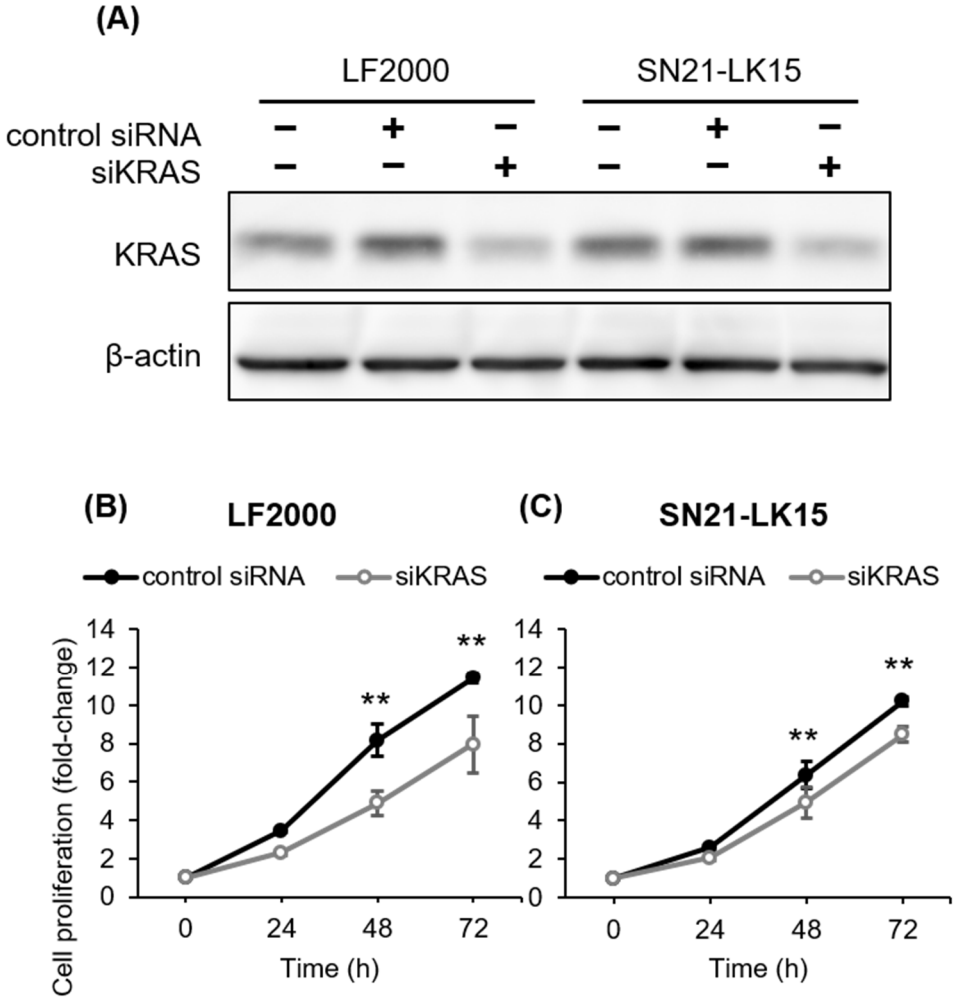

Figure 1−11. Delivery of KRAS siRNA using SN21–LK15. HeLa cells were transfected with control or KRAS siRNA using LF2000 or SN21-LK15 (charge ratio 5). The efficiency of KRAS siRNA transfection was determined by (A) western blot analysis of KRAS protein expression and (B) cell proliferation after 0, 24, 48, 72 h post-transfection. Data are presented as mean ± SE of three independent experiments (Student's *t*-test; **, $P < 0.01$).

IV. Delivery of antibodies and genome-editing proteins

Intracellular delivery of antibodies should help in understanding the biological relevance of protein-protein interactions within cells and show a significant impact as a current therapeutic approach.[68] The ability of this peptide to deliver antibodies was examined. HeLa cells were treated with 100 μg/mL of Alexa Fluor 488-labeled immunoglobulin G (IgG-AF488) in the presence of SN21, LK15, or SN21–LK15. Confocal microscopy images showed dot-like, punctate signals, together with fluorescent signals uniformly distributed throughout the cytoplasm in cells treated with 2 μM SN21–LK15, but not with SN21 or LK15 (Fig. 1–12A).

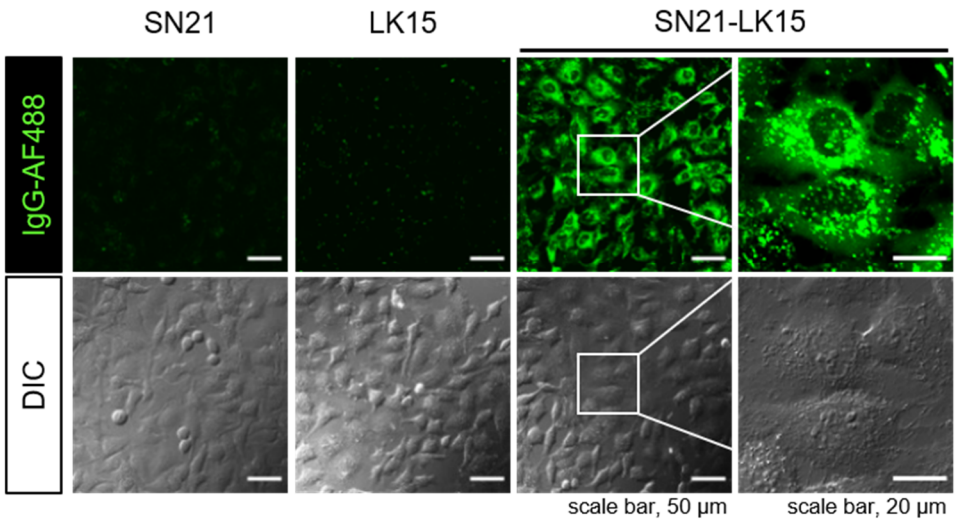

Figure 1–12. Antibody delivery using SN21–LK15. HeLa cells treated with 100 μg/mL IgG-AF488 shows diffuse signals throughout the cytoplasm (endosomal released) and fluorescent puncta (endosome trapped) signals after treatment with 2 μM SN21–LK15. Images were captured using the FV1000 CLSM system.

To know if IgGs delivered by SN21–LK15 retained the antigen-binding ability, HeLa cells were treated with Alexa Fluor 594-labeled anti-nuclear pore complex IgG (anti-NPC-AF594) (50 μg/mL) in the presence of 2 μM SN21–LK15. Figure 1–14 shows labeling of the nuclear periphery after treatment of anti-NPC-AF594 in the presence of 2 μM SN21–LK15 (yellow arrows, upper panels; nucleus stained with Hoechst 33342). Such staining was not observed in cells treated with control IgG-AF594 (Fig. 1–14, lower panels). Observing intracellular targeting confirms that the diffuse IgG signals in Fig. 1–12 and 1–13 are intact functional IgGs and are not by-products of lysosomal protein degradation. These findings suggest the applicability of SN21–LK15 to deliver biofunctional protein cargoes.

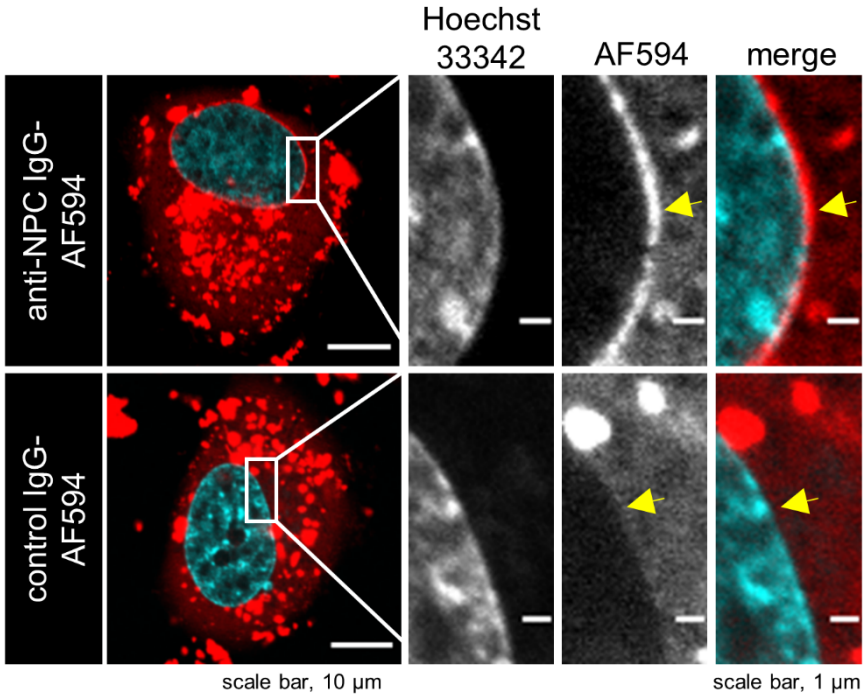

Figure 1–13. Antibodies delivered by SN21–LK15 retain the antigen-binding ability. HeLa cells were treated with 50 μg/mL Alexa Fluor 594-labeled anti-nuclear pore complex IgG (anti-NPC-AF594) or control IgG-AF594 with 2 μM SN21–LK15 for 1 h. Yellow arrows indicate the nuclear boundary. Observation was performed using the FV3000 CLSM system.

Applications of SN21-LK15 for intracellular protein delivery was also tested using the two genome-editing proteins, namely, Cre recombinase and an artificial transcription activator protein (TALE-VP64). The delivery of Cre recombinase was assessed using a Cre-loxP recombination assay system (Fig. 1–14A).[12,22,71] Briefly, HeLa cells transiently transfected with the *loxP-DsRed-loxP-EGFP-N1* reporter initially express the red-fluorescent protein, DsRed. When Cre is delivered, the DsRed coding region flanked by two loxP sites will be removed to allow the expression of EGFP. Cells were treated with Cre (5 μM) in the presence of 3 μM SN21–LK15 for 1 h, followed by protein washout and incubation for another 24 h. This treatment resulted in 59% recombination (the percentage of EGFP-positive cells over total fluorescence emitting cells) (Fig. 1–14B, C). Treatment with the same concentration of Cre in the presence of 5 μM SN21 or 2.5 μM LK15 only yielded 10% and 21% recombination, respectively.

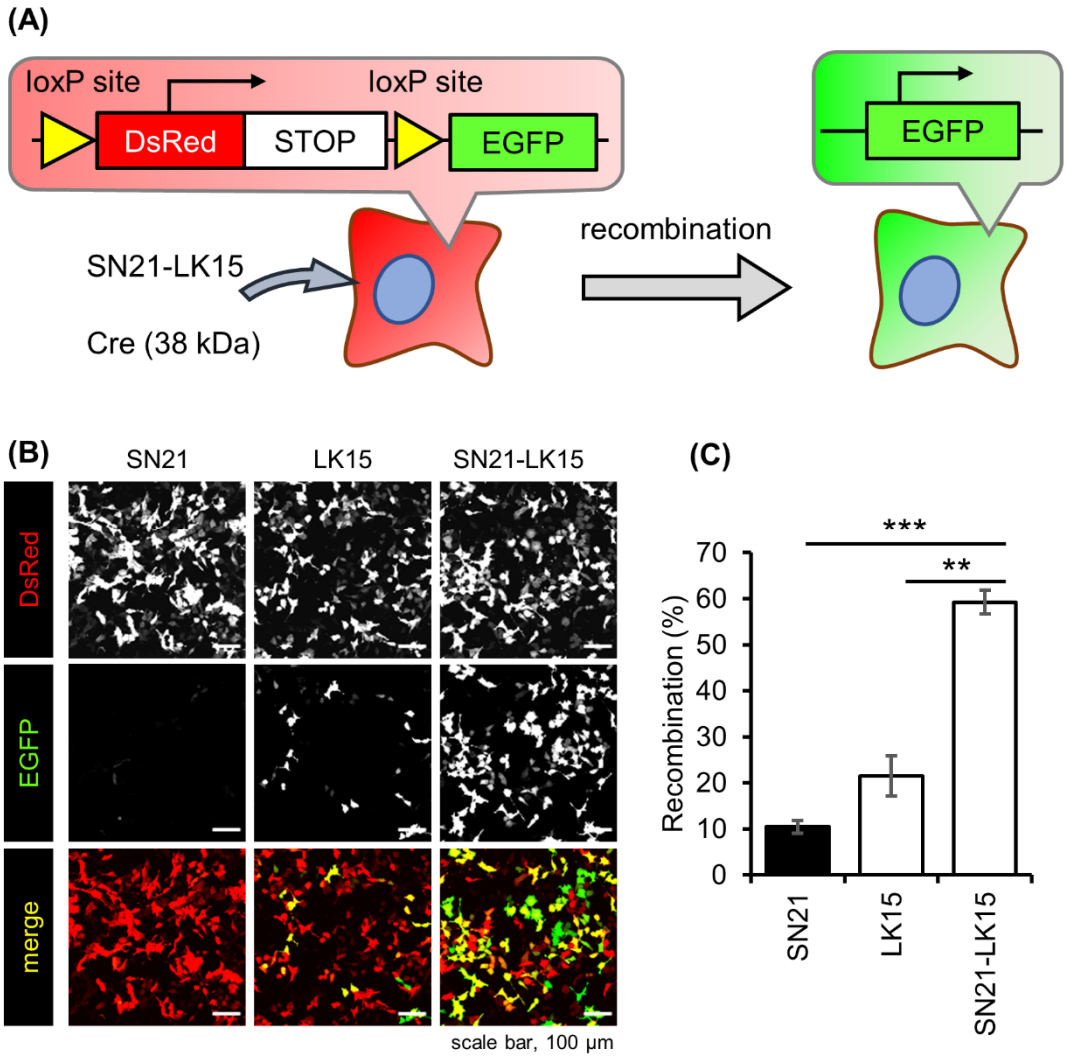

Figure 1–14. Cre recombinase delivered by SN21-LK15. (A) Cre recombinase assay. (B) Microscopic observation of HeLa cells transfected with *loxP-DsRed-LoxP-EGFP* reporter plasmid treated with 5 μM Cre recombinase and SN21, LK15, or SN21–LK15. (C) Recombination rates (the percentage of EGFP-expressing cells over the total number of fluorescent cells) after Cre delivery using SN21, LK15, or SN21–LK15. Data are presented as mean ± SE of around 3000 counted cells across three independent experiments (one-way ANOVA followed by Tukey's *post-hoc* test; ***, $P < 0.001$; **, $P < 0.01$).

SN21–LK15 can also deliver the artificial transcription activator TALE-VP64. Transcription activator-like effectors (TALEs) are designable DNA binding proteins that bind to specific DNA segments (Fig. 1–15).[72] TALEs are useful tools for genome manipulation when combined with nucleases or transcription activators.[73–75] For this experiment, a model transcription activator dHax3-VP64 was used. This fusion protein is comprised of a *de novo* designed artificial TALE (dHax3), recognizing a specific DNA segment of 12 base pairs[74,76] and VP64 transcription activation domains.[77] This protein is delivered into stable HeLa cells carrying a luciferase reporter gene under the control of a dHax3 TALE binding sequence (TBS) upstream of a minimal promoter[76] (HeLa-TBS-Luci; Fig. 1–15A). Cytosolic translocation and binding of TALE-VP64 to the binding sequence allows the expression of luciferase, which is measured as a function of luminescence. Around 90-fold increase in luminescence was obtained by treating HeLa-TBS-Luci with 1 μM TALE-VP64 in the presence of 2 μM SN21–LK15, compared with no peptide or SN21 treatments, which only yielded minimal luciferase activity (Fig. 1–15B). The previously designed endosomolytic peptide L17E[47] elicited a less than 10% increase in luminescence under the given condition. L17E induces membrane ruffling and transiently disrupts the ruffled membranes to allow materials to enter the cell.[78] Due to this mechanism, using L17E requires high concentrations of cargoes (300-500 μg/mL of IgG or 5 μM of bioactive proteins) to deliver cargoes. Considering that this assay only used 1 μM of TALE-VP64, L17E was found inefficient. Similar to SN21, TAT also induces macropinocytosis (Fig. 1–4).[42] The LK15-conjugated version of this peptide (TAT–LK15) may have structural/functional similarity with SN21–LK15. Despite only being reported for nucleic acid delivery,[53,54] TAT–LK15 also promoted the uptake of TALE-VP64. However, the data show that

using SN21–LK15 for delivery resulted in higher luminescence than using TAT–LK15 (Fig. 1–15C). This tendency is consistent with the data shown in Figure 1–4, which may support the idea that high macropinocytosis induction by SN21 leads to better cytosolic delivery of the bioactive molecules.

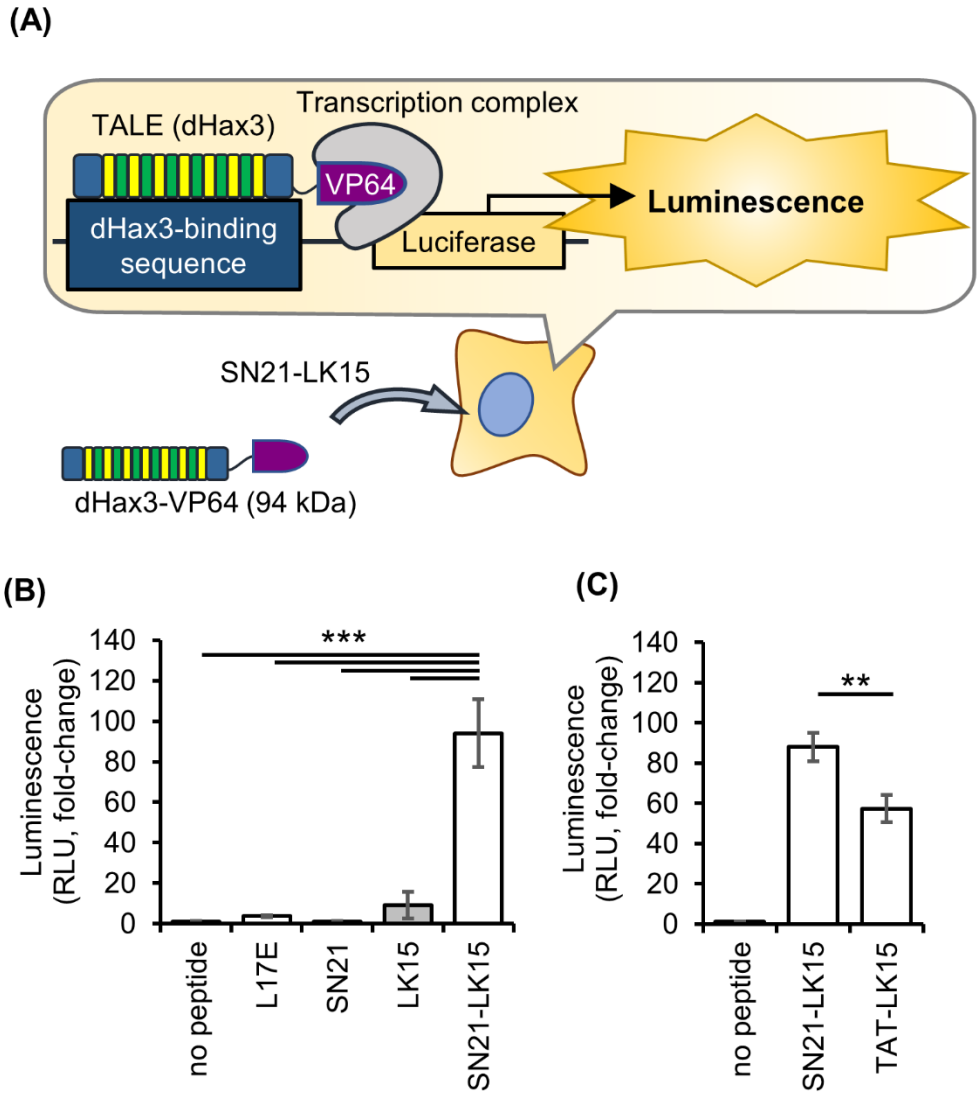

Figure 1–15. Delivery of TALE-VP64 by SN21–LK15. (A) TALE-VP64 delivery assay scheme. (B) Luciferase activities of HeLa-TBS-Luci cells treated with 1 μM TALE-VP64 in the presence of 40 μM L17E, 5 μM SN21, 2.5 μM LK15, or SN21–LK15. (C) Comparison of the efficiency of TALE-VP64 delivery using SN21–LK15 and TAT-LK15. Data are presented as mean ± SE of three independent experiments (one-way ANOVA followed by Tukey's *post-hoc* test; ***, $P < 0.001$; **, $P < 0.01$)

V. SN21–LK15 delivers cargoes by inducing macropinocytosis

Lastly, the pathway of endocytosis, including macropinocytosis, and endosomal escape in SN21–LK15-mediated delivery, were analyzed. Treatment of cells at 4°C (i.e., the temperature at which endocytosis is suppressed; Fig. 1–16A),[23] as well as in the presence of EIPA (Fig. 1–16B), prevented SN21–LK15-mediated IgG-AF488 uptake. Although the presence of endosome-trapped signals persisted, these data suggest the requirement of endocytosis (particularly macropinocytosis) for efficient intracellular delivery.

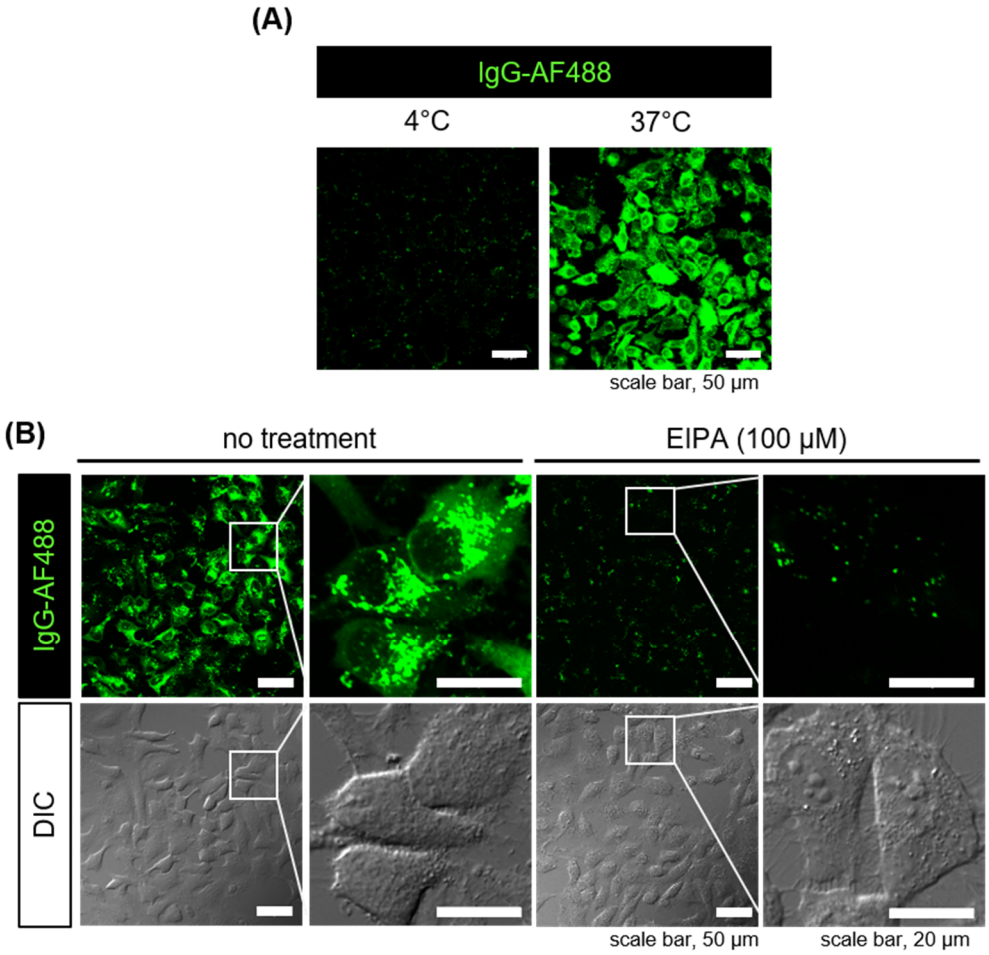

Figure 1–16. Macropinocytosis-induced delivery of SN21–LK15. Incubation of 2 μM SN21–LK15 with 100 μg/mL IgG-AF488 in (A) 4 °C and in the presence of (B) 100 μM EIPA blocked the delivery of IgG-AF488. Images were captured using the FV1000 CLSM system.

The number of cells with diffuse cytoplasmic IgG-AF488 signals increased by increasing incubation time (30 min and 60 min incubation resulted in 35% and 61%, respectively) (Fig. 1–17A). In addition, blocking early-to-late endosome maturation using bafilomycin A1[69] decreased the number of cells with diffuse cytoplasmic signals by ~30% (Fig. 1–17B, C). These findings indicate that endosome maturation and accumulation should be necessary for SN21–LK15 to achieve its intracellular delivery function. Endosome maturation results in decreased intraluminal pH and endosome fusion, accompanied by the accumulation of endocytosed cargoes.[70] During this stage, SN21–LK15 and its accompanying cargo should increase in concentration within maturating endosomes, eventually resulting in the disruption of endosome membranes and the release of endocytosed cargoes.

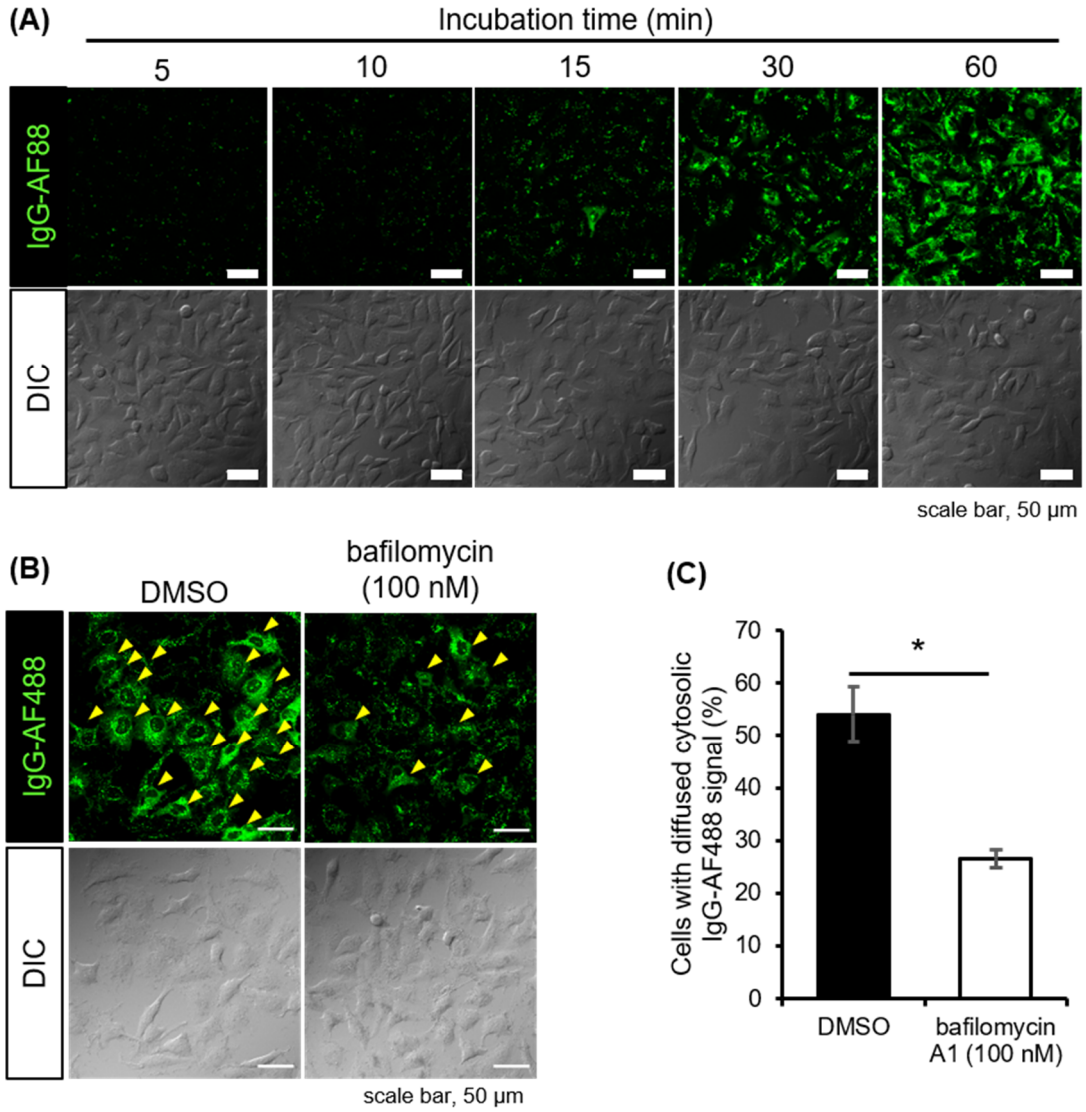

Figure 1–17. SN21–LK15-mediated delivery of IgGs requires endosome maturation. (A) Increasing intracellular IgG-AF488 signal observed in increasing incubation (5, 10, 15, 30, and 60 min) of 0.1 mg/mL IgG-AF488 and 2 μM SN21–LK15 in α–MEM (−). (B, C) Bafilomycin A1 treatment reduced the number of cells showing diffuse cytoplasmic IgG-AF488 signals (yellow arrows). Data are presented as the mean of the percent of cells with diffuse signals ± SE among 1080 counted cells across four biological replicates (Student's *t*-test. *, $P < 0.05$)

Discussion

This chapter illustrates the concept of combining a macropinocytosis-inducing peptide with a membrane-lytic peptide to deliver functional cargoes into cells. Firstly, SN21, a peptide derived from the N-terminal region of SDF-1α, showed induction of macropinocytosis. This peptide contains the receptor-binding (RFFESH) and receptor-activating (KPVSLSYR) motifs from SDF-1α, which are necessary for activating CXCR4.[34] Loetscher et al. suggested that peptides derived from SDF-1α having these motifs showed agonistic activity,[35] and Filippo et al. showed that peptides from the N-terminal region of SDF-1α activate chemotaxis and proliferation in both neuroblastomas and CXCR4-expressing cells.[36] The dextran uptake induction exhibited by SN21 in Figure 1–2 were consistent with the previous studies mentioned above. More importantly, SN21 was comparable with SDF-1α with respect to macropinocytosis induction (Fig. 1–3).

Although SN21 showed the ability to induce macropinocytosis and allowed cargoes (represented by Dex70-TMR) to be internalized into endosomes (Fig. 1–5), the cargoes were retained within the endosomes. To enable the release of cargoes from endosomes, SN21 was conjugated to a membrane-lytic peptide LK15 (SN21–LK15).[55] Damage on the plasma membrane may result in cell death. LK15 has strong membrane-lytic activity,[57] thus, IC_{50} was reached at the range of 3.7 ± 0.2 μM. SN21–LK15 showed less cytotoxicity (8.5 ± 1.8 μM). The decreased cytotoxicity could be due to less plasma membrane disruption due to the ability of SN21 to induce macropinocytosis, allowing the peptide to enter the cell. The accumulation of EGFP-galectin 3 on ruptured endosomes after SN21–LK15 treatment should suggest (1) entry of the peptide into

endosomes, and (2) the ability of the SN21–LK15 to rupture endosomal membranes (Fig. 1–8). Since it was observed to disrupt endosome membranes, SN21–LK15 should be capable of delivering bioactive cargo molecules.

SN21–LK15 successfully delivered nucleic acids (pDNA, and siRNAs) and proteins (IgGs, Cre recombinase, and TALE-VP64) into cells. LK15 can perform nucleic acid complexation but was less efficient in delivery than SN21–LK15 due to the lack of the SN21 segment to facilitate macropinocytic uptake (Fig. 1–9, 10). To deliver nucleic acids, the delivery agent should complex with nucleic acid cargoes and should facilitate endocytic uptake.[64] SN21–LK15 has both the nucleic acid complexation ability and macropinocytosis inducing ability, which made this peptide capable of nucleic acid delivery. Also, protein delivery was achieved using SN21–LK15 with 100 μg/mL for IgG. This concentration of cargoes was relatively lower (up to 5× lower) than the amount needed when using the attenuated cationic amphipathic lytic peptide L17E (500 μg/mL antibody), suggesting an advantage over the L17E strategy.[47] Furthermore, the delivery of different cargoes having different properties (such as nucleic acids and proteins) showed the versatility of using SN21–LK15 for intracellular delivery. Simple administration of this peptide should be beneficial for the delivery of intact nucleic acids and proteins, without the need for cross-link formation.

Finally, the observed efficacy of SN21–LK15 can be attributed to the induction of macropinocytosis. Figure 1–16 shows that cytosolic delivery of antibodies was inhibited by a decrease in temperature (4 °C) and in the presence of the macropinocytosis inhibitor EIPA, suggesting that SN21–LK15-mediated cargo delivery requires endocytosis, in particular, macropinocytosis. The high cytotoxicity of LK15 suggests that this peptide can rupture membranes to allow cargoes to enter the cells through the

disrupted plasma membrane (Fig. 1–7). However, Figure 1–17A shows that at least 30 min of incubation is required before observing the cytoplasmic fluorescent antibody signal, suggesting that the delivery performed by SN21–LK15 is not due to plasma membrane disruption. Additionally, Figure 1–17B and C data show that blocking the early-to-late endosome maturation suppressed SN21–LK15-mediated delivery of antibodies. These data suggest that endocytic uptake by macropinocytosis is performed by SN21–LK15 to deliver cargoes into the cell, and endosome maturation is required to release the cargoes into the cytosol.

Overall, this chapter shows the identification of a macropinocytosis-inducing peptide and its use as an intracellular delivery strategy for biomacromolecules. The data showing successful delivery of proteins even at relatively lower cargo concentration is encouraging since this could imply the possibility of reducing the amount of cargoes used for delivery – a salient feature for the delivery of precious samples, including antibodies.

Chapter Two:
Important Chemical Species and Their Mechanism to Activate Macropinocytosis

第 2 章

マクロピノサイトーシス活性化に重要な化学種と作用機序

The study in the previous chapter identified the macropinocytosis-inducing peptide, SN21, which is able to deliver nucleic acids and bioactive proteins into cells when combined with a membrane-lytic peptide, LK15. In this chapter, the mode of macropinocytosis activation mediated by SN21 was investigated (Fig. 2–1). First, it was found that CXCR4 is unlikely to be involved in macropinocytosis induced by SN21. Analysis of the structure-activity relationship revealed the importance of two Cys residues of the canonical CXC motif in the SN21 peptide for macropinocytosis activation. The peptide corresponding to positions 7 to 14 of SN21 was suggested to be the key residues, and substitution of the Pro residue between the two Cys residues to Ala (P4A) further facilitated macropinocytosis. Dextran uptake assays and phosphorylation signaling analyses[79] were performed to confirm macropinocytosis induction by the identified peptides. More importantly, HPLC analyses revealed that P4A undergoes disulfide exchange reactions facilitated by amino acids within the media, resulting in the formation of more potent forms. The findings in this chapter offer a possible mechanism for the activities of identified macropinocytosis-inducing peptides and describe the influence of the chemical species within the extracellular environment on the activities of administered peptides.

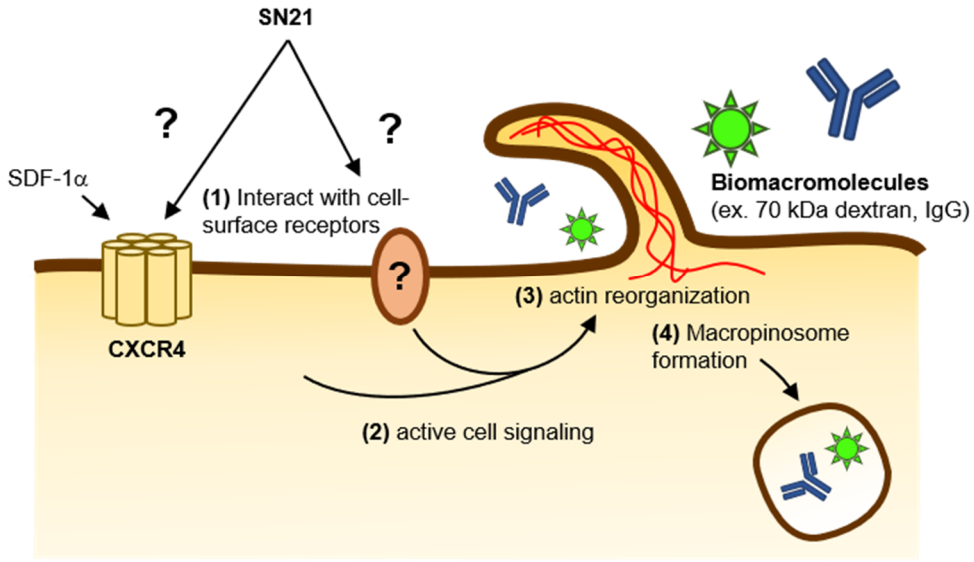

Figure 2–1. Potential induction mechanism of identified macropinocytosis-inducing peptide. (1) Interaction with cell-surface elements should (2) activate intracellular signaling, resulting in (3) reorganization of the actin cytoskeleton and (4) macropinosome formation.

I. Macropinocytosis activation by SN21 is independent of CXCR4

SN21 consists of the receptor activating (KPVSLSYR) and receptor binding (RFFESH) motifs from SDF-1α, which are needed for this chemokine to interact and activate CXCR4.[32,33,80] To evaluate the interaction of SN21 with CXCR4, a NanoBRET-based competition assay was performed.[81] This assay relies on the principle of bioluminescence resonance energy transfer (BRET) between a luminescent donor and a fluorescent acceptor. This system uses a NanoLuc luciferase, a structurally optimized luciferase from *Oplophorus gracilirostris*,[82] fused with CXCR4 at the N-terminus (exposed on the extracellular side) proximal to its ligand-binding region as the luminescence donor.[33] In the absence of a CXCR4 ligand, TAMRA-labeled Ac-TZ14011, a CXCR4 antagonist,[83] attaches onto the proximal binding site (~10 nm). Enzymatic oxidation of furimazine by NanoLuc causes energy transfer to the fluorescent acceptor TAMRA in close proximity, resulting in fluorescence emission.[84] Competition between the binding of co-administered CXCR4 ligands and TAMRA-Ac-TZ14011 decreases the observed BRET, which is shown as an increase in CXCR4-binding inhibition (Fig. 2–2A). In this assay, the CXCR4 antagonist FC131[85] (IC_{50} < 10 nM) and SDF-1α were used as positive controls and a non-binding peptide (IGLMV-amide) and a D-isomer of SN21 (dSN21) as negative controls. D-type peptides are unlikely to interact with the native receptor very tightly, but since it contains the same amino acid sequence, dSN21 should share the chemical properties of L-type SN21. This assay revealed that SN21 exhibited a lower CXCR4 inhibition compared to SDF-1α, suggesting that SN21 only weakly interacts with CXCR4 (Fig. 2–2B).

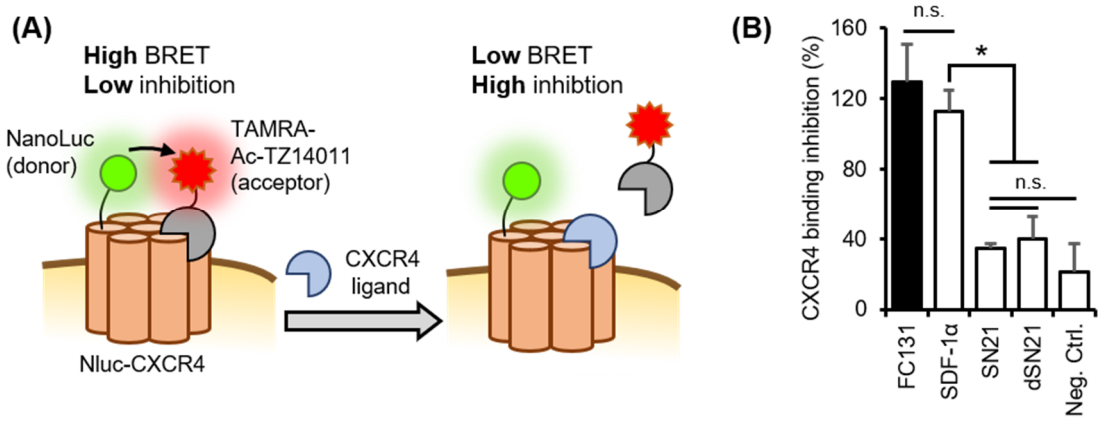

Figure 2–2. Evaluation of SN21 interaction with CXCR4. (A) NanoBRET-based CXCR4 interaction assay. CHO cells expressing Nluc-CXCR4 (luminescence donor) are treated with TAMRA-Ac-TZ14011 (fluorescent acceptor) in the presence of CXCR4 ligands. (B) An increase in BRET (expressed as CXCR4 binding inhibition) is observed in the co-treatment of cells with CXCR4 ligands (FC131 and SDF-1α). SN21, dSN21, and negative control peptides (IGLMV-amide, Neg. Ctr.) showed significantly lower CXCR4 inhibition compared to SDF-1α. Data are presented as mean ± SE of three independent experiments (one-way ANOVA followed by Tukey's *post-hoc* test; *, $P < 0.05$; n.s., not significant).

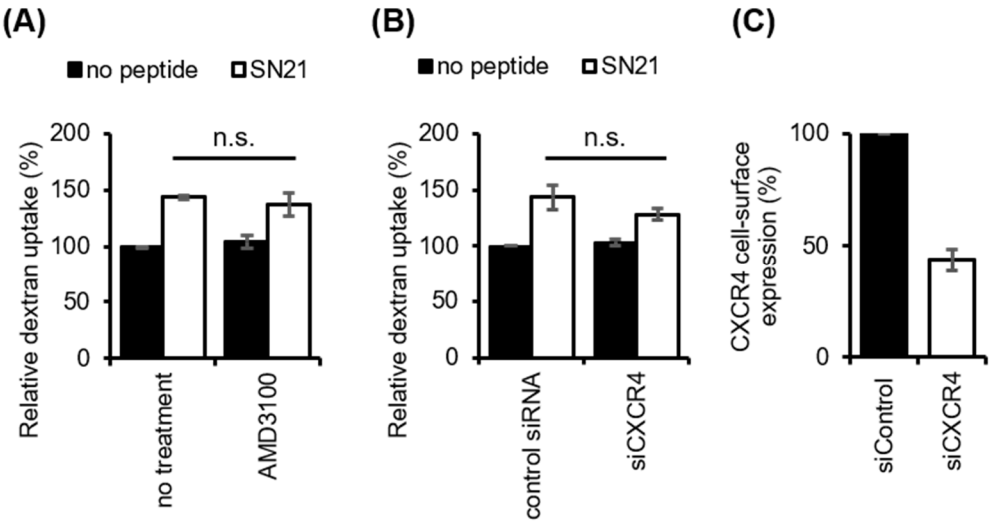

Figure 2–3. SN21-induced 70 kDa dextran uptake may not involve CXCR4. Dex70-FL uptake induced by 5 μM SN21 in (A) HeLa cells pretreated with 5 μM AMD3100 and in (B) CXCR4-knockdown cells. (C) Confirming CXCR4 expression knockdown by immunofluorescence flow cytometry. Data are presented as mean ± SE of three independent experiments (one-way ANOVA followed by Tukey's *post-hoc* test; n.s., not significant).

Dextran uptake experiments also showed that SN21-induced 70kDa dextran uptake was unaffected in the presence of a CXCR4 inhibitor AMD3100 (Fig. 2–3A) or by the siRNA-mediated knockdown of CXCR4 (Fig. 2–3B). These findings contradict the initial assumption that SN21 may activate macropinocytosis through CXCR4.

II. SN21 requires its Cys residues to activate macropinocytosis

The structure-activity relationship was examined to identify key amino acid residues for the activity of SN21 to induce macropinocytosis. SDF-1α contains two intramolecular disulfide bridges (Cys9-Cys34 and Cys11-Cys50).[86] Since SN21 does not contain Cys34 or Cys50, mutations of Cys9 and Cys11 could have minimal effect on its macropinocytosis-inducing ability. To test this, Cys-to-Ala mutants (C9A, C11A, and C9A/C11A) of SN21 were synthesized (Fig. 2–4A) and analyzed for their ability to induce dextran uptake. As shown in Figure 2–4B, however, none of the Cys-to-Ala mutants could induce dextran uptake. Interestingly, even a single Cys-to-Ala mutation on SN21 (C9A and C11A) was enough to abolish the dextran uptake induction by SN21.

Western blot analysis of signaling proteins related to macropinocytosis activation should indicate macropinocytosis activation (Fig. 2–4C).[87,88] Macropinocytosis is triggered by extracellular stimuli, such as binding of ligands (e.g., SDF-1α) to its receptor to activate phosphoinositide 3-kinase (PI3K). Activated PI3K converts phosphatidylinositol 4,5-bisphosphate [PtdIns(4,5)P_2] to phosphatidylinositol 3,4,5-trisphosphate [PtdIns(3,4,5)P_3], which leads to downstream phosphorylation of Akt(S473) (P-Akt) and conversion of Rac1 from an inactive GDP-bound form to an active GTP-bound form (Fig. 2–4C).[79,88] Thus, increased P-Akt and active Rac1 levels suggest macropinocytosis induction. Figure 2–4D shows increased P-Akt and active Rac1 levels in cells treated with SDF-1α and SN21. By contrast, C9A/C11A showed no apparent increase in the P-Akt or active Rac1 level, suggesting that the lack of dextran uptake-inducing ability of Cys-to-Ala mutants was due to the lack of macropinocytosis signal activation.

Rac1 activation facilitates reorganization of the actin cytoskeleton, leading to dynamic membrane ruffling, lamellipodia formation, and macropinocytosis.[20] Thus, the treatment of cells with peptides with the ability to activate Rac1 might lead to dynamic reorganization of the actin cytoskeleton. To address this possibility, HeLa cells stably expressing filamentous actin-binding Lifeact-mCherry (lm-HeLa) were treated with the peptide and subjected to a time-lapse recording. When lm-HeLa cells were treated with 5 μM SN21, the cytoskeletal reorganization and membrane ruffling were observed (Fig. 2–4D, upper panel, white arrow). By contrast, a minimal reorganization was observed in cells treated with the C9A/C11A peptide (Fig. 2–4D, lower panels). Thus, the data on dextran uptake, Akt and Rac1 activation, and reorganization of the actin cytoskeleton together support the ability of SN21 to induce macropinocytosis. Furthermore, these data also show the potential importance of the Cys residues in the SN21 peptide.

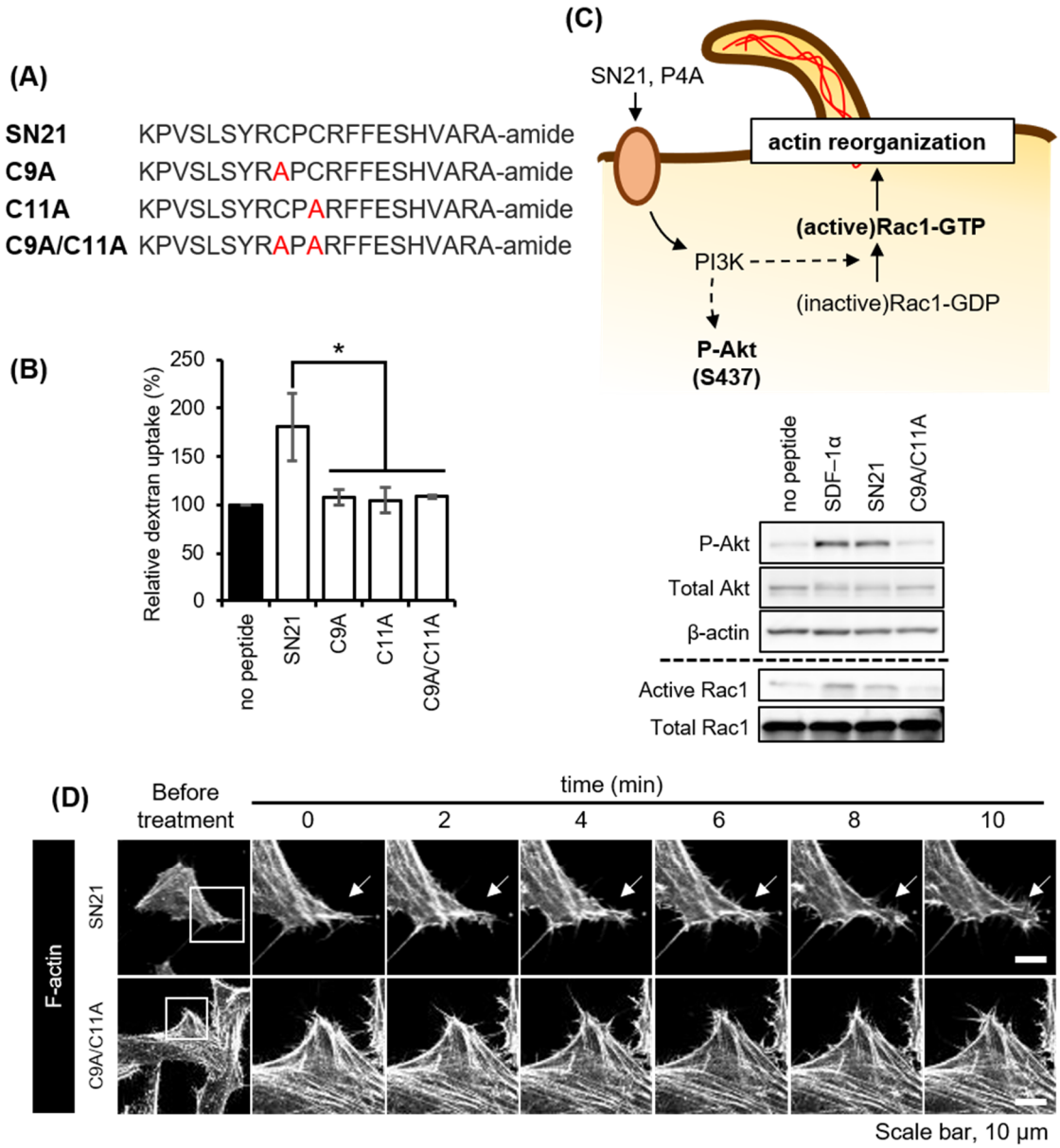

Figure 2–4. Cys-to-Ala mutations in the SN21 peptide abrogate its ability to induce macropinocytosis. (A) Sequences of SN21 and its Cys-to-Ala mutants. (B) Dextran uptake in HeLa cells treated with 5 μM SN21 and its Cys-to-Ala mutants and with 0.5 mg/mL Dex70-FL in α–MEM (−) for 30 min. Data are presented as mean ± SE of three independent experiments (Student's *t*-test; *, $P < 0.05$). (C) Hypothesized scheme of macropinocytosis induced by SN21 and western blot analysis of P-Akt and active Rac1 levels (representative data of n=3). (D) Time-lapse analysis of reorganization of the actin cytoskeleton confirms the loss of lamellipodia formation by the Cys-to-Ala mutation. Images were captured using the FV3000 CLSM system.

Cysteine contains a sulfhydryl group that can generate nucleophilic thiolates when deprotonated.[89] To examine whether the reaction of Cys thiols of SN21 with extracellular thiols species contributes to the observed macropinocytosis activation, the SN21 peptide was chemically modified. Alkylation of thiols using iodoacetamide (alkyl-SN21) blocks its reactivity, whereas pyridinesulfenylation using 2-mercaptopyridine (PyS-SN21) generates activated disulfide, which can easily react with free extracellular thiol species (Fig. 2–5A). PyS-SN21 could induce Dex70-FL uptake comparable to that of SN21. By contrast, alkyl-SN21 had a significantly reduced ability to induce Dex70-FL uptake (Fig. 2–5B). These data suggest that Cys thiols of SN21 might contribute to its ability to activate macropinocytosis.

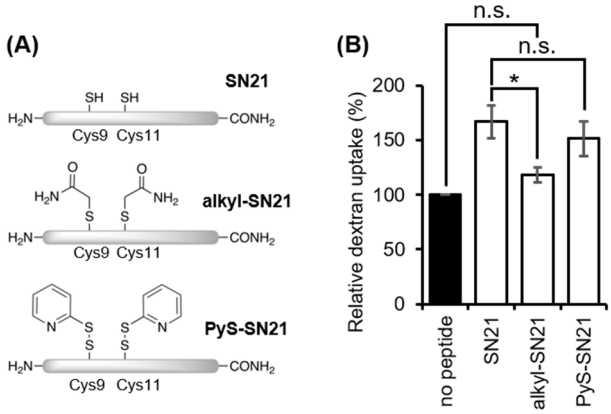

Figure 2–5. Chemical modifications on the Cys residues of SN21 affect dextran uptake. (A) Schematic diagrams of unmodified, alkylated, and pyridinesulfenylated SN21 showing the chemical modifications on respective Cys residues. (B) Dex70-FL (0.5 mg/mL) uptake in HeLa cells treated with 5 μM SN21, alkyl-SN21, or PyS-SN21. Data are presented as mean ± SE of three independent experiments (Student's *t*-test; *, $P < 0.05$; n.s., not significant).

III. Shorter derivatives of SN21 induce macropinocytosis and require Cys residues

To determine residues important for the macropinocytic dextran uptake activity other than the Cys residues, alanine scan mutants of SN21 were synthesized (Fig. 2–6A) and subjected to the examination of their ability to induce dextran uptake. Mutations of residues between Tyr7 and Phe14 significantly decreased the dextran uptake induction compared with the original SN21 peptide (Fig. 2–6B), indicating the importance of these residues for the macropinocytosis activation of SN21. Note that the Y7A, R8A, R12A, F13A, and F14A mutations decreased but did not abolish the uptake induction when compared to the dextran uptake induced by SN21 treatment and no peptide treatment (gray and black columns, respectively; Fig. 2–6). Thus, together with the data from Figure 2–4, Cys9 and Cys11 are essential for, and Tyr7, Arg8, Arg12, Phe13, and Phe14 make contributions to the macropinocytosis activation of SN21.

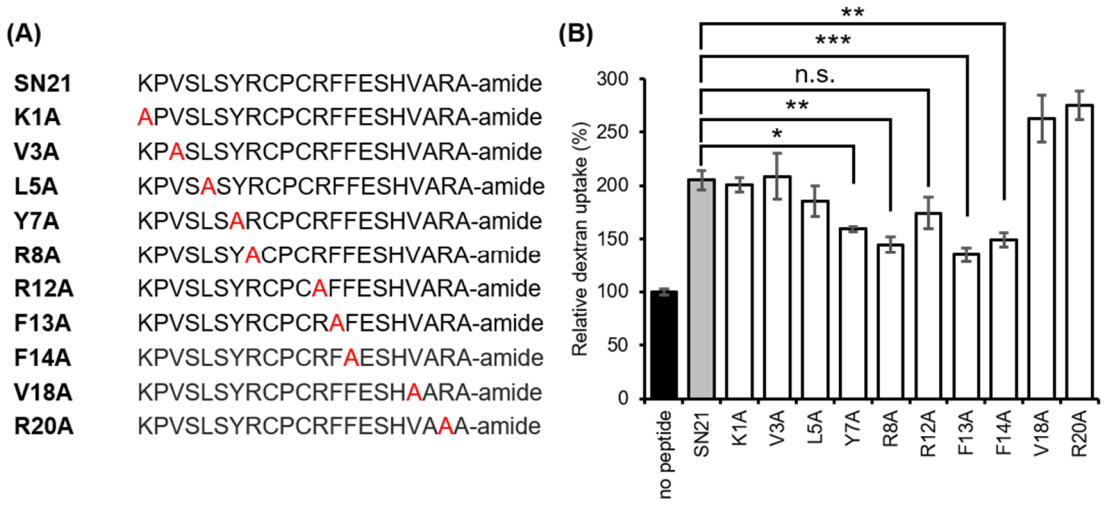

Figure 2–6. Alanine scanning of SN21 suggests important amino acid residues for the stimulation of dextran uptake. (A) Primary structures of alanine mutants of SN21. (B) Dextran uptake in HeLa cells treated with 5 μM peptide with 0.5 mg/mL Dex70-FL for 30 min. Data are presented as mean ± SE of three independent experiments (Student's *t*-test; ***, $P < 0.001$; **, $P < 0.01$; *, $P < 0.05$; n.s., not significant).

The data shown in Figure 2–6 suggests that the region between Tyr7 and Phe14, which includes Cys9 and Cys11, mainly contributes to the dextran uptake induced by SN21. As the minimization of the peptide region with critical residues will be helpful for the following analyses, sSN21, which encompasses residues from Tyr7 to Phe14, was then prepared (Fig. 2–7A). As proline residues often provide structural rigidity for the peptide structure, substitution of Pro10 between the two Cys residues by alanine/glycine was expected to increase the flexibility to the peptide. Thus, P4A and P4G mutants of sSN21 were also prepared, and, along with sSN21, were examined for induction of dextran uptake (Fig. 2–7B). Despite having the Tyr7 to Phe14 residues, sSN21 only yielded ~11% increased dextran uptake compared to no peptide control. Although this observed increase was statistically significant compared to no peptide treatment, this increase was statistically insignificant when compared to the dextran uptake induced by SN21 (~32%) (Fig. 2–7A). Among the analyzed peptides, P4A exhibited the highest dextran uptake induction (up to ~143% higher compared to no peptide control), which are significantly higher than induction by SN21 and sSN21. Thus, Pro-to-Ala/Gly mutations between the two Cys residues of the SN21-derived short peptide enhanced the dextran uptake induction. Since P4A showed the highest dextran uptake, the following experiments were performed using this peptide. Like SN21, macropinocytosis inhibitors (EIPA and wortmannin) decreased the dextran uptake induced by P4A, suggesting the involvement of macropinocytosis in P4A-mediated dextran uptake (Fig. 2–7C).

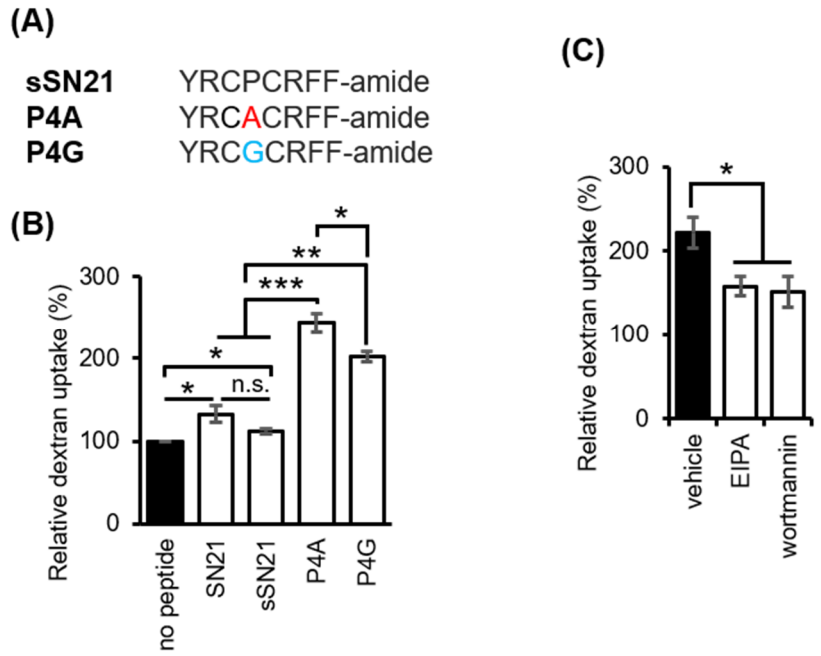

Figure 2–7. A minimal SN21-derived peptide shows features of intracellular delivery similar to SN21. (A) Primary structures of shorter versions of SN21. (B) Graph showing the induction of dextran uptake in HeLa cells treated with 5 μM peptides with 0.5 mg/mL Dex70-FL in α–MEM (–) for 30 min. (C) Macropinocytosis inhibitors (100 μM EIPA and 500 nM wortmannin) decreased P4A-induced dextran uptake. Data are presented as mean ± SE of three independent experiments (Student's *t*-test; ***, $P < 0.001$; **, $P < 0.01$; *, $P < 0.05$; n.s., not significant).

Cys-to-Ala mutants of P4A (P4A/C3A, P4A/C5A, P4A/C3A/C5A) and chemically modified P4A (alkyl-P4A and PyS-P4A) were synthesized (Fig. 2–8A). Similar to the Cys-to-Ala mutations of SN21 (Figure 2–4B), the Cys-to-Ala mutations of P4A decreased the induction of dextran uptake (Fig. 2–8B). Western blot analysis showed an increase in P-Akt and active Rac1 levels induced by P4A treatment (Fig. 2–8C). As for P4A/C3A/C5A mutants, however, no such marked increase was observed for P-Akt and active Rac1 levels. Alkylation of the thiols in P4A abolished the ability to induce dextran uptake, while modification of the Cys residues into activated disulfides slightly increased the dextran uptake of the P4A peptide (Fig. 2–8C). These data suggest a similarity between the activities and mechanisms of SN21 and P4A concerning the importance of their Cys residues for the activation of macropinocytic dextran uptake.

Lastly, P4A, but not P4A/C3A/C5A, showed marked activation of reorganization of the actin cytoskeleton (Fig. 2–8E), which is consistent with the low level of activated Rac1 in P4A/C3A/C5A-treated cells (Fig. 2–8C).

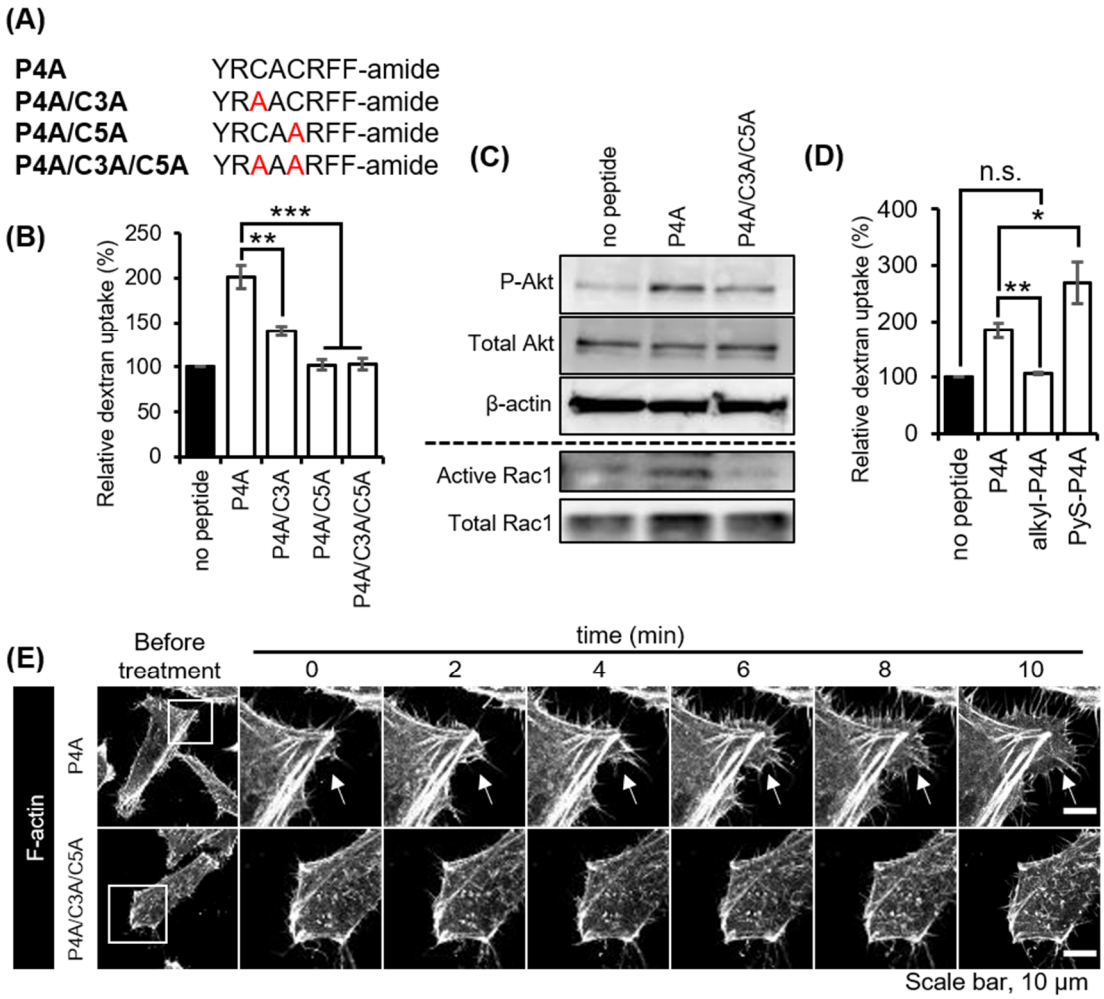

Figure 2–8. P4A requires Cys residues to achieve marked macropinocytosis induction. (A) Primary structures of Cys-to-Ala mutants of P4A and (B) their dextran uptake induction. (C) Western blot analysis of P-Akt and active Rac1 levels in cells treated with 5 μM peptide (representative data of n=3). (D) Dextran uptake induced by chemically modified P4A. Data are presented as mean ± SE of three independent experiments (Student's *t*-test; ***, $P < 0.001$; **, $P < 0.01$; *, $P < 0.05$; n.s., not significant). (E) Time-lapse imaging of reorganization of the actin cytoskeleton of lm-HeLa cells treated with 5 μM P4A or P4A/C3A/C5A. Images were captured using the FV3000 CLSM system.

IV. P4A undergoes thiol-disulfide exchange reactions with amino acids in the cell culture medium

Blocking and activating thiols on SN21 and P4A affected the dextran uptake induced by these peptides (Figs. 2–4B, 8D), suggesting that the reactivity of the Cys thiols on the peptides contributes to the observed macropinocytosis induced by these peptides. As the cell culture medium used in this study [i.e., α-MEM (−)] contained a high concentration of cysteine and cystine (0.5 and 0.1 mM, respectively), P4A may undergo thiol-disulfide exchange reaction with them. To address this possibility, P4A was added to α-MEM (−) in the original composition that contains amino acids [designated as α-MEM (AA+)] to final concentrations of 20 μM (150 μL). An aliquot of 50 μL was immediately analyzed by high performance liquid chromatography (HPLC) [This data is considered as 0 min incubation: green line, Fig. 2–9A], and unique peaks were collected and analyzed by matrix-assisted laser desorption/ionization mass spectrometry (MALDI-TOF MS). The remaining solution was incubated under standard cell culture conditions (37 °C, 5% CO_2) for 30 min, and the collected medium was analyzed by HPLC and MALDI-TOF MS [This data is then considered as 30 min incubation: blue line, Fig. 2–9A].

In addition to the P4A peak, unique peaks were observed immediately after adding P4A in α-MEM (AA+) [indicated by broken gray lines; Fig. 2–9A(i)]. MALDI-TOF analyses of these peaks yielded m/z of 1062.90, 1064.96, and 2123.73, which correspond to the intermolecularly oxidized P4A (oxP4A), P4A, and dimers of P4A (theoretical [$M+H^+$]; 1062.47, 1064.47, and 2123.93, respectively; structures of these peptides are given in Figure 2–9B). Intriguingly, after 30 min incubation, the amount of

P4A decreased, while the amounts of oxP4A and P4A dimers considerably increased. Given the potential involvement of amino acids in α-MEM (AA+) in the observed changes, and amino acid-free α-MEM (−) [designated as α-MEM (AA−)] was formulated (Table 2–1). When P4A was added to α-MEM (AA−), P4A remained mostly unchanged, with only a small fraction changed to oxP4A and dimeric P4A [Fig. 2–9A(ii)]. Even after 30 min incubation, the main species in the solution was P4A. These findings suggest the possible conversion of P4A upon administration to the cells.

Table 2–1. Formulation of amino acid-free α-MEM (AA−)

Reagent	MW	mg/L (1×)	mM (1×)
$CaCl_2$	110.98	200	1.80
KCl	74.55	400	5.37
$MgSO_4 \cdot 7\ H_2O$	246.48	199.6	0.81
NaCl	58.44	6800	116.36
$NaHCO_3$	84.01	2267.73	15.69
$Na_2HPO_4 \cdot 2\ H_2O$	156.01	157.57	1.01
Sodium ascorbate	198.11	50	0.25
D-glucose	180.16	1000	5.55
Sodium pyruvate	110.04	110	1.00

*Concentrations are based on MEMα (FUJIFILM Wako, Cat #135-15175)

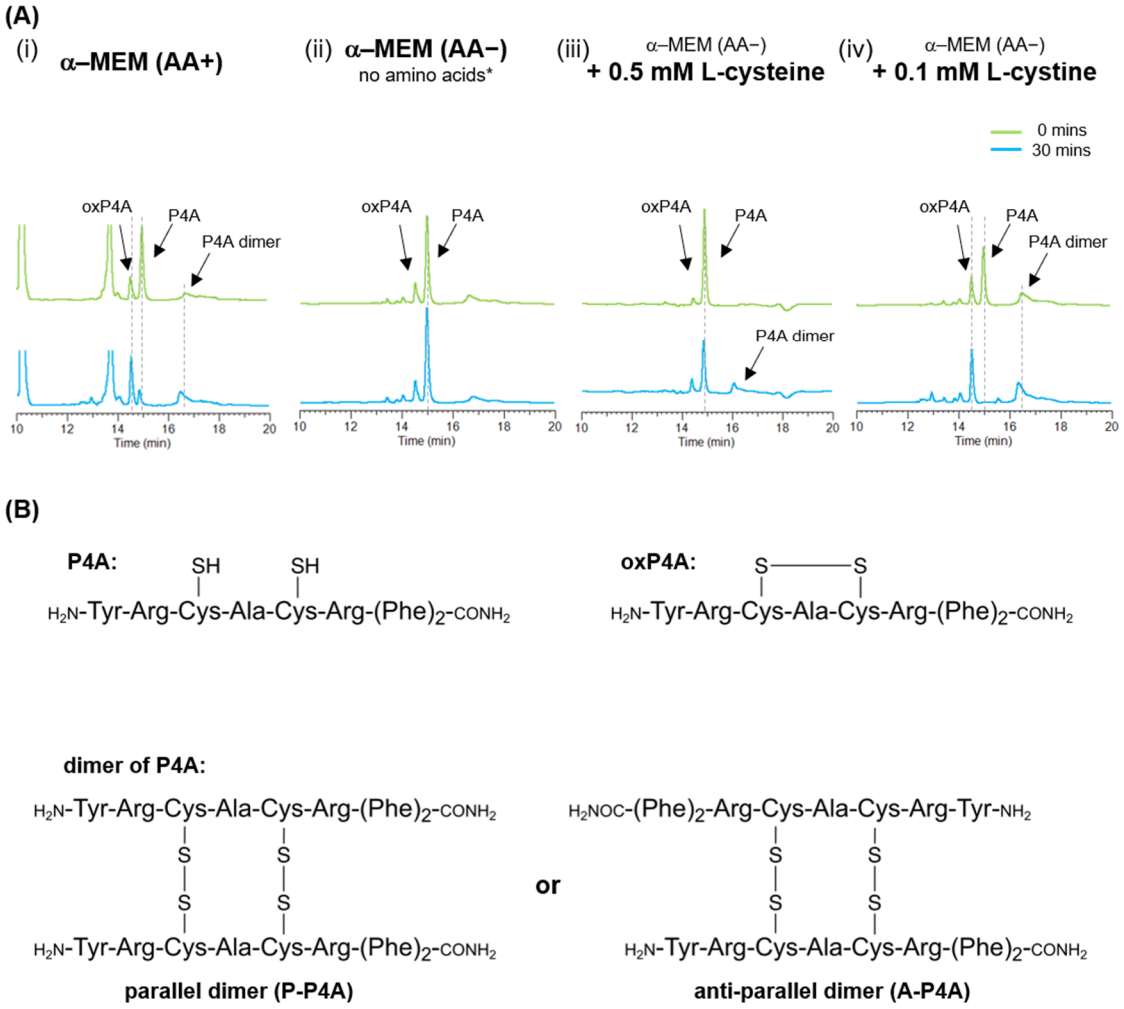

Figure 2–9. (A) HPLC analysis of 20 μM P4A in (i) regular amino acid-containing α-MEM [α-MEM (AA+)], (ii) amino acid-free α-MEM [α-MEM (AA−)], (iii) α-MEM (AA−) with 0.5 mM L-cysteine, or (iv) α-MEM (AA−) with 0.1 mM L-cystine (green line, 0 min incubation; blue line, 30 min incubation in 37 °C). Broken lines are to correlate the retention times of respective peptides. MALDI-TOF MS was conducted for the samples of (i) at 0 min, and the structures were deduced as in (B). Two possible forms of P4A dimer (parallel and anti-parallel) can be deduced from the MS values. HPLC peaks in succeeding runs having the corresponding retention times were speculated to have these structures.

It was possible that cysteine and cystine in the culture medium are involved in the observed changes of P4A. To address this possibility, changes of P4A were analyzed by supplementing cysteine or cystine into amino acid-free α-MEM (AA−). As shown in Fig. 2–9A(iii), oxP4A, and dimeric P4A were marginally increased when P4A was incubated for 0 or 30 min in α-MEM (AA−) supplemented with 0.5 mM L-cysteine (according to the formulation of MEMα from FUJIFILM Wako Pure Chemicals). In striking contrast, the addition of P4A to α-MEM (AA−) supplemented with 0.1 mM L-cystine resulted in the formation of oxP4A and dimeric P4A even upon the addition. Furthermore, the increase in the levels of oxP4A and P4A dimers after 30 min incubation was accompanied by the eventual loss of P4A [Fig. 2–9A(iv)]; this was essentially the same as observed when P4A was incubated in α-MEM (AA+) [Fig. 2–9A(i)]. The same incubations performed in the presence of HeLa cells suggested that P4A predominantly exists in its oxidized or dimeric forms when exposed to cystine-containing media (Fig. 2–10).

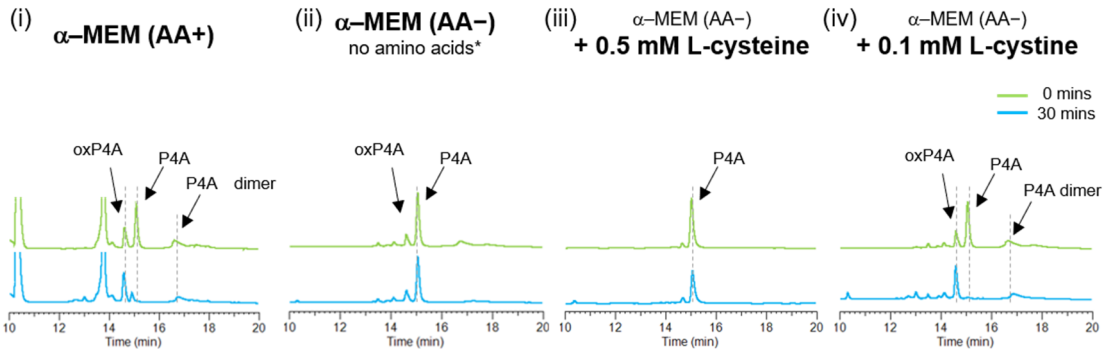

Figure 2–10. HPLC analysis of 20 μM P4A in α-MEM (AA+), amino acid-free α-MEM (AA−), α-MEM (AA−) with 0.5 mM L-cysteine, or α-MEM (AA−) with 0.1 mM L-cystine in the presence of serum-starved HeLa cells (green line, 0 min incubation; blue line, 30 min incubation in 37 °C).

V. Dextran uptake and macropinocytosis induced by oxidized form and dimers of P4A

The HPLC analyses data showed that P4A reacts with L-cystine in cell culture medium to form oxP4A and dimers of P4A independent of the presence of cells. Therefore, analyses of the abilities of oxP4A and dimeric P4A to induce the dextran uptake and macropinocytosis should provide more in-depth information about the mechanism of macropinocytosis induced by P4A.

To dissect the individual abilities of P4A, oxP4A, and dimeric P4A to induce macropinocytosis, these peptides were chemically synthesized. Oxidation of P4A was done by combining 0.1 mM P4A with 5 eq of methyl-3-nitropyridinesulfenate (NPys-OMe), followed by overnight incubation (Fig. 2–11).[90] The dimers of P4A can exist as a parallel dimer (P-P4A) and an anti-parallel dimer (A-P4A), both of which were synthesized. P-P4A synthesis starts with Fmoc-SPPS of P4A, having an acetamidomethyl (Acm)-protected Cys at position 5 (Cys5) (Fig. 2–12). After deprotection with trifluoroacetic acid (TFA)/H_2O (95:5) and purification yielded P4A 1. Half of the purified P4A 1 were reacted with 10 eq dithiodipyridine in 2 N acetic acid/isopropanol (10:3) solution to yield P4A 2 (yield: 86%).[91] P4A 1 and P4A 2 (1:1 mole ratio) in 0.1 M ammonium acetate (pH 6.5) was stirred for 1 h in ~23 °C, yielding P4A 4 having the disulfide bridge on Cys3 (yield: 89%). Finally, the Acm-protected Cys5 on P4A 4 (4 mmol) was deprotected using 40 eq silver trifluoromethanesulfonate (AgOTf), 35 eq anisole in 500 μM ice-cold TFA. The peptides were precipitated and washed with ice-cold diethyl ether. The dried peptide pellet was dissolved and incubated in a 50% dimethylsulfoxide (DMSO)/1 N HCl solution overnight at ~23 °C.[92] The supernatant was collected and diluted with H_2O (2-folds) before purification by

HPLC (yield: 38%). To synthesize A-P4A (Figure 2–13), P4A with Acm-protected Cys at position 3 (Cys3) was instead synthesized (P4A 3). This was combined with P4A 2 to yield P4A 5, having a disulfide bridge between Cys3 and Cys5 of P4A molecules (yield: 77%). Acm deprotection and final disulfide bridging were done as stated above, yielding A-P4A (yield: 32%). Retention times (R_t) of purified peptides are listed in Table 3–3 in Materials and Methods. Also, R_t of oxP4A and dimers of P4A corresponded well with the findings in Figure 2–9. Since P-P4A and A-P4A had similar R_t, under the standard protocol, additional analysis was performed by Ultra HPLC to evaluate their purities (Fig. 2–14).

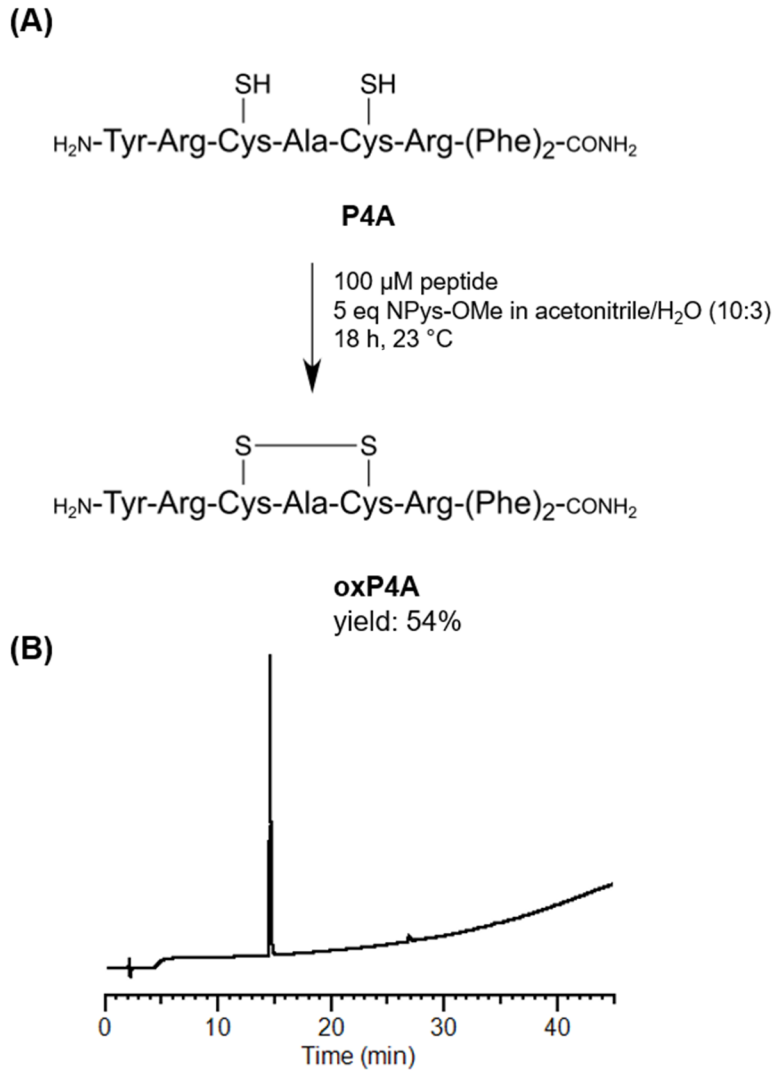

Figure 2–11. Synthesis of oxidized P4A (oxP4A). (A) Synthetic scheme. (B) Analytical HPLC of purified oxP4A.

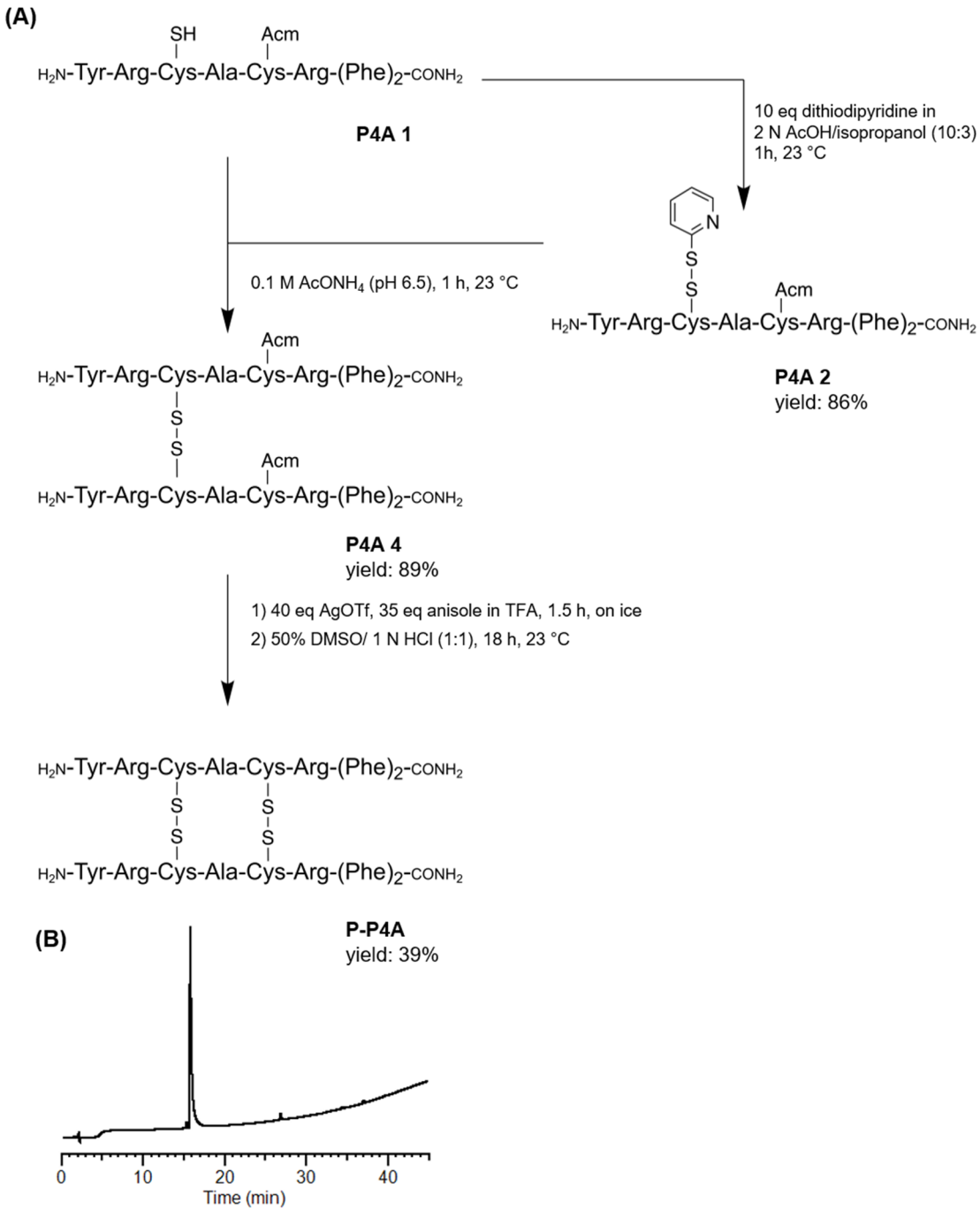

Figure 2–12. Synthesis of the parallel dimer of P4A (P-P4A). (A) Synthetic scheme. (B) Analytical HPLC of purified P-P4A.

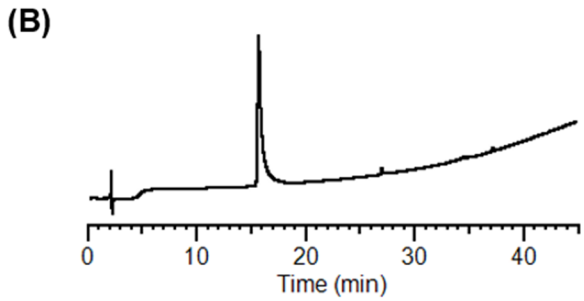

Figure 2–13. Synthesis of the anti-parallel dimer of P4A (A-P4A). (A) Synthetic scheme. (B) Analytical HPLC of purified A-P4A.

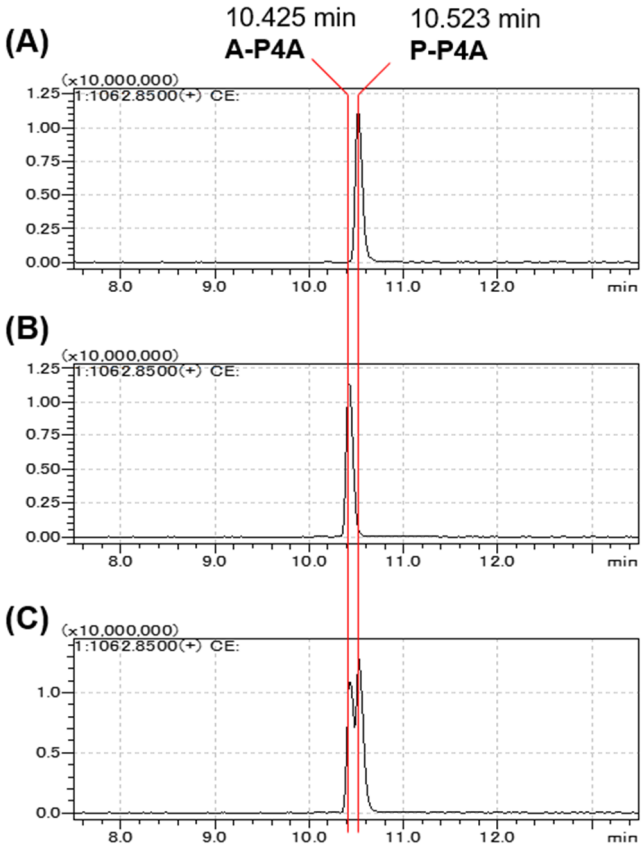

Figure 2–14. Ultra HPLC analysis of (A) P-P4A, (B) A-P4A. and (C) a mixture of both peptides [column: C18-AQ (3 µm, 150 × 2.1 mm, Shimadzu); system: Nexera UHPLC system; A = H_2O-0.1% formic acid, B = acetonitrile-0.1% formic acid; gradient: 0-3 min, 0% B; 3-15 min, linear gradient to 60% B; 15-17.5 min, 95%B; 17.5-20.0 min, linear gradient to 0% B; hold for 4 min; flow rate, 0.2 ml/min; temp = 40 °C].

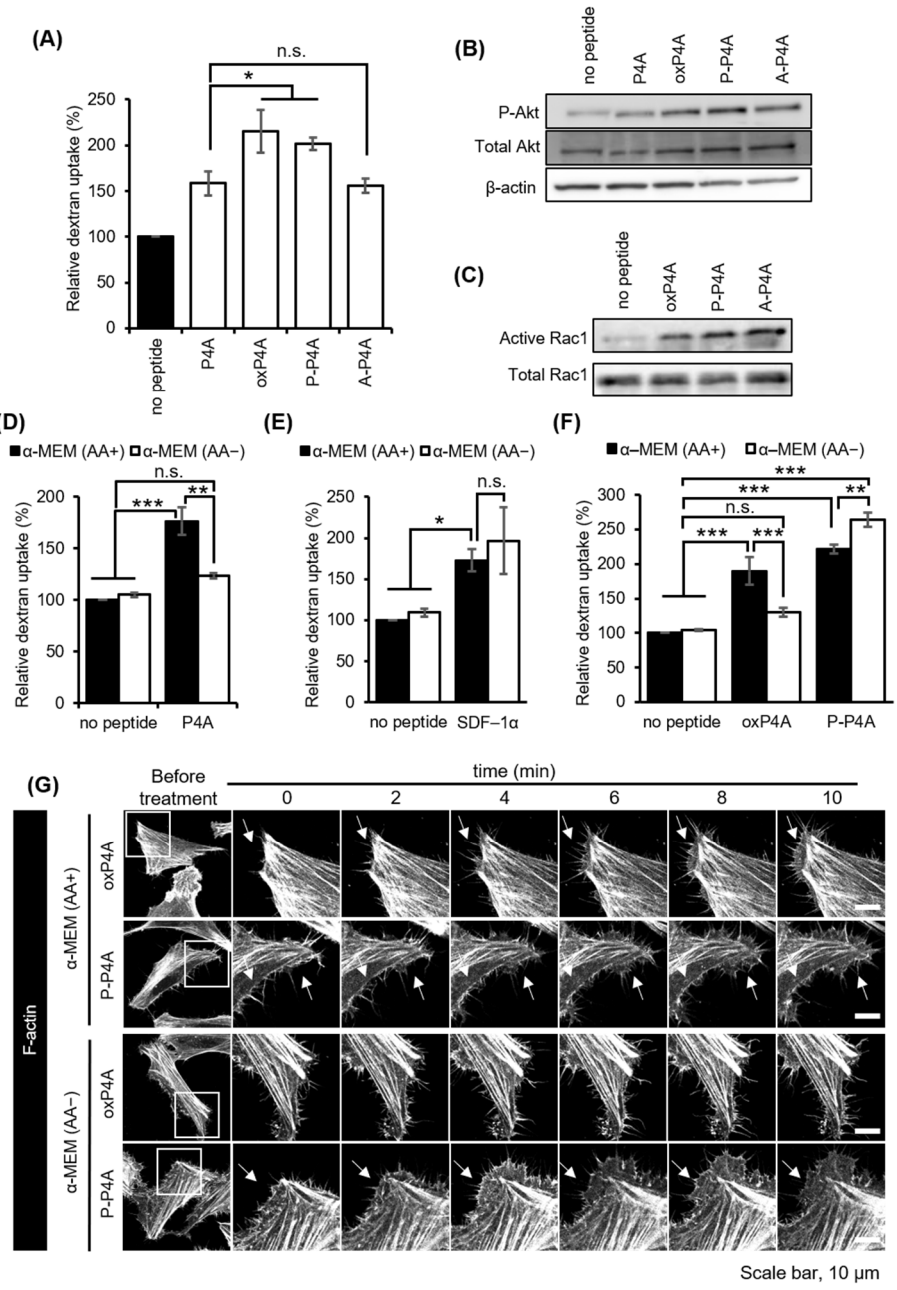

Figure 2–15. Oxidized and parallel dimer forms of P4A have the highest ability to induce macropinocytosis. (A) Dextran uptake in HeLa cells treated with 5 μM P4A, 5 μM oxP4A, 2.5 μM P-P4A or 2.5 μM A-P4A and 0.5 mg/mL Dex70-TMR in α-MEM (−) for 30 min. Western blot analysis of (B) P-Akt and (C) active Rac1 levels in peptide-treated HeLa cells (representative data of n=3). Dextran uptake induced by (D) P4A, (E) SDF-1α, (F) oxP4A, and P-P4A in α-MEM (AA+) or α-MEM (AA−). Data are presented as mean ± SE of three independent experiments (Student's *t*-test; ***, $P < 0.001$; **, $P < 0.01$; *, $P < 0.05$; n.s., not significant) (G) Time-lapse microscopy of lm-HeLa cells treated with 5 μM oxP4A or 2.5 μM P-P4A in α-MEM (AA+) or α-MEM (AA−). Arrows indicate areas of lamellipodia formation. Images were captured using the FV3000 CLSM system.

Dextran uptake induction of these peptides was evaluated along with their activation of macropinocytosis signaling. Incubation of cells with 5 μM P4A, 5 μM oxP4A, 2.5 μM P-P4A, or 2.5 μM A-P4A in the presence of 0.5 mg/mL Dex70-TMR showed that all the peptides were capable of increasing dextran uptake (Fig. 2–15A). Compared to no peptide control, oxP4A and P-P4A approximately doubled the dextran uptake and P4A and A-P4A increased the uptake by ~1.5-fold. Western blot analysis showed that P-Akt and active Rac1 levels were substantially increased by the P4A and modified P4A peptides (Fig. 2–15B, C). Then, dextran uptake and reorganization of the actin cytoskeleton induced by the P4A-derived peptides were compared in the presence and absence of amino acids in the medium. P4A-induced dextran uptake was significantly lower in α-MEM (AA−) than in α-MEM (AA+) (Fig. 2–15D). Given that P4A remains in its reduced form when added to α-MEM (AA−) (Fig. 2–9, 2–10), and that no significant increase in dextran uptake was induced by P4A in α-MEM (AA−) (Fig. 2-15D), it is likely that the conversion of P4A to the oxP4A and dimeric forms is crucial for P4A to induce dextran uptake. On the other hand, SDF-1α, which activates macropinocytosis via its binding to CXCR4, induced the dextran uptake independent of amino acids in the medium (Fig. 2–15E). Dextran uptake induced by oxP4A in the absence of amino acids in the medium was not significantly different from no peptide treatment conditions, whereas P-P4A significantly increased the dextran uptake in both the presence and absence of extracellular amino acids (Fig. 2–15F). In parallel with the dextran uptake induction, oxP4A induced reorganization of the actin cytoskeleton in the presence but not the absence of extracellular amino acids (Fig. 2–15G), whereas P-P4A induced the cytoskeletal reorganization even under the α-MEM (AA−) conditions (Fig.

2–15G). The above results suggested that the disulfide exchange performed by P4A and oxP4A in α-MEM (AA+) leads to the conversion to mixed forms of P4A, including oxP4A and the dimers of P4A, among which P-P4A is likely to be the most potent macropinocytosis inducer.

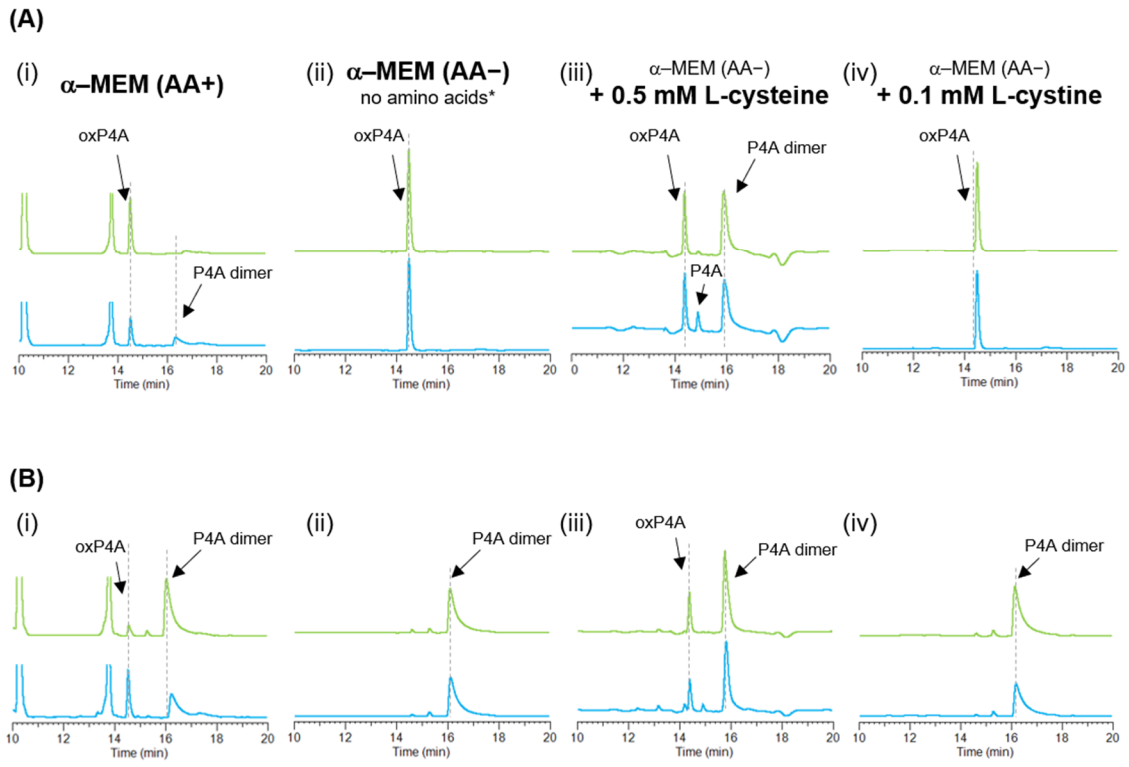

Figure 2–16. HPLC analysis of (A) oxP4A and (B) P-P4A incubated in α-MEM (AA+), α-MEM (AA−), α-MEM (AA−) with 0.5 mM L-cysteine, or α-MEM (AA−) with 0.1 mM L-cystine for 0 min (green line) and after 30 min in 37 °C (blue line).

HPLC analysis was also performed on oxP4A and P-P4A when incubated in α-MEM (AA+), α-MEM (AA−), α-MEM (AA−) with 0.5 mM L-cysteine, or α-MEM (AA−) with 0.1 mM L-cystine (Fig. 2–16). Incubation of oxP4A and P-P4A in α-MEM (AA+) for 30 min resulted in the mixed solution containing both oxidized and dimeric forms [Fig. 2–16A, B(i)], whereas incubation of these peptides in α-MEM (AA−) did not cause their substantial transformation [Fig. 2–16A, B(ii)]. When oxP4A and P-P4A

were incubated in α-MEM (AA−) with 0.5 mM L-cysteine, both the oxidized and dimeric forms were found in the medium [Fig. 2–16A, B(iii)], suggesting the interconversion of these peptides in the presence of L-cysteine; this was in contrast to incubation of P4A in α-MEM (AA−) with 0.5 mM L-cysteine, where P4A remained unchanged (Figs. 2–9, 2–10). Incubation of oxP4A and P-P4A in α-MEM (AA−) with 0.1 mM L-cystine did not cause the transformation of these peptides [Fig. 2–16A, B(iv)]; this was also in contrast to the incubation of P4A under the same conditions, where both the oxidized and dimeric P4A forms were generated (Figure 2–9). These data provide information regarding the transformation of P4A occurring within the medium. Namely, interconversion of oxP4A and dimeric P4A might be stimulated in the presence of free cysteine, whereas P4A was changed, in the presence of L-cystine, to oxP4A and dimeric P4A, which are likely to be energetically more stable.

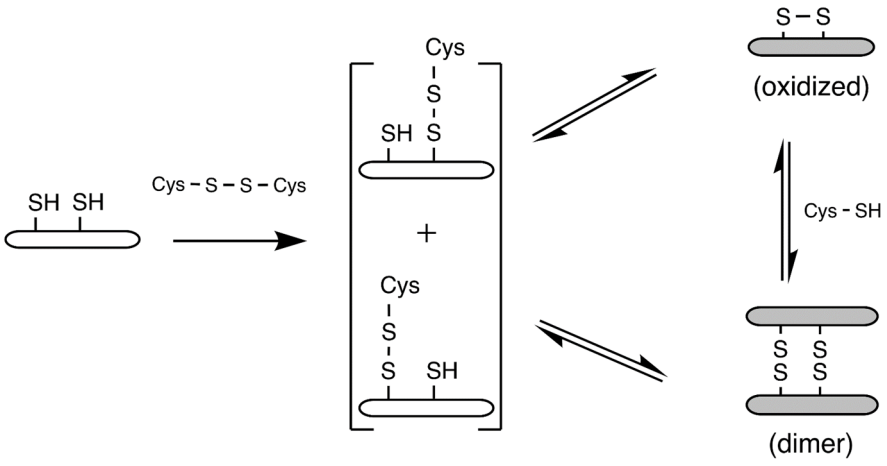

Scheme 2–1. Proposed extracellular thiol-disulfide exchange reactions performed by reduced P4A. (1) Cystine in the medium first reacts with reduced P4A and forms mixed disulfides of P4A, which can either (2) perform self-oxidation to form oxP4A, or (3) react with another mixed disulfide to form P4A dimers. In the presence of L-cysteine, oxP4A and P4A dimers coexist, possibly in equilibrium.

HPLC analyses of P4A, oxP4A, and P4A incubated in the presence of L-cysteine and L-cystine suggest dynamic thiol-disulfide exchange reactions shown in Scheme 2–1; first, P4A reacts with cystine in the medium to form mixed disulfides. Cys3 and Cys5 on P4A have adjacent, positively charged Arg residues (Arg2 and Arg6), which may decrease the pK_a of adjacent Cys residues on the peptide, enabling thiolate formation at neutral pH.[93,94] These thiolates can react with oxidizing agents (i.e., cystine) to form mixed disulfides, which can exchange with either a second thiol within the same molecule (intramolecular) to form oxP4A or with another P4A molecule (intermolecular) to form dimeric P4A. Gauthier and coworkers suggested the propensity of CXC-bearing peptides to form intermolecular thiol-disulfide bridges.[93,94] HPLC analyses of oxP4A and P-P4A incubated in α–MEM (AA−) with 0.5 mM L-cysteine suggests that cysteine is responsible for driving the reversible conversion between oxP4A and the dimers (Fig. 2–14B).

Discussion

Herein, the mechanisms underlying macropinocytosis induced by newly identified SN21-derived peptides were studied. Although SN21 is derived from the receptor binding and activating motifs of a CXCR4 ligand, it weakly interacts with CXCR4, which may not be enough to activate CXCR4. Despite the lack of substantial interaction of SN21 with CXCR4 in the NanoBRET competition assay (Fig. 2–2), SN21 retains the ability to induce macropinocytosis (Fig. 2–3), suggesting a macropinocytosis-inducing mechanism independent of CXCR4. Analyses of the structure-activity relationship revealed that Cys9 and Cys11 of SN21 are critical for the observed macropinocytosis induction, and Tyr7, Arg8, Phe13, and Phe14 also make some contribution. In agreement with the alanine scanning results, a short peptide of SN21 encompassing Tyr7 to Phe14 (sSN21) and its derivatives (P4A, and P4G) also induced macropinocytosis. Like SN21, Cys-to-Ala mutations on P4A abolished the activity, emphasizing the critical role of these Cys residues in macropinocytosis induction.

Aubry et al. reported the contribution of Cys residues to cellular uptake of peptides.[95] On the other hand, Wu and coworkers found that the addition of a Cys-Xxx-Cys (CXC) motif to non-cell penetrating peptides enabled their entry into cells via an energy-dependent uptake pathway, which was reported to be insensitive to common endocytosis or macropinocytosis inhibitors.[96,97] Both groups suggested that thiol-disulfide exchange reactions between the peptides and cell-surface thiols were responsible for the observed internalization into cells. Besides these studies, the detailed cellular entry mechanisms of cysteine-bearing peptides have been poorly understood.

The critical finding in this chapter is the importance of cysteine and cystine in the medium to the macropinocytosis induction by P4A. The presence of these amino acids in the medium was found to facilitate the thiol-disulfide exchange reactions of P4A, transforming P4A into its oxidized and dimeric forms (Figs. 2–9, 2–10, and 2–16). In an amino acid-free medium, P4A remained unchanged (reduced state), without its conversion to the oxidized and dimeric forms (Fig. 2–9A). Intriguingly, under the same conditions, the ability of P4A to induce dextran uptake was not apparent, compared to the amino acid-containing conditions (Fig. 2–15D). By contrast, SDF-1α can induce dextran uptake independent of extracellular amino acids (Fig. 2–15E), because it induces macropinocytosis via its binding to CXCR4. Therefore, the dextran uptake induction observed in the presence of P4A was attributable to either oxP4A or dimers of P4A generated by the disulfide exchange reactions. Note that the dextran uptake induction by oxP4A was not apparent in α-MEM (AA–), whereas the parallel dimer of P4A exhibited its ability to induce dextran uptake independent of extracellular amino acids (Fig. 2–15F). These results suggest that, among the P4A-derived peptides, the dimers of P4A, particularly P-P4A, should play a substantive role in inducing dextran uptake and macropinocytosis. As described above, it has been considered that cross-link formation with cell-surface thiols should lead to the cell-surface recruitment and enhanced cellular uptake of Cys-containing peptides.[95,96] The present study, however, raised the alternative possibility that cysteine and cystine in the medium contribute to the conversion of the P4A peptide to its active forms.

A recent study by Wei et al. showed that the lack of cysteine in the medium suppressed the macropinocytic uptake of nanoparticles, suggesting the potential

contribution of cysteine within the medium to activate macropinocytosis.[98] However, the most typical and well-known pathway to induce macropinocytosis is via stimulation of growth factor receptors by their ligands; however, the stimulation by the ligands does not require extracellular amino acids.[31,99] Consistently, the present study showed that SDF-1α was observed to induce dextran uptake even in an amino acid-free medium (Fig. 2–15E). Notably, P-P4A was capable of increasing dextran uptake and activating reorganization of the actin cytoskeleton under amino acid-free conditions (Fig. 2–15F, G). Given the similarity to macropinocytosis stimulated by growth factors, such as SDF-1α, it could be hypothesized that P-P4A may interact with certain cell-surface receptors to activate macropinocytosis. Further investigations regarding the identification of the putative receptor will help to understand how P-P4A induces macropinocytosis.

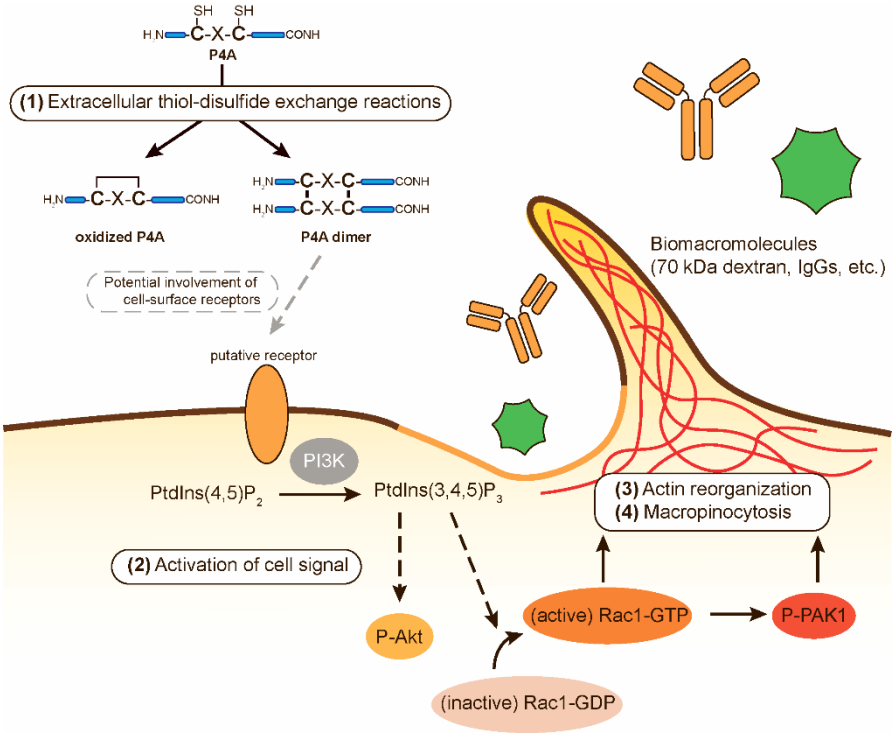

Figure 2–17. Possible mechanism for macropinocytosis induction by P4A. (1) P4A undergoes thiol-disulfide exchange with cysteine and cystine in the medium to form oxP4A and the dimeric P4A, among which P-P4A was assumed to be the most potent macropinocytosis inducer. It is possible that P-P4A interacts with cell-surface receptors to (2) activate cell signaling pathways, leading to (3) reorganization of the actin cytoskeleton and (4) macropinocytosis.

As proposed in Figure 2–17, cysteine-bearing peptide P4A (1) undergoes thiol-disulfide exchange reactions in the culture medium, and transformation into oxP4A and the dimeric forms, among which the parallel dimer showed the highest potency. These forms could interact with unidentified cell-surface receptors to (2) activate signaling pathways, leading to (3) reorganization of the actin cytoskeleton and (4) macropinocytosis. Although more detailed studies are required, this chapter provides an insight into the mechanisms underlying macropinocytosis induced by a cysteine-bearing peptide P4A and its derivatives. In particular, the contribution of the extracellular environment to their structures and activity of the peptides is emphasized.

Conclusion

This dissertation aimed to establish the basis of the peptide-mediated activation of macropinocytosis as a potential route for the intracellular delivery of biomacromolecules and to elucidate the mechanisms underlying the delivery.

In Chapter 1, SN21 derived from SDF-1α was identified as a novel macropinocytosis-inducing peptide. Although the SN21 peptide demonstrates a high level of competence to induce dextran uptake compared to known macropinocytosis inducers, there remained a problem related to the delivery of cargo macromolecules to the cytosol across endosomal membranes. However, the fusion of SN21 with LK15 (a membrane-lytic peptide) was found to overcome the problem of intracellular delivery. Moreover, SN21–LK15 was able to deliver cargo macromolecules with different physicochemical properties, demonstrating this fusion peptide as an attractive tool for macromolecule delivery. Since various peptides have been developed to enhance endosomal escape (e.g., pH-responsive[9] and lipid charge-responsive peptides[47]), the substitution of LK15 with other peptides with higher endosomal escape ability may further improve the strategy.

Findings in Chapter 2 expounded on the potential mechanism underlying macropinocytosis induced by SN21 and P4A. NanoBRET-based receptor binding, pharmacological inhibition, and knockdown analyses altogether showed that SN21 displays a marginal interaction with CXCR4. Instead, the activity of SN21 to induce macropinocytosis relied on 8-amino acid residues, including the two Cys residues of the canonical CXC motif. Mutations of one or both of the Cys residues abolished the

macropinocytosis-inducing activity. This was also true for the short P4A peptide encompassing the crucial 8-amino acid residues from SN21. Importantly, P4A undergoes thiol-disulfide exchange reactions with cystine in the cell culture medium to generate the oxP4A and dimeric forms, among which the latter may play substantive roles in inducing macropinocytosis

Overall, this dissertation presents findings on the macropinocytosis induction by SN21-derived peptides. The strategy using these peptides was highly effective for the intracellular delivery of nucleic acid and protein when combined with the endosome perturbation strategy using membrane lytic peptides. Moreover, the role of extracellular cysteine and cystine to allow thiol-disulfide exchange reaction of the cysteine-bearing macropinocytosis-inducing peptide P4A could be a new finding in the effects of the extracellular environment on peptide-mediated biosignaling and intracellular delivery.

Materials and Methods

Materials

All chemicals, materials, and cell culture media were purchased for either Thermo Scientific or FUJIFILM Wako Pure Chemicals unless otherwise specified. All synthesized oligonucleotides were purchased from Thermo Scientific and are listed in Table 3–1. Antibodies used in this work are summarized in Table 3–2.

Table 3–1. List of primers

Oligo Name	Sequence (5′- 3′)
EF1 promoter- forward	GGT AAA ATC GAT AAG CCG CGT ACG CGT GTG AAG ACT C
EF1 promoter- reverse	TCG CCA CCA TGA CCG AGT ACA AGC CCA CGG
EF1 insulator- forward	CGG TCA TGG TGG CGA ATT CGT AGG CGC C
EF1 insulator- reverse	GGG CAT CGG TCG ACG CGA CGG CCA GTG AAA CTA GTG GT

Table 3–2. List of Antibodies for Western Blot

Antibody (source)	Maker	Cat. #	Dilution
Anti-KRAS antibody (Rabbit)	Abcam	ab180772	1:1000
Monoclonal anti-actin antibody (Mouse)	Sigma-Aldrich	A2228	1:10,000
Phospho-Akt (Ser473) (D9E) XP mAb (Rabbit)	Cell Signaling Technology	4060	1:2000
Akt Antibody (Rabbit)	Cell Signaling Technology	9272	1:1000
Anti-Rac1 Antibody, clone 23A8 (Mouse)	Merck	05-389	1:1000
Anti-Mouse IgG, Horseradish Peroxidase-Linked	GE Healthcare	NA931	1:5000
Anti-rabbit IgG, HRP-linked Antibody	Cell Signaling Technology	7074	1:2000

Peptide Synthesis

General procedure for peptide synthesis

All linear peptides were synthesized via Fmoc solid-phase peptide synthesis (SPPS) using a Rink amide resin (TGS-RAM) and the 3-[bis(dimethylamino)methyliumyl]-3*H*-benzotriazol-1-oxide hexafluorophosphate (HBTU)/hydroxybenzotriazole (HOBt) coupling system. Deprotection of protecting groups and detachment of the peptides from the resin was conducted using trifluoroacetic acid (TFA)/ethanedithiol (95:5) at room temperature (~23°C) for 3 h. Peptides were purified by reverse-phase high-performance liquid chromatography (HPLC) using a C18 column. Masses were confirmed by MALDI-TOF mass spectroscopy. Peptide sequences, obtained masses and analytical HPLC retention times (R_t) [column: Cosmosil 5C18-AR-II (4.6 × 150 mm) (Nacalai Tesque); gradient: 5−95% B in A (A = H_2O containing 0.1% TFA, B = CH_3CN containing 0.1% TFA) over 45 min; flow: 1 mL/min; detection: 220 nm] are summarized in Table 3–3.

Fluorescein isothiocyanate (FITC) conjugation

The protected peptide segment of SN21, Lys(Boc)-Pro-Val-Ser(^{t}Bu)-Leu-Ser(^{t}Bu)-Tyr(^{t}Bu)-Arg(Pbf)-Cys(Trt)-Pro-Cys(Trt)-Phe-Phe-Glu(O^{t}Bu)-Ser(^{t}Bu)-His(Trt)-Val-Ala-Arg(Pbf)-Ala-Gly-Lys(Mtt)-NH-resin (Boc = *tert*-butyloxycarbonyl; ^{t}Bu = *tert*-butyl; Pbf = 2,2,4,6,7-pentamethyldihydrobenzofuran-5-sulfonyl; Trt = trityl; Mtt = 4-methyltrityl) was constructed as stated above. N-terminal Boc protection was done by incubating the resin with di-*tert*-butyl dicarbonate (Boc_2O, 5 eq) and *N*-methylmorpholine (NMM, 5 eq) in dimethylformamide (DMF) for 3 h at 23°C. The resin was washed with DMF, methanol (MeOH), and diethylether (DEE) for five times

each and was dried in vacuo at ~23°C. The protected peptide resin was then allowed to swell in dichloromethane (DCM) for 30 min at ~23°C. Mtt deprotection was performed in 1,1,1,3,3,3-hexafluoro-2-propanol (HFIP)/DCM (1:4) solution for 3 h at 23°C. The peptide resin was then washed with DCM, DMF, MeOH, and DEE for 3× each and dried. Fluorescein isothiocyanate (FITC) labeling was done by treating the peptide resin in the presence of FITC (3 eq) and diisopropylethylamine (DIEA, 10 eq) in pyridine/DMF/DCM (12:7:5) with constant shaking overnight. The final deprotection of the protecting groups and cleavage from the resin, purification, and subsequent analyses were performed as stated above. Obtained masses and analytical HPLC retention times (R_t) are listed in Table 3–3.

Synthesis of alkylated peptides

Purified peptides (1 μmol) were dissolved in 100 μL phosphate-buffered saline (PBS: 100 mM Na_2HPO_4, 18 mM KH_2PO_4, 1.37 M NaCl, 27 mM KCl, pH 7.2) with 2.5 mM dithiolthreitol (DTT). Iodoacetamide (10 eq in H_2O) was added, and the solution was incubated in dark for 1 h at room temperature (~23 °C) with stirring. Alkylated peptides were purified by HPLC and analyzed by MALDI-TOF MS. Obtained masses and analytical HPLC retention times (R_t) are listed in Table 3–3.

Synthesis of pyridinesulfenylated (PyS) peptides

Purified peptides (2 μmol) were dissolved in 2N acetic acid (AcOH). 2,2'-Dithiolpyridine (10 eq) in 2-propanol was added to yield a 2N AcOH/2-propanol ratio (10:3, total volume of 0.4 mL). The solution was incubated for 1 h at room temperature

(~23 °C) with stirring, followed by purification by HPLC and analysis by MALDI-TOF MS. Obtained masses and analytical HPLC retention times (R_t) are listed in Table 3–3.

Synthesis of oxP4A

Purified P4A was dissolved in H_2O. To this, 5 eq of methyl 3-nitro-2-pyridinesulfenate (NPyS-OMe) in acetonitrile was added (0.1 mM final peptide concentration). The solution was allowed to react overnight at room temperature (~23 °C) with constant stirring. Purification was performed by HPLC and analysis by MALDI-TOF MS. Obtained masses and analytical HPLC retention times (R_t) are listed in Table 3–3.

Synthesis of P-P4A and A-P4A

Protected peptides for P4A 1 [Tyr(^{t}Bu)-Arg(Pbf)-Cys(Trt)-Pro-Cys(Acm)-Phe-Phe-NH-resin] and for P4A 3 [Tyr(^{t}Bu)-Arg(Pbf)-Cys(Acm)-Pro-Cys(Trt)-Phe-Phe-NH-resin] (Acm= acetamidomethyl) were synthesized, deprotected, and purified as stated above to yield P4A 1 and P4A 3. P4A 2 was synthesized by pyridinesulfenylation of P4A-1 using the protocol above.

P4A 4 was synthesized by combining equal molar ratios of P4A 1 and P4A 2 in 0.1M ammonium acetate (pH 6.5, 1 mL). The solution was stirred for 30 min at room temperature (~23 °C), or until the reaction completes. For anti-parallel dimer, P4A 5 was synthesized by combining P4A 2 and P4A 3 in a similar manner to above. Purification by HPLC and MALDI-TOF MS analysis were followed.

Parallel P4A (P-P4A) and anti-parallel P4A (A-P4A) were synthesized from P4A 4 (3.8 μmol) and P4A 5 (1.3 μmol), respectively. The peptides were dissolved in a

500 µL of pre-chilled TFA containing 40 eq silver trimethanesulfonate (AgOTf) and 10 µL anisole. The mixture was incubated on ice for 1.5 h. Washing was performed by adding ice-cold dry diethyl ether (1 mL) to the solution, followed by centrifugation (3,500 × g, 5 min). The supernatant was discarded, and the washing step was repeated twice before drying the precipitate *in vacuo*. The dried pellet was dissolved in 4 mL 50% DMSO/1 M HCl and incubated overnight (18 h) at room temperature (~23 °C) with constant agitation. The solution was centrifuged (3,500 × g, 5 min), and the supernatant was collected. Purification was performed by HPLC like above. MALDI-TOF MS analyzed the molecular weights of the obtained peptides.

Table 3–3. List of synthesized peptides

Peptide	Sequence	$[M+H^+]_{calc.}$	$[M+H^+]_{obs.}$	R_t
SN8	KPVSLSYR-amide	948.56	948.47	11.2
SN17	KPVSLSYRCPCRFFESH-amide	2054.99	2055.27	17.6
SN21	KPVSLSYRCPCRFFESHVARA-amide	2451.24	2450.75	15.1
SN23	KPVSLSYRAPCRFFESHVARANV-amide	2665.34	2665.52	15.3
SN25	KPVSLSYRCPARFFESHVARANVKH-amide	2930.50	2930.89	14.8
SN21-FITC	KPVSLSYRCPCRFFESHVARAK(FITC)-amide	2969.37	2968.04	22.2
LK15	KLLKLLLKLLLKLLK-amide	1789.33	1789.69	28.0
Tat-LK15	GRKKRRQRRRPGGKLLKLLLKLLLKLLK-amide	3378.30	3378.24	23.9
dSN21	kpvslsyrcpcrffeshvara-amide	2054.99	2055.27	17.6
K1A	APVSLSYRCPCRFFESHVARA-amide	2395.17	2395.64	15.6
V3A	KPASLSYRCPCRFFESHVARA-amide	2424.20	2423.78	14.6
L5A	KPVSASYRCPCRFFESHVARA-amide	2410.18	2409.73	14.6
Y7A	KPVSLSARCPCRFFESHVARA-amide	2360.20	2360.63	14.8
R8A	KPVSLSYACPCRFFESHVARA-amide	2367.17	2367.36	16.2
C9A	KPVSLSYRAPCRFFESHVARA-amide	2420.25	2419.55	14.8
C11A	KPVSLSYRCPARFFESHVARA-amide	2420.25	2419.47	14.9

R12A	KPVSLSYRCPCAFFESHVARA-amide	2367.17	2367.56	16.1
F13A	KPVSLSYRCPCRAFESHVARA-amide	2376.30	2376.74	13.6
F14A	KPVSLSYRCPCRFAESHVARA-amide	2376.30	2376.55	13.4
V18A	KPVSLSYRCPCRFFESHAARA-amide	2424.20	2423.74	15.0
R20A	KPVSLSYRCPCRFFESHVAAA-amide	2367.17	2368.03	15.3
C9A/C11A	KPVSLSYRAPARFFESHVARA-amide	2387.29	2388.01	14.5
sSN21	YRCPCRFF-amide	2387.29	2388.01	12.1
P4A	YRCACRFF-amide	1090.49	1090.66	14.7
P4G	YRCGCRFF-amide	1050.46	1050.36	15.3
P4A-LK15	YRCACRFFGGKLLKLLLKLLLKLLK-amide	2949.83	2949.15	28.5
P4A/C3A	YRAACRFF-amide	1032.50	1032.64	14.6
P4A/C5A	YRCAARFF-amide	1032.50	1032.62	14.4
P4A/C3A/C5A	YRAAARFF-amide	1000.53	1000.67	13.9
alkyl-SN21	KPVSLSYRC(alkyl)PC(alkyl)RFFESHVARA-amide	2566.28	2566.62	14.0
PyS-SN21	KPVSLSYRC(PyS)PC(PyS)RFFESHVARA-amide	2670.24	2670.32	16.6
alkyl-P4A	YRC(alkyl)AC(alkyl)RFF-amide	1178.52	1178.64	13.7
PyS-P4A	YRC(PyS)AC(PyS)RFF-amide	1282.59	1282.09	17.6
oxP4A	YRC*AC*RFF-amide	1062.47	1062.63	14.6
P4A 1	YRCAC(Acm)RFF-amide	1135.37	1135.64	14.3
P4A 2	YRC(PyS)AC(Acm)RFF-amide	1244.51	1244.75	15.6
P4A 3	YRC(Acm)ACRFF-amide	1135.37	1135.65	14.4
P4A 4	See Figure 2–12	2268.72	2268.27	15.7
P4A 5	See Figure 2–13	2268.72	2267.73	15.7
P-P4A	See Figure 2–12	2124.54	2124.07	15.8
A-P4A	See Figure 2–13	2124.54	2124.30	15.7

(alkyl = alkylated by iodoacetamide; PyS = pyridinefulfenylated; Acm = acetamidomethyl; * = disulfide bridged)

Chapter 1 Cell Assay Experimental Procedures

Cell Culture

All incubations were done at 37°C in a humidified 5% CO_2 atmosphere. HeLa cells were cultured in minimum essential medium alpha modification (FUJIFILM Wako) containing 10% bovine serum (BS) (Gibco) [α-MEM (+)]. Established HeLa cells stably expressing GL3 luciferase (HeLa-GL3) cells[66] and HeLa-TBS-Luci cells were cultured in α-MEM (+) with 500 μg/mL G418 and 0.8 μg/mL puromycin, respectively.

Dextran Uptake Assays

HeLa cells (6×10^4 cells/well) were seeded onto 24-well plates (IWAKI) and incubated overnight for their attachment to the plates, followed by serum-starvation with serum-free α-MEM [α-MEM (−)] for 16 h. Starved cells were washed three times with PBS and treated with 1 mg/mL 70 kDa fluorescein-dextran (Dex70-FL) with 5 μM peptides or indicated proteins in α-MEM (−) (total volume of 200 μL) for 30 min. After incubation, cells were washed three times with ice-cold PBS, dislodged with 0.01% trypsin for 5 min, and transferred to microcentrifuge tubes. Samples were centrifuged (800 × *g*, 5 min, 4°C), and the pellets were washed once with PBS. Flow cytometry (FCM) analysis was performed on 10,000 gated events using Attune NxT Flow Cytometer (Thermo Fisher). Data were presented as relative data normalized against no peptide setup.

For inhibitor experiments, starved cells were incubated with 100 μM 5-(*N*-ethyl-*N*-isopropyl) amiloride (EIPA) or 500 nM wortmannin (Sigma) in α-MEM (−) for 30 min before peptide addition (total volume of 200 μL). Incubation with peptide and dextran

were performed in the presence of the respective inhibitor in α-MEM (−) for 30 min, followed by similar steps as described above.

Confocal laser scanning microscopy (CLSM)

HeLa cells (2×10^5 cells) were seeded on 35-mm glass-bottom dishes (IWAKI). After 24 h, cells were serum-starved with α-MEM (−) for 16 h. Dishes were washed with PBS and incubated with 5 μM SN21-FL in the presence of 1 mg/mL 70 kDa tetramethylrhodamine (TMR)-labeled dextran (Dex70-TMR) in α-MEM (−) for 1 h. The treated cells were washed with PBS, followed by nuclear staining with Hoechst 33342. The cells were observed using the Olympus FV1000 confocal system at 60× magnification.

Time-lapse imaging

HeLa cells (1.2×10^5 cells) were seeded on 35-mm glass-bottom dishes (IWAKI) overnight before transfection with *Lifeact-mCherry* plasmid (kindly provided by Prof. T. Itoh) using Lipofectamine LTX and Plus reagent (Thermo Fisher) according to the manufacturer's specifications. After 6 h, the medium was changed to fresh α-MEM (+) and was incubated overnight. The transfected cells were washed, and 150 μL of α-MEM (−) was added. The dish was mounted onto a stage top incubator (Tokai Hit) mounted on the FV3000 CLSM system and equilibrated for 5 min before visualization. Time-lapse images were captured with an interval of 30 s between each image capture. After 3 min, α-MEM (−) with or without 20 μM peptide (50 μL) was added to the dish to yield a final concentration of 5 μM. Images were subsequently taken for an additional 10 min (a total of 13 min).

EGFP-galectin 3 accumulation assay

HeLa cells (2×10^5 cells) were seeded on 35-mm glass-bottom dishes. After overnight incubation, the EGFP-Gal3 plasmid (kindly provided by Prof. T. Yoshimori) (1 μg) was transfected into the cells using Lipofectamine 3000 (Thermo Fisher) according to the manufacturer's protocol. After 6 h, the medium was changed to fresh α-MEM (+), and the cells were incubated for another 24 h. The transfected cells were washed with PBS and were incubated with 5 μM SN21, 2 μM LK15, 2 μM SN21-LK15, or 1 mM L-leucyl-L-leucine methyl (LLOMe; Sigma) for 30 min in α-MEM (–). Cells were washed three times with PBS before CLSM observation using the Olympus FV1000 system.

Electrophoretic mobility shift assay

For pDNA complexation, 1 μg EGFP-N1 plasmid was combined with the peptide at charge ratios (equation below) of 0.25, 0.5, 1, 3, 5, and 7 in HEPES-buffered saline (HBS; 21 mM HEPES, 135 mM NaCl, 5 mM KCl, 0.26 mM Na_2PO_4, pH 7.4) for 30 min at room temperature (~23 °C). Net charges of respective peptides were defined as following: LK15, +6; SN21–LK15, +9; considering that the following amino acids are positively and negatively charged (positively charged amino acids, Lys and Arg; a negatively charged amino acids, Glu) in addition to the positive charges of an amino group at the N-terminal. The complexes were loaded onto 0.8% agarose gel and ran at 100 V for 45 min. Gels were stained with ethidium bromide and visualized using the Typhoon FLA9000 biomolecular imager (GE Healthcare).

For siRNA complexation, 1 μg BLOCK-iT Alexa Fluor Red Fluorescent Control siRNA (Thermo Fisher) was combined with SN21–LK15 or LK15 at charge ratios of

0.25, 0.5, 1, 3, 5, and 7 in HBS for 30 min. After complex formation, the samples were subjected to 20% native polyacrylamide gel electrophoresis (100 V, 60 min), and visualized as described above.

$$\text{charge ratio}=\frac{(\text{nmol peptide})(\text{number of positive charge residues -number of negative charge residues})}{(\text{nmol siRNA})(\text{total number of bases})}$$

pDNA and siRNA transfection

For transfection of the EGFP-N1 plasmid, HeLa cells were seeded on 35-mm glass-bottom dishes and incubated overnight. Peptides were combined with pDNA (1 μg) at charge ratios of 5 in 200 μL OptiMEM and allowed to form complexes for 30 min at room temperature (~23 °C). For transfection using Lipofectamine 2000 (LF2000), 1 μL of LF2000 was combined with the plasmid in 200 μL OptiMEM, according to the manufacturer's specifications. Prepared cells were washed twice with PBS, and 800 μL α-MEM (−) was added, followed by the administration of the peptide-pDNA complex. After 6 h, the medium was changed to fresh α-MEM (+), and cells were further incubated for 24 h, before observation by CLSM.

Luciferase siRNA (siLuc, 21mer, 5′-GCG CUG CUG GUG CCA ACC CTT-3′, 5′-GGG UUG GCA CCA GCA GCG CTT-3′) and control siRNA were obtained from Sigma-Aldrich. HeLa-GL3 cells were seeded on 12-well plates (7×10^4 cells/well) and allowed to attach to the plate for 24 h. Peptides were combined with the duplex siRNA (final concentration of 50 nM, 1 mL) at charge ratios of 1.25, 2.5, 5, and 10 in 200 μL OptiMEM, and allowed to form complexes for 30 min at room temperature. Control siRNA was transfected using 1 μL LF2000 according to the manufacturer's protocol.

Luciferase assay of siLuc-transfected HeLa-GL3 cells

Transfected HeLa-GL3 cells were washed three times with PBS before adding 200 μL of GloLysis Buffer (Promega) and incubation at 25 °C for 5 min with constant shaking. Lysates (50 μL) were plated into white-walled 96-well plates (Nunc). Steady-Glo Luciferase Assay Reagent (Promega) (50 μL) was then added to each well, followed by 23 °C incubation for 5 min before luminescence measurement using GloMax-Multi Detection System (Promega). Simultaneously, total protein concentrations of each lysate were determined by Pierce BCA Assay (Thermo Fisher). Luciferase activity was calculated as relative luminescence unit per mg of protein (RLU/mg protein).

KRAS siRNA transfection

HeLa cells were seeded on 12-well plates (2×10^5 cells/well) and allowed to attach to the plate overnight. The cells were transfected with KRAS Silencer siRNA (Ambion) using LF2000 or SN21–LK15 at a charge ratio of 5, as stated above. After 6 h, the medium was discarded and replaced with fresh α-MEM (+) After incubation for additional 24 h, the transfected cells were trypsinized and either seeded on 96-well plates (5,000 cells/well) for cell viability assay or onto 12-well plates (1.5×10^5 cells/well) for western blotting.

For cell viability assay, cells seeded on 96-well plates were incubated. After 3 h, WST-8 reagent (Dojindo) was added to designated wells, and the cells were further incubated for 2 h before absorbance reading at 450 nm. This process was repeated after 24 h, 48 h, and 72 h.

Western Blot

Primary and secondary antibodies used in western blotting are listed in Table 3–2. Cells were washed with ice-cold PBS and lysed in RIPA buffer (50 mM Tris-HCl, 150 mM NaCl, 1 mM EDTA, 1% Triton X-100, 0.1 % SDS, 0.1% sodium deoxycholate, pH 7.6) containing 1× cOmplete Protease Inhibitor Cocktail (Roche). The cells were collected by scraping and transferred into pre-chilled 1.5 microcentrifuge tubes, followed by on ice for 15 min. The lysates were centrifuged (16,000 × g, 20 min, 4°C) and the supernatants were transferred into new pre-chilled microcentrifuge tubes. Total protein concentration was determined using Pierce BCA assay. Samples were boiled in SDS-PAGE loading buffer for 5 min, loaded (8 μg/well) onto 5–20% SuperSep Ace precast SDS-PAGE gel (FUJIFILM Wako), and electrophoresed (25 mA, 60 min, 25°C), The proteins on the gel were blotted onto Transblot Turbo Mini PVDF membrane (BioRad). The membrane was then blocked with 5% skim milk in Tris-buffered saline with 0.1% tween 20 (TBST, pH 7.6) for 1 h at 25°C, and incubated with diluted primary antibodies with constant agitation (4°C, overnight). The primary antibodies used were as follows: Anti-KRAS antibody (1:2000, Abcam); monoclonal anti-β-actin mouse IgG, clone AC-74 (1:10000, Sigma-Aldrich). The membrane was washed three times with TBST (10 min each washing), followed by secondary antibody incubation (25°C, 1 h) [HRP-conjugated anti-rabbit IgG (1:2000, Cell Signaling Technologies] or Amersham ECL Anti-Mouse IgG, Horseradish Peroxidase-Linked Species-Specific Whole Antibody (1:5000, GE Healthcare)] and another round of washing with TBST before detection using ECL Prime Western Blotting Detection reagent (Amersham) and visualization under LAS3000 CCD camera (GE Lifescience). After detection, the

membranes were stripped using Restore PLUS Western Blot Stripping Buffer and re-probed accordingly.

For western blot analysis of phosphorylated proteins, starved HeLa cells were incubated with the peptide solution for 10 min prior to lysis. The lysis buffer includes 1× PhosSTOP phosphatase inhibitor (Roche), and 5% bovine serum albumin in TBST was used as a blocking solution and antibody diluent. All other steps are similar to the above.

Cell viability assays

Cell viability and cell proliferation assays were performed using Cell Counting Kit-8 (Dojinjo). To check viability, cells were seeded on a 96-well plate (10,000 cells/well) and incubated for 48 h. After washing with PBS, the cells were treated with peptides (0.3, 0.625, 1.25, 2.5, 5, 10, 20, 40, or 80 μM) in α-MEM (–) for 60 min at 37°C, and washed twice with α-MEM (–, before adding 100 μL α-MEM (–) and 10 μL WST-8 reagent to each well. The plate was incubated for 2 h, followed by measuring the absorbance at 450 nm. IC_{50} was calculated using KaleidaGraph (ver. 4.01)

Alexa Fluor 488-labeled IgG (IgG-AF488) delivery

Human serum IgG (Oriental Yeast Co., Ltd.) was labeled with Alexa Fluor 488 5-sulfodichlorophenol (SDP) ester (Invitrogen) in 50 mM $NaHCO_3$ for 1 h. Unreacted probes were desalted using a PD-10 desalting column (GE Healthcare) with PBS (pH 7.5) as eluent. Labeled antibodies (IgG-AF488) were collected and concentrated by ultrafiltration.

HeLa cells (1.5×10^5 cells) were seeded on 35-mm glass-bottom dishes for 48 h, and washed three times with PBS, followed by incubation with 100 μg/mL IgG-AF488 in the presence of 5 μM SN21, 2 μM LK15, or 2 μM SN21–LK15 in α-MEM (−) (total volume of 200 μL) for 60 min. After incubation, the cells were washed three times with PBS, and extracellular IgG-AF488 was quenched by adding 0.02% trypan blue in PBS for 1 min. After washing three times with PBS, the cells were observed using the FV1000 CLSM system.

For inhibitor and 4°C experiments, attached cells were pretreated with 100 μM EIPA for 30 min or cooled in 4°C refrigerator for 15 min. The following incubation with peptide and IgG-AF488 were conducted in the presence of 100 μM EIPA and in 4°C refrigerator, respectively for 1 h in α-MEM (−) (total volume of 200 μL).

For time-course incubation, cells were incubated with IgG-Alexa488 and peptide (as stated above) and incubated for 5, 10, 15, 30, and 60 min.

For IgG delivery in the presence of bafilomycin A_1, cells were pretreated with bafilomycin A1 in DMSO or DMSO only (final DMSO concentration of 0.5%) for 30 min, followed by incubation with IgG and peptides as described above.

Anti-nucleopore complex IgG (anti-NPC) delivery

Control IgG-AF594 was made by labeling human serum IgG with Alexa Fluor 594-*N*-hydroxysuccinimidyl (NHS) ester the same as above. HeLa cells (1.5×10^5 cells) were seeded on 35-mm glass-bottom dishes and incubated for 48 h. The cells were washed three times with PBS, followed by incubation with 50 μg/mL control IgG-AF594 or anti-nucleopore complex (NPC) IgG-AF594 [anti-NPC IgG-AF594, BioLegends] in the presence of 2 μM SN21–LK15 in α-MEM (−) (total volume of 200

μL) for 60 min. After incubation, the cells were washed three times with PBS and observed using the FV3000 CLSM system.

Delivery of Cre recombinase

Cre recombinase was expressed and purified as previously described.[47] HeLa cells (5×10^4 cells) were seeded on 8-well coverglass chamber slides (IWAKI) and allowed to attach to the slides overnight. After transfection of the *LoxP-DsRed-LoxP-EGFP-N1* plasmid using Lipofectamine LTX with Plus reagent according to manufacturer's protocol, the cells were incubated for 24 h and, after washing, incubated with 5 μM Cre recombinase in the presence of 5 μM SN21, 2.5 μM LK15, or 3 μM SN21–LK15 in α-MEM (−) (200 μL) for 1 h. After washing with PBS, the cells were incubated for an additional 24 h in fresh α-MEM (+) and observed using the FV1000 CLSM system. Recombination (%) was calculated using the equation below. Approximately 3000 fluorescent cells were counted across three independent experiments.

$$\text{Recombination (\%)} = \left(\frac{\text{EGFP-expressing cells (green)}}{\text{Total number of fluorescent cells (green+red)}} \right) \times 100$$

Establishment of stable HeLa-TBS-Luci cells

The DNA fragment encoding the puromycin resistance gene, EF1 promoter, and insulator sequence was amplified from the GFP-Puro (#HR700PA-1, SBI system) using primers listed in Table 3–1. The amplified puromycin resistance gene, EF1 promoter, and insulator sequence fragments were assembled with the *Bam*HI-digested dHAx3 TALE binding sequence - luciferase (TBS-Luci) vector using the Gibson assembly

System.[76] To establish stable reporter cells (HeLa-TBS-Luci), HeLa cells were transfected with the above plasmid using Lipofectamine LTX according to the manufacturer's specifications. The selection was performed using 0.8 μg/mL puromycin.

Preparation of TALE-VP64 protein

To construct an *E. coli* expression vector *dHax3-VP64*-pET42b(+), a DNA fragment encoding the VP64 sequence was excised from the dHax3-VP64_pCMV using *Xma*I and *Xba*I, and was inserted into His-dHax3-pET42b(+).[76]

BL21(DE3) *E. coli* cells transformed with the dHax3-VP64-pET42b(+) plasmid were cultured in 1 L Luria-Bertani (LB) medium until the optical density (O.D. 600) reached 0.6. Protein expression was induced by adding β-D-1-thiogalactopyranoside (IPTG) to a final concentration of 1 mM, followed by incubation for 16 h at 20°C, with constant shaking (100 rpm). The cells harvested were resuspended in Buffer A (50 mM NaH_2PO_4, 300 mM NaCl, 10 mM imidazole, 2 mM sodium azide, pH 8.0), and lysed by sonication. The His-tagged protein in the lysates was purified using HisTrap FF 1 mL (GE Healthcare) using the following buffer systems: binding buffer (20 mM NaH_2PO_4, 500 mM NaCl, 5 mM imidazole, 2 mM sodium azide, pH 8.0); elution buffer (20 mM NaH_2PO_4, 500 mM NaCl, 500 mM imidazole, 2 mM sodium azide, pH 8.0). Protein fractions were further purified by anion-exchange chromatography using Resource Q column (GE Healthcare) with binding buffer (10 mM NaH_2PO_4, 2 mM sodium azide, pH 7.4) and elution buffer (10 mM NaH_2PO_4, 2 M NaCl, 2 mM sodium azide, pH 7.4). Collected fractions were again subjected to size-exclusion chromatography using Superdex 75 P.C. 3.2/30 column (GE Healthcare) with TALE-storage buffer (480 mM KCl, 1.6 mM EDTA, 2 mM DTT, 12 mM Tris-HCl, pH 7.5).[76] The purity of the

purified TALE-VP64 protein was confirmed by SDS-PAGE and stored in 20% glycerol until use.

Delivery of TALE-VP64

Before the assay, purified TALE-VP64 was buffer-exchanged to PBS by ultrafiltration using Amicon Ultra-0.5 mL (30,000 MWCO, Merck). The protein concentration was determined by checking the absorbance at 280 nm using NanoDrop (extinction coefficient $\varepsilon = 24800$). HeLa-TBS-Luci cells (1×10^4 cells) were seeded on 96-white walled assay plates (Nunc) and allowed to attach to the plates for 48 h in the absence of antibiotics and washed with PBS before adding 1 μM TALE-VP64 in the presence of 5 μM SN21, 2.5 μM LK15, 2 μM SN21–LK15, or 2 μM TAT–LK15 in α-MEM (−) (50 μL). For untreated setup, only α-MEM (−) (50 μL) was added, and for no peptide setup, only 1 μM TALE-VP64 in α-MEM (−) (50 μL) was added. The cells were incubated for 1 h before replacing the medium with 50 μL α-MEM (+) (50 μL) and further incubated for 8 h. The luciferase activity was determined by measuring the luminescence using GloMax-Multi Detection System (Promega) after the addition of an equal volume of Steady-Glo Luciferase Assay reagent (Promega) to each well.

Chapter 2 Cell Assay Experimental Procedures

CXCR4 NanoBRET-based interaction assay

All assays and preparations were courtesy of Dr. M. Sakyiamah, Prof. W. Nomura, and Prof. H. Tamamura (Tokyo Medical and Dental University). Chinese Hamster Ovary (CHO) cells stably expressing Nluc-CXCR4[81] (5×10^4 cells) were seeded on a white-walled Thermo Scientific Matrix 96-well microplate and incubated for 24 h before experiments. The medium in each well was removed and replaced with serum-free OptiMEM. Competitive binding assays in stable CHO cells were performed by incubating seeded cells with 10 nM TAMRA-Ac-TZ14011 in the presence of 0.1 M peptides or proteins. The substrate, furimazine reconstituted in the buffer (30 mM Tris-HCl, 10 mM EDTA, pH 7.6), was then added to each well (25 µL) to a final concentration of 10 µM, according to manufacturer's protocol. BRET was read immediately using a Wallac 1420 ARVO MX plate reader (fitted with 100 nm filter) at room temperature (~23 °C). The donor emission of Nluc was measured at 460 nm (80 nm bandpass), and the acceptor emission of TAMRA was measured at >610 nm (long pass). Data are presented as CXCR4 binding inhibition as stated below;

$$\text{CXCR4 binding inhibition}=\frac{\text{Donor emission}}{\text{Acceptor emission}}\times100$$

IGLMV-amide was used as a negative control peptide (Neg. Ctrl.).

Immunofluorescence detection of CXCR4 cell-surface expression

Knockdown of CXCR4 was performed by transfecting CXCR4 siRNA (siCXCR4, 5′-UGG UUG GCC UUA UCC UGC CUG GUA U-3′, 5′-AUA CCA GGC AGG AUA AGG CCA ACC A -3′) using LF2000 according to manufacturer's protocols. After 24 h, the cells were washed twice with ice-cold PBS with 3% bovine serum albumin (PBS-BSA), dislodged using Versene Solution (Gibco), transferred into pre-chilled microcentrifuge tubes, and were centrifuged (1000 × g, 4°C, 5 min). The cell pellets were washed twice with PBS-10% fetal bovine serum (FBS), and resuspended in 25 µL PBS-BSA, followed by the addition of 10 µL anti-CXCR4 IgG_{2A}, phycoerythrin (PE) conjugate (R&D Systems) or 5 µL mouse IgG_{2A} isotype control, PE conjugate (eBioscience). After incubation at 25°C for 30 min, the cells were washed twice with PBS-10% FBS, followed by an FCM analysis of 10,000 gated events.

Dextran uptake in the presence of AMD3100 and in CXCR4-knockdown HeLa cells

Starved cells were washed with PBS and pre-incubated with 5 µM AMD3100 (Sigma) for 30 min. Peptide treatment was performed in the presence of AMD3100. All succeeding steps are similar to the above.

For CXCR4 knockdown, HeLa cells were transfected with 50 nM CXCR4 siRNA or control siRNA (Sigma) using LF2000 (Invitrogen) according to the manufacturer's protocol. After 6 h of incubation, the culture medium was changed to fresh α-MEM (+) and further incubated for 24 hours. The cells were then starved for 16 h before peptide treatment, as described above.

Rac1 pulldown assay

HeLa cells (6×10^5 cells) were seeded on 100-mm culture dishes (IWAKI) and incubated for 48 h. After washing with PBS, the cells were starved with α-MEM (−) for 24 h, washed with pre-warmed PBS, and incubated in 2 mL of peptide solution in α–MEM (−) for 5 min. The plates were immediately cooled on ice and washed with ice-cold PBS. Pre-chilled pulldown lysis buffer [50 mM Tris-HCl, 10 mM $MgCl_2$, 300 mM NaCl, 2% octylphenoxy poly(ethyleneoxy)ethanol (IGEPAL), pH 7.5; 350 μL] with 1× Protease Inhibitor Cocktail (Cytoskeleton, Inc.) was added to each plate, and the cells were collected using a rubber scraper. Lysates were transferred to pre-chilled 1.5 mL microcentrifuge tubes and incubated on ice for 1 min, followed by centrifugation (10,000 × g, 1 min, 4°C). An aliquot (30 μL) was taken from the clarified supernatants, while the remaining were snap-frozen in liquid nitrogen and stored at −80°C until use. The total protein concentration for each sample was determined using Precision Red Advanced Protein Assay Reagent (Cytoskeleton) according to the manufacturer's protocols.

The snap-frozen lysates were quickly defrosted at 37°C and diluted to 0.8 mg/mL using the lysis buffer (a final volume of 1 mL). The lysates (800 μg protein) were added to commercially acquired PAK1–p21-binding domain (PBD)–glutathione *S*-transferase (GST) protein-bound onto glutathione beads (Cytoskeleton) according to manufacturer's protocols, and incubated on a rotator at 4 °C for 1 h. The beads were collected by centrifugation (5,000 × g, 1 min, 4 °C), washed once with a buffer containing 25 mM Tris-HCl, 30 mM $MgCl_2$, 40 mM $NaCl_2$, pH 7.5 (500 μL), and centrifuged (5,000 × g, 3 min, 4°C). All the remaining buffer was discarded, and 2 × SDS loading buffer (15 μL) was added to the beads before boiling for 5 min. SDS-

PAGE and western blotting were performed using an anti-Rac1 antibody, as described above.

Establishing HeLa cells stably expressing Lifeact-mCherry

HeLa cells stably expressing Lifeact-mCherry (lm-HeLa) were established as follows. HeLa cells are transfected with the Lifeact-mCherry plasmid (kindly provided by Prof. T. Itoh) with Lipofectamine 3000 according to manufacturer's protocol. After 24 h, the media was changed to fresh α-MEM (+). The cells were incubated for an additional 72 h before selection in the presence of 600 μg/mL G418 (FUJIFILM Wako) for 1 week. Colonies expressing Lifeact-mCherry were picked and expanded. Reorganization of the actin cytoskeleton was observed as described above.

HPLC analyses of thiol-disulfide exchange reactions

Peptides dissolved in deionized H_2O were added in a specified medium or buffer to a final concentration of 20 μM (150 μL). An aliquot of 50 μL was immediately analyzed by HPLC [column: Cosmosil 5C18-AR-II (4.6 × 150 mm) (Nacalai Tesque); gradient: 5−55% B in A (A = H_2O containing 0.1% TFA, B = CH_3CN containing 0.1% TFA) over 25 min; flow rate: 1 mL/min; detection: 220 nm] (0 min data). The remaining solution (100 μL) was incubated at 37 °C for 30 min. An aliquot of 50 μL from the incubated sample was analyzed by HPLC (30 min data). Unique peaks were collected and identified by MALDI-TOF MS.

For incubation in the presence of cells, HeLa cells were seeded on 24-well plates and allowed to attach to the plates overnight. The attached cells were serum-starved for 24 h before use. Peptides dissolved in deionized H_2O were added to the medium or

buffer (final concentration of 20 μM, 250 μL). An aliquot of 50 μL was analyzed as described above (0 min data). The starved cells were washed twice with PBS, and, after addition of the remaining peptide solution (200 μL), incubated for 30 min. The medium was then collected, and, after brief centrifugation, 50 μL of the supernatant was analyzed by HPLC (30 min data).

Ultra-high performance liquid chromatography analysis

The separation was conducted on a Shim-pack GIST C18-AQ column (3um,150 mm × 2.1 mm id, Shimadzu GLC) using a Nexera UHPLC system (Shimadzu). The mobile phase consisted of 0.1% formic acid in water (A) and 0.1% formic acid in acetonitrile (B). The gradient program was as follows: 0–3 min, 0% B; 3–15 min, linear gradient to 60% B; 15–17.5 min, 95% B; 17.5–20.0 min, linear gradient to 0% B; hold for 4 min; flow rate, 0.2 ml/min. The column oven temperature was maintained at 40˚C.

References

1. Stewart, M. P. *et al.* In vitro and ex vivo strategies for intracellular delivery. *Nature* **538**, 183–192 (2016).

2. Guillard, S., Minter, R. R. & Jackson, R. H. Engineering therapeutic proteins for cell entry: the natural approach. *Trends Biotechnol.* **33**, 163–171 (2015).

3. Craik, D. J., Fairlie, D. P., Liras, S. & Price, D. The Future of Peptide-based Drugs. *Chem. Biol. Drug Des.* **81**, 136–147 (2013).

4. Stewart, M. P., Langer, R. & Jensen, K. F. Intracellular Delivery by Membrane Disruption: Mechanisms, Strategies, and Concepts. *Chem. Rev.* **118**, 7409–7531 (2018).

5. Mix, K. A., Lomax, J. E. & Raines, R. T. Cytosolic delivery of proteins by bioreversible esterification. *J. Am. Chem. Soc.* **139**, 14396–14398 (2017).

6. Futaki, S. & Nakase, I. Cell-surface interactions on arginine-rich cell-penetrating peptides allow for multiplex modes of internalization. *Acc. Chem. Res.* **50**, 2449–2456 (2017).

7. Nischan, N. *et al.* Covalent attachment of cyclic TAT Peptides to GFP results in protein delivery into live cells with immediate bioavailability. *Angew. Chem. Int. Ed.* **54**, 1950–1953 (2015).

8. Herce, H. D. *et al.* Cell-permeable nanobodies for targeted immunolabelling and antigen manipulation in living cells. *Nat. Chem.* **9**, 762–771 (2017).

9. Tünnemann, G. *et al.* Cargo-dependent mode of uptake and bioavailability of TAT-containing proteins and peptides in living cells. *FASEB J.* **20**, 1775–1784 (2006).

10. Reissmann, S. Cell penetration: scope and limitations by the application of cell-penetrating peptides. *J. Pept. Sci.* **20**, 760–784 (2014).

11. Fu, A., Tang, R., Hardie, J., Farkas, M. E. & Rotello, V. M. Promises and pitfalls of intracellular delivery of proteins. *Bioconjugate Chemistry* vol. 25 1602–1608 (2014).

12. Kawaguchi, Y. *et al.* Syndecan-4 is a receptor for clathrin-mediated endocytosis of arginine-rich cell-penetrating peptides. *Bioconjug. Chem.* **27**, 1119–1130 (2016).

13. Takayama, K. *et al.* Effect of the attachment of a penetration accelerating sequence and the influence of hydrophobicity on octaarginine-mediated intracellular delivery. *Mol. Pharm.* **9**, 1222–1230 (2012).

14. Duncan, R. & Richardson, S. C. W. Endocytosis and intracellular trafficking as gateways for nanomedicine delivery: Opportunities and challenges. *Mol. Pharm.* **9**, 2380–2402 (2012).

15. Nakase, I. *et al.* Efficient intracellular delivery of nucleic acid pharmaceuticals using cell-penetrating peptides. *Acc. Chem. Res.* **45**, 1132–1139 (2012).

16. Jones, A. T. Macropinocytosis: searching for an endocytic identity and role in the uptake of cell penetrating peptides. *J. Cell. Mol. Med.* **11**, 670–684 (2007).

17. Conner, S. D. & Schmid, S. L. Regulated portals of entry into the cell. *Nature* **422**, 37–44 (2003).

18. Kumari, S., Mg, S. & Mayor, S. Endocytosis unplugged: Multiple ways to enter the cell. *Cell Res.* **20**, 256–275 (2010).

19. Mercer, J. & Helenius, A. Gulping rather than sipping: macropinocytosis as a way of virus entry. *Curr. Opin. Microbiol.* **15**, 490–499 (2012).

20. Mercer, J. & Helenius, A. Virus entry by macropinocytosis. *Nat. Cell Biol.* **11**, 510–520 (2009).

21. Meier, O. & Greber, U. F. Adenovirus endocytosis. *J. Gene Med.* **6**, S152–S163 (2004).

22. Wadia, J. S., Stan, R. V & Dowdy, S. F. Transducible TAT-HA fusogenic peptide enhances escape of TAT-fusion proteins after lipid raft macropinocytosis. *Nat. Med.* **10**, 310–315 (2004).

23. Nakase, I. *et al.* Cellular uptake of arginine-rich peptides: Roles for macropinocytosis and actin rearrangement. *Mol. Ther.* **10**, 1011–1022 (2004).

24. Sakagami, K., Masuda, T., Kawano, K. & Futaki, S. Importance of net hydrophobicity in the cellular uptake of all-hydrocarbon stapled peptides. *Mol. Pharm.* **15**, 1332–1340 (2018).

25. Cardarelli, F., Pozzi, D., Bifone, A., Marchini, C. & Caracciolo, G. Cholesterol-dependent macropinocytosis and endosomal escape control the transfection efficiency of lipoplexes in CHO living cells. *Mol. Pharm.* **9**, 334–340 (2012).

26. Costa Verdera, H., Gitz-Francois, J. J., Schiffelers, R. M. & Vader, P. Cellular uptake of extracellular vesicles is mediated by clathrin-independent endocytosis and macropinocytosis. *J. Control. Release* **266**, 100–108 (2017).

27. Desai, A. S., Hunter, M. R. & Kapustin, A. N. Using macropinocytosis for intracellular delivery of therapeutic nucleic acids to tumour cells. *Philos. Trans. R. Soc. B Biol. Sci.* **374**, 20180156 (2018).

28. Pei, D. & Buyanova, M. Overcoming endosomal entrapment in drug delivery. *Bioconjug. Chem.* **30**, 273–283 (2019).

29. Stewart, M. P., Langer, R. & Jensen, K. F. Intracellular delivery by membrane disruption: mechanisms, strategies, and concepts. *Chem. Rev.* **118**, 7409–7531 (2018).

30. Nakase, I., Kobayashi, S. & Futaki, S. Endosome-disruptive peptides for improving cytosolic delivery of bioactive macromolecules. *Biopolymers* **94**, 763–770 (2010).

31. Tanaka, G. *et al.* CXCR4 stimulates macropinocytosis: Implications for cellular uptake of arginine-rich cell-penetrating peptides and HIV. *Chem. Biol.* **19**, 1437–1446 (2012).

32. Crump, M. P. *et al.* Solution structure and basis for functional activity of stromal cell-derived factor-1; dissociation of CXCR4 activation from binding and inhibition of HIV-1. *EMBO J.* **16**, 6996–7007 (1997).

33. Kofuku, Y. *et al.* Structural basis of the interaction between chemokine stromal cell-derived factor-1/CXCL12 and its G-protein-coupled receptor CXCR4. *J. Biol. Chem.* **284**, 35240–35250 (2009).

34. Huang, X. *et al.* Molecular dynamics simulations on SDF-1α: Binding with CXCR4 receptor. *Biophys. J.* **84**, 171–184 (2003).

35. Loetscher, P., Gong, J. H., Dewald, B., Baggiolini, M. & Clark-Lewis, I. N-terminal peptides of stromal cell-derived factor-1 with CXC chemokine receptor 4 agonist and antagonist activities. *J. Biol. Chem.* **273**, 22279–22283 (1998).

36. Filippo, T. R. M. *et al.* CXCL12 N-terminal end is sufficient to induce chemotaxis and proliferation of neural stem/progenitor cells. *Stem Cell Res.* **11**, 913–925 (2013).

37. Li, L. *et al.* The effect of the size of fluorescent dextran on its endocytic pathway. *Cell Biol. Int.* **39**, 531–539 (2015).

38. Meier, O. *et al.* Adenovirus triggers macropinocytosis and endosomal leakage together with its clathrin-mediated uptake. *J. Cell Biol.* **158**, 1119–1131 (2002).

39. Koivusalo, M. *et al.* Amiloride inhibits macropinocytosis by lowering submembranous pH and preventing Rac1 and Cdc42 signaling. *J. Cell Biol.* **188**, 547–563 (2010).

40. Araki, N., Johnson, M. T. & Swanson, J. A. A role for phosphoinositide 3-kinase in the completion of macropinocytosis and phagocytosis by macrophages. *J. Cell Biol.* **135**, 1249–1260

(1996).

41. von Kleist, L. *et al.* Role of the Clathrin terminal domain in regulating coated pit dynamics revealed by small molecule inhibition. *Cell* **146**, 471–484 (2011).

42. Kaplan, I. M., Wadia, J. S. & Dowdy, S. F. Cationic TAT peptide transduction domain enters cells by macropinocytosis. *J. Control. Release* **102**, 247–253 (2005).

43. Futaki, S., Nakase, I., Tadokoro, A., Takeuchi, T. & Jones, A. T. Arginine-rich peptides and their internalization mechanisms. *Biochem. Soc. Trans.* **35**, 784–787 (2007).

44. Yamamoto, K. *et al.* Deregulation of the actin cytoskeleton and macropinocytosis in response to phorbol ester by the mutant protein kinase C gamma that causes spinocerebellar ataxia type 14. *Front. Physiol.* **5**, 126 (2014).

45. Davies, P. F. & Ross, R. Mediation of pinocytosis in cultured arterial smooth muscle and endothelial cells by platelet-derived growth factor. *J. Cell Biol.* **79**, 663–671 (1978).

46. Wiedman, G., Kim, S. Y., Zapata-Mercado, E., Wimley, W. C. & Hristova, K. pH-triggered, macromolecule-sized poration of lipid bilayers by synthetically evolved peptides. *J. Am. Chem. Soc.* **139**, 937–945 (2017).

47. Akishiba, M. *et al.* Cytosolic antibody delivery by lipid-sensitive endosomolytic peptide. *Nat. Chem.* **9**, 751–761 (2017).

48. Shai, Y. Mechanism of the binding, insertion and destabilization of phospholipid bilayer membranes by α-helical antimicrobial and cell non-selective membrane-lytic peptides. *Biochim. Biophys. Acta - Biomembr.* **1462**, 55–70 (1999).

49. Matsuzaki, K. *Membrane permeabilization mechanisms*. *Advances in Experimental Medicine and Biology* vol. 1117 (Springer New York LLC, 2019).

50. Van Meer, G., Voelker, D. R. & Feigenson, G. W. Membrane lipids: Where they are and how they behave. *Nat. Rev. Mol. Cell Biol.* **9**, 112–124 (2008).

51. Kobayashi, T. *et al.* Late endosomal membranes rich in lysobisphosphatidic acid regulate cholesterol transport. *Nat. Cell Biol.* **1**, 113–118 (1999).

52. Salomone, F. *et al.* A novel chimeric cell-penetrating peptide with membrane-disruptive properties for efficient endosomal escape. *J. Control. Release* **163**, 293–303 (2012).

53. Saleh, A. F. *et al.* Improved Tat-mediated plasmid DNA transfer by fusion to LK15 peptide. *J. Control. Release* **143**, 233–242 (2010).

54. Arthanari, Y., Pluen, A., Rajendran, R., Aojula, H. & Demonacos, C. Delivery of therapeutic shRNA and siRNA by Tat fusion peptide targeting bcr-abl fusion gene in Chronic Myeloid Leukemia cells. *J. Control. Release* **145**, 272–280 (2010).

55. Perry, H. A., Alhaj Saleh, A. F., Aojula, H. & Pluen, A. YOYO as a dye to track penetration of LK15 DNA complexes in spheroids: Use and limits. *J. Fluoresc.* **18**, 155–161 (2008).

56. Matsuoka, M., Wispriyono, B. & Igisu, H. Increased cytotoxicity of cadmium in fibroblasts lacking c-fos. *Biochem. Pharmacol.* **59**, 1573–1576 (2000).

57. Cornut, I., Büttner, K., Dasseux, J. L. & Dufourcq, J. The amphipathic α-helix concept. Application to the de novo design of ideally amphipathic Leu, Lys peptides with hemolytic activity higher than that of melittin. *FEBS Lett.* **349**, 29–33 (1994).

58. Castano, S., Cornut, I., Büttner, K., Dasseux, J. . & Dufourcq, J. The amphipathic helix concept: length effects on ideally amphipathic LiKj(i=2j) peptides to acquire optimal hemolytic activity. *Biochim. Biophys. Acta - Biomembr.* **1416**, 161–175 (1999).

59. Béven, L., Castano, S., Dufourcq, J., Wieslander, Å. & Wróblewski, H. The antibiotic activity of cationic linear amphipathic peptides: lessons from the action of leucine/lysine copolymers on bacteria of the class *Mollicutes*. *Eur. J. Biochem.* **270**, 2207–2217 (2003).

60. Maejima, I. *et al.* Autophagy sequesters damaged lysosomes to control lysosomal biogenesis and kidney injury. **32**, 2336–2347 (2013).

61. Paz, I. *et al.* Galectin-3, a marker for vacuole lysis by invasive pathogens. *Cell. Microbiol.* **12**, 530–544 (2010).

62. Jacobson, L. S. *et al.* Cathepsin-mediated necrosis controls the adaptive immune response by Th2 (T helper type 2)-associated adjuvants. *J. Biol. Chem.* **288**, 7481–7491 (2013).

63. Ni, R., Feng, R. & Chau, Y. Synthetic approaches for nucleic acid delivery: Choosing the right carriers. *Life* **9**, 59 (2019).

64. Nie, X. *et al.* Interactions in DNA condensation: An important factor for improving the efficacy of gene transfection. *Bioconjug. Chem.* **30**, 284–292 (2018).

65. Dufourcq, J., Neri, W. & Henry-Toulmé, N. Molecular assembling of DNA with amphipathic peptides. *FEBS Lett.* **421**, 7–11 (1998).

66. Akita, H. *et al.* Nanoparticles for ex vivo siRNA delivery to dendritic cells for cancer vaccines: Programmed endosomal escape and dissociation. *J. Control. Release* **143**, 311–317 (2010).

67. Strand, M. S. *et al.* Precision delivery of RAS-inhibiting siRNA to KRAS driven cancer via peptide-based nanoparticles. *Oncotarget* **10**, 4761–4775 (2019).

68. Kaiser, P. D., Maier, J., Traenkle, B., Emele, F. & Rothbauer, U. Recent progress in generating intracellular functional antibody fragments to target and trace cellular components in living cells. *Biochim. Biophys. Acta - Proteins Proteomics* **1844**, 1933–1942 (2014).

69. Bayer, N. *et al.* Effect of bafilomycin A1 and nocodazole on endocytic transport in HeLa cells: implications for viral uncoating and infection. *J. Virol.* **72**, 9645–9655 (1998).

70. Huotari, J. & Helenius, A. Endosome maturation. *EMBO J.* **30**, 3481–3500 (2011).

71. Méndez-Ardoy, A., Lostalé-Seijo, I. & Montenegro, J. Where in the cell is our cargo? Methods currently used to study intracellular cytosolic localisation. *ChemBioChem* **20**, 488–498 (2018).

72. Bogdanove, A. J. & Voytas, D. F. TAL Effectors: Customizable proteins for DNA targeting. *Science* **333**, 1843–1846 (2011).

73. Joung, J. K. & Sander, J. D. TALENs: a widely applicable technology for targeted genome editing. *Nat. Rev. Mol. Cell Biol.* **14**, 49–55 (2013).

74. Mahfouz, M. M. *et al.* De novo-engineered transcription activator-like effector (TALE) hybrid nuclease with novel DNA binding specificity creates double-strand breaks. *Proc. Natl. Acad. Sci. U. S. A.* **108**, 2623–2628 (2011).

75. Tsuji, S., Futaki, S. & Imanishi, M. Sequence-specific recognition of methylated DNA by an engineered transcription activator-like effector protein. *Chem. Commun.* **52**, 14238–14241 (2016).

76. Tsuji, S., Futaki, S. & Imanishi, M. Creating a TALE protein with unbiased 5′-T binding. *Biochem. Biophys. Res. Commun.* **441**, 262–265 (2013).

77. Beerli, R. R., Segal, D. J., Dreier, B. & Barbas, C. F. Toward controlling gene expression at will: specific regulation of the erbB-2/HER-2 promoter by using polydactyl zinc finger proteins constructed from modular building blocks. *Proc. Natl. Acad. Sci. U. S. A.* **95**, 14628–14633 (1998).

78. Akishiba, M. & Futaki, S. Inducible membrane permeabilization by attenuated lytic peptides: a

new concept for accessing cell interiors through ruffled membranes. *Mol. Pharm.* **16**, 2540–2548 (2019).

79. Yoshida, S., Pacitto, R., Inoki, K. & Swanson, J. Macropinocytosis, mTORC1 and cellular growth control. *Cell. Mol. Life Sci.* **75**, 1227–1239 (2018).

80. Xu, L., Li, Y., Sun, H., Li, D. & Hou, T. Structural basis of the interactions between CXCR4 and CXCL12/SDF-1 revealed by theoretical approaches. *Mol. Biosyst.* **9**, 2107 (2013).

81. Sakyiamah, M. M., Nomura, W., Kobayakawa, T. & Tamamura, H. Development of a NanoBRET-based sensitive screening method for CXCR4 ligands. *Bioconjug. Chem.* **30**, 1442–1450 (2019).

82. England, C. G., Ehlerding, E. B. & Cai, W. NanoLuc: A small luciferase is brightening up the field of bioluminescence. *Bioconjug. Chem.* **27**, 1175–1187 (2016).

83. Hanaoka, H. *et al.* Development of a 111In-labeled peptide derivative targeting a chemokine receptor, CXCR4, for imaging tumors. *Nucl. Med. Biol.* **33**, 489–494 (2006).

84. Boute, N., Jockers, R. & Issad, T. The use of resonance energy transfer in high-throughput screening: BRET versus FRET. *Trends Pharmacol. Sci.* **23**, 351–354 (2002).

85. Fujii, N. *et al.* Molecular-size reduction of a potent CXCR4-chemokine antagonist using orthogonal combination of conformation- and sequence-based libraries. *Angew. Chem. Int. Ed.* **42**, 3251–3253 (2003).

86. Veldkamp, C. T. *et al.* Structural basis of CXCR4 sulfotyrosine recognition by the chemokine SDF-1/CXCL12. *Sci. Signal.* **1**, ra4 (2008).

87. Ha, K. D., Bidlingmaier, S. M. & Liu, B. Macropinocytosis exploitation by cancers and cancer therapeutics. *Front. Physiol.* **7**, 381 (2016).

88. Pacitto, R., Gaeta, I., Swanson, J. A. & Yoshida, S. CXCL12-induced macropinocytosis modulates two distinct pathways to activate mTORC1 in macrophages. *J. Leukoc. Biol.* **101**, 683–692 (2017).

89. Poole, L. B. The basics of thiols and cysteines in redox biology and chemistry. *Free Radic. Biol. Med.* **80**, 148–157 (2015).

90. Taguchi, A. *et al.* 3-Nitro-2-pyridinesulfenates as efficient solution- and solid-phase disulfide bond forming agents. *Chem. Eur. J.* **23**, 8262–8267 (2017).

91. Futaki, S. & Kitagawa, K. Peptide-unit assembling via disulfide cross-linking: A versatile approach which enables the creation of artificial proteins comprising helices with different amino acid sequences. *Tetrahedron* **53**, 7479–7492 (1997).

92. Tamamura, H. *et al.* Disulfide bond formation in S-Acetamidomethyl cysteine-containing peptides by the combination of silver trifluoromethanesulfonate and dimethylsulfoxide / aqueous HCl. *Tetrahedron Lett.* **34**, 4931–4934 (1993).

93. Wu, C., Leroux, J.-C. & Gauthier, M. A. Twin disulfides for orthogonal disulfide pairing and the directed folding of multicyclic peptides. *Nat. Chem.* **4**, 1044–1049 (2012).

94. Wu, C., Belenda, C., Leroux, J.-C. & Gauthier, M. A. Interplay of chemical microenvironment and redox environment on thiol-disulfide exchange kinetics. *Chem. Eur. J.* **17**, 10064–10070 (2011).

95. Aubry, S. *et al.* Cell-surface thiols affect cell entry of disulfide-conjugated peptides. *FASEB J.* **23**, 2956–2967 (2009).

96. Li, T. *et al.* Biscysteine-bearing peptide probes to reveal extracellular thiol–disulfide exchange reactions promoting cellular uptake. *Anal. Chem.* **89**, 8501–8508 (2017).

97. Meng, X., Li, T., Zhao, Y. & Wu, C. CXC-mediated cellular uptake of miniproteins: Forsaking "Arginine Magic". *ACS Chem. Biol.* **13**, 3078–3086 (2018).

98. Wei, Y., Tang, T. & Pang, H.-B. Cellular internalization of bystander nanomaterial induced by TAT-nanoparticles and regulated by extracellular cysteine. *Nat. Commun.* **10**, 3646 (2019).

99. Doodnauth, S. A., Grinstein, S. & Maxson, M. E. Constitutive and stimulated macropinocytosis in macrophages: Roles in immunity and in the pathogenesis of atherosclerosis. *Phil. Trans. R. Soc. B* **374,** 20180147 (2019).